Fundamental Investigations of Single-entity Electrochemistry towards Ultrasensitive Biosensing

Ruixuan Wan

A dissertation

submitted in partial fulfillment of the

requirements for the degree of

Doctor of Philosophy

University of Washington

2025

Reading Committee:

Bo Zhang, Chair

Dan Fu

Joshua Charles Vaughan

Program Authorized to Offer Degree:

Chemistry

University of Washington

Abstract

Fundamental Investigations of Single-entity Electrochemistry towards Ultrasensitive Biosensing

Ruixuan Wan

Chair of the Supervisory Committee:

Bo Zhang

Department of Chemistry

This dissertation explores novel advances in single-entity electrochemistry, with a focus on understanding nanoscale electrochemical processes and developing innovative sensing platforms. Chapter 2 investigates the electrocatalytic behavior of individual Pt nanoparticles on electrode-solution interface using a single-nanoparticle collision approach. The study reveals that molecular adsorption and dynamic changes in the local chemical environment critically influence catalytic responses. Furthermore, the observed steady-state currents are found to be governed by either chemical kinetics or mass transport limitations, providing key mechanistic insights into single-nanoparticle electrochemistry. In Chapter 3, a glass microbulb (GMB) nanopore is employed to study the transient bipolar electrochemical behavior of single metal nanoparticles. The design of GMB enables high-throughput recording of translocation events with minimal clogging. The ionic current response exhibits biphasic signals at low voltages and oscillatory behavior at higher potentials, suggesting the formation of transient nanobubbles on moving nanoparticles. These findings advance the development of ultrasensitive biosensors based on single-entity bipolar electrochemistry. Chapters 4 and 5 focus on the development of optical imaging techniques for single-entity electrochemical detection. Chapter 4 explores the use of electrogenerated chemiluminescence

(ECL) to image gold nanoparticle translocations, identifying key challenges such as nanoparticle residence time, faradaic efficiency, and optical sensitivity. Chapter 5 introduces a novel dark-field microscopy (DFM) platform based on closed-bipolar electrochemistry, enabling real-time optical monitoring of electrochemical reactions. This system demonstrates quantitative detection capabilities, serving as a promising optical reporter for transient single-entity electrochemistry. Collectively, this work advances fundamental understanding and practical applications of single-entity electrochemistry, paving the way for next-generation biosensing, nanoscale electroanalysis, and high-throughput single-particle studies.

TABLE OF CONTENTS

LIST OF FIGURES

LIST OF TABLES

ACKNOWLEDGEMENTS

First and foremost, I would like to express my deepest gratitude to my research advisor, Prof. Bo Zhang, for your support and exceptional mentorship throughout my graduate studies. From my very first day in the lab in Autumn 2019 to the completion of this journey, working under your guidance has been an incredibly rewarding experience. Your infectious enthusiasm for novel ideas and your constant encouragement to explore new directions have been a tremendous source of motivation, pushing me to continually expand my knowledge and pursue new challenges. I am particularly grateful for the intellectual freedom you afforded me in the lab, coupled with your thoughtful guidance, both of which have been instrumental in my growth as a researcher.

I am also highly grateful to my committees: Prof. Joshua Vaughan, Prof. Dan Fu, and Prof. Ying Zheng for your insightful comments and support of my research. Also, thank you to my former committee Prof. Xiaohu Gao for sharing your expertise in the field of biosensing.

I extend my deepest gratitude to my colleagues in the Zhang group, past and present. I am particularly thankful to Dr. Samuel Barlow, Dr. Todd Anderson, Dr. Hongfang Gao, and Chris McAllister for your support and willingness to assist me whenever needed. It has been a privilege to work alongside such an exceptional team. To Todd Lewis, whose tireless work ethic has been a constant source of inspiration. To Wes Leininger, our optics expert, thank you for patiently guiding me through the microscopy world and for the friendship we shared, both in and out of the lab. Jupeng Zhang ("JPEG"), your kindness and generosity are unmatched, you are the master of caring for others. Wenyu Huang, though the most junior member, your technical skill and scientific insight have left an impression on me. To Dr. Zhuoyu Peng, while our time together in the lab may have been short, I deeply value all our conversations and text exchanges even after graduation. Thank you for consistently reminding me that every cloud has a silver lining and that perfection isn't always necessary, these lessons have been invaluable to me. To Dr. Milomir Suvira, I remain constantly amazed by your endless stream of innovative ideas. More importantly, I'm grateful for your guidance in helping me become a better scientist. In addition, thank you for teaching me when to say no.

To Dr. Peter Aaron Defnet, I still remember my first week in Bo's lab, back when I didn't even know what UME was. Yet, you patiently mentored me, teaching me the fundamental skills to become an electrochemist. I'll never forget the countless hours we spent troubleshooting experiments together. You show me what it means to be a true scientist: meticulous, dedicated, curious, and endlessly knowledgeable. But beyond being an incredible lab partner, you've also been a wonderful presence in my life. Your love and support carried me through the most challenging moments of my PhD. I'm endlessly grateful for every adventure we shared, and for all those drives you made between Seattle and Portland. Whatever the future holds, one thing is certain: I will always cherish the memories we've made together.

Additionally, I would like to express my deepest gratitude to my friends. Wenqiu Ma, thank you for being my emergency contact over the past six years. Words cannot capture how much your friendship and unconditional support have meant to me. You've been not just my best friend but also my family here in the U.S., and I'm certain I couldn't have made it through my PhD without you by my side. Rowena Yin, though you started as my "student," I'm incredibly grateful our bond grew into a lifelong friendship. And don't worry—you are and will always my good "daughter". Dr. Liu Cao (now Prof. Cao), Dr. Hao Yin, and Qinlin Yu thank you for your friendship since day one at UW—your companionship has been a constant throughout this journey. Minhao Jiang and Zonghui Yao, thank you for hiking every mountain and trail with me, sharing countless dinners, and keeping me company through all those late-night drinks. I'm also deeply thankful to Dongyu Wei, Mingfei Chen, Yanxiao Sun, Fiona Xi Xu, Yuting Zeng and Jiahao Wan for bringing so much joy and brightness into my life. Lastly, to Dr. Yan Lu, Qinchen Zhang, and Rong Qin, despite the vast distance of the Pacific Ocean between us, your support has always meant the world to me.

I also thank my cats, Petruchio (aka little P) and Rourou, you are the (0, 0, 0, 0) of my life. In an ever-changing world, it is a single point of consistency. If my life were expressed as a function on a four-dimensional Cartesian coordinate system, the moment I see you waiting for me home, the spot you stand would be (0, 0, 0, 0).

Lastly, I'd especially like to thank my parents, Hongyan Guo and Honghui Wan, who always love me and support me unconditionally, despite being thousands of miles away. None of those would happen without your love and support. Thank you so much for letting me stand on your shoulders so I can see a whole different world and achieve my dream.

CHAPTER 1 INTRODUCTION

1.1 Single-Nanoparticle Collision Electrochemistry

Over the past two decades, single-entity electrochemistry (SEE) has emerged as a powerful tool for resolving individual analyte units within a bulk electrochemical response. Among SEE techniques, single-nanoparticle collision electrochemistry (also termed nanoimpact electrochemistry) has become a prominent electroanalytical approach for probing nanoparticle (NP) properties and behaviors at the single-particle level. This method relies on the stochastic collisions of micro- or nanoscale entities with a voltage-biased ultramicroelectrode (UME), generating discrete current transients that reflect dynamic interactions between the NPs and the charged electrode surface. [1]

The nature of the collision-induced current signals depends on the composition, and catalytic activity of NPs, as well as the electrode properties. These signals may arise from the blocking of faradaic processes[2], direct NPs oxidation [3–5], or electrocatalytic amplification driven by the NPs [6,7]. Such measurements provide critical insights into particle size[8], aggregation state[9,10], concentration[11,12], catalytic activity[13,14], and interfacial interactions[15]. To date, this approach has been applied to diverse nanomaterials, including metals[16], dielectrics[17], organic NPs[18], and biological species[19]. Moreover, single-nanoparticle collision electrochemistry has enabled the development of sensitive biosensors for detecting microRNAs[20], cancer cells[21], and viruses[22].

In 2007, Bard and co-workers published a key detection scheme of single-nanoparticle collision electrochemistry that used electrocatalytic amplification.[6] This method uses an inner sphere redox mediator whose redox kinetics are material-specific. Examples of redox mediator reactions include hydrazine oxidation[23,24], hydrogen peroxide oxidation[25], and proton reduction[26,27]. An electrode material that is kinetically sluggish toward the redox mediator is biased to a potential where it does not drive a reaction. A more catalytically active NP collides on an electrode surface, guided by diffusion and migration. Upon the arrival of NP, when the NP first contacts the electrode surface, it adopts the potential of the electrode and produces a charging current that is too small to measure.[28] Then the redox mediator undergoes a redox process that generates a transient current signal. This method has been extensively used to study the electrocatalytic properties of individual NPs, further expanding the structure-function relationship regarding NP catalytic activity.

In this detection scheme, the electrode material, redox mediator, and NP composition are all critically important factors. For one, these parameters will contribute toward whether the generated shape of the current is a step or a spike. A step is produced from an uninterrupted redox reaction with the mediator. In Bard's theory, the current is generated due to a diffusion-limited redox reaction.[29] If one assumes that the faradaic redox process is controlled by diffusion and the surface concentration of the redox mediator at the NP surface drops to zero at the applied potential, then the magnitude of the diffusion-controlled current step can be calculated using Equation 1 for spherical particles in contact with a planar electrode.[29] Here, $I_{ss(sphere)}$ is the magnitude of the current step, n is the number of electrons transferred, F is Faraday's constant, D and C^* are the diffusion coefficient and bulk concentration of the redox mediator, and r is the radius of the colliding NP:

$$I_{ss_{(sphere)}} = 4\pi(ln2)nFDC^*r \tag{1}$$

A spike, however, can form under varying conditions. In the simplest case, a spike may be observed when the NP collides and then quickly leaves the electrode surface, thus only generating current for a short period of time. It's also possible for a 'deactivation' mechanism to occur, in which the NP loses some of its catalytic ability due to surface passivation. Deactivation has been proposed to occur due to the formation of bubbles from the reaction of the redox mediator, either encapsulating the entire particle or simply covering a portion of the NP surface area. [30, 31] A freshly nucleated nanobubble of nitrogen, formed in the oxidation of hydrazine for example, was recently determined to require approximately 8000 molecules and have a radius of about 8 nm, which would be small enough to generate on the surface of an appropriately sized NP.[32] A deactivation mechanism specific toward platinum (Pt) NPs colliding on hemispherical mercury electrodes has also been established [33–35]. Upon collision, the Pt NP either sinks into the liquid mercury or is 'poisoned' by the formation of an amalgam, thus deactivating the particle and forming a spike-shaped current. Recent advances in ultrafast chronoamperometry have revealed previously unresolved features in collision dynamics.[26,36–38] This technique clearly distinguishes rapid processes (e.g., μs-scale hydrogen monolayer formation during hydrogen-evolution reaction) from slower catalytic steps (e.g., ms-scale sustained hydrogen evolution).[36] These findings demonstrate that current transients serve as sensitive reporters of both interfacial processes and reaction mechanisms, providing rich information about NP dynamics and surface chemistry.

Previous studies have demonstrated that diffusion-limited models fail to fully account for the behavior of certain electrocatalytic amplification collision systems. For example, in a hydrazine system, experimentally measured step currents are significantly lower than the predicted value (calculated by E1) based on particle radius and bulk hydrazine concentration[23,39–42]. Notably, reported ratios between the expected and observed current vary widely, ranging from 3 to 20. While prior work has attributed these discrepancies to potential variations in hydrazine's diffusion coefficient, such an explanation would require an unrealistic ~10-fold change in diffusion coefficient, suggesting that the diffusion-limited assumption may not hold under certain conditions.

To explore alternative mechanisms beyond the diffusion-limited model, in Chapter 2, I report a mechanistic study of the electrocatalytic response of single Pt NPs on a carbon UME in a hydrazine solution. Through high-temporal single NP collision measurement, my study shows their catalytic response is characterized by a sharp, <50 μs-long current spike followed by a steady step-current signal. My results suggest that the current spike is due to the quick oxidation of hydrazine molecules pre-adsorbed onto the NP surface, while the step current reflects the continuous catalytic oxidation of protonated hydrazine, which goes through a deprotonation and adsorption step on Pt. Since each protonated hydrazine molecule releases five protons upon complete oxidation, a drastic decrease in local pH can be expected in the vicinity of the NP. This pH shift in turn limits the rate of adsorption and the steady-state oxidation current one can observe from each colliding particle. My study reveals the key importance of molecular adsorption and the changing local chemical environment (e.g., pH) to the observed catalytic response of single NPs and highlights that steady-state currents in their measurement may be chemically or mass-transport limited.

1.2 Nanopore Sensing

Nanopores represent a powerful class of sensors consisting of nanometer-scale apertures, which can be either formed by biological ion-channel proteins or engineered in solid-state materials. The fundamental concept originates from the Coulter counter principle, where particle counting was first achieved by detecting micrometer-scale pore blockages.[43] Since then, nanopore sensing has emerged as a versatile platform for SEE, enabling the detection and characterization of diverse analytes including DNA[44], RNA[45], peptides[46], proteins[47], viruses[48], small molecules[49], and nanoparticles[50].

In biological nanopore systems, ion-channel proteins (e.g., α-hemolysin, α-HL) are embedded within lipid bilayers to form well-defined nanopores.[51] These protein pores offer distinct advantages including precise, reproducible pore dimensions and modifiable inner wall chemistry through protein engineering. However, their analytical applications face three key limitations: (1) lipid bilayer instability[52], (2) challenges in controlled channel insertion[53], and (3) time-dependent current decay[54]. Solid-state nanopores address these limitations through scalable fabrication techniques, including glass pipette pulling, controlled dielectric breakdown, and advanced nanofabrication methods such as focused ion beam milling, electron-beam lithography, and atomic layer deposition.[55,56] These approaches enable precise pore-size engineering across the 10–100 nm range, combining reproducibility with tailored physicochemical properties for diverse sensing applications.

The majority of nanopore systems operate via the resistive-pulse mechanism. In a typical configuration, a pair of driving electrodes (usually Ag/AgCl) are placed on two sides of the pore. Then a constant potential is applied across the substrate containing the nanopore through the driving electrodes, while the resulting ionic current is monitored with high temporal resolution. NPs translocation events generate characteristic resistive current signals due to partial blockage of the pore, which leads to ion depletion and thus causes resistive peaks.[57,58] However, several studies have also reported the occurrence of conductive or biphasic peaks (conductive peak followed by resistive peak) during the translocation of conductive NPs. The phenomenon of the current enhancement can be influenced by electrolyte concentration, NP-to-pore size ratio, and the NP surface charge.[59] The prevailing explanation in the literature attributes conductive events to the counterion cloud surrounding NPs, which enhances local ion accumulation inside the nanopore under low-salt conditions.[60–63] Additionally, in polymer-electrolyte nanopores, resistive peaks emerge when the NP size closely matches the pore dimensions.[64,65] The signal transitions from biphasic (resistive-conductive) to purely conductive as the NP size decreases relative to the pore (or vice versa). This behavior is attributed to the deformation of the nanopore's liquid-liquid interface (between the inner aqueous salt solution and outer polymer electrolyte) by the translocating NP. The resulting ionic rearrangement enhances current, which shows conductive or biphasic peaks. The rich information encoded in translocation events, including signal shape, amplitude, and duration, enables quantitative characterization of analyte size[66], dynamic conformation[67], electrophoretic mobility[68], and surface charge[69]. Moreover, translocation frequency provides a direct measure of analyte concentration, facilitating both quantitative analysis and single-molecule detection.[70]

Beyond traditional translocation-based sensing, which relies solely on non-faradaic ionic current, recent advancements in nanopore-based wireless sensing have gained significant attention due to their ability to provide additional faradaic information at the nanoscale. In a nanopore-supported nanoelectrode system, a nanoscale conductive metal is deposited at the nanopore orifice, enabling it to function as a bipolar electrode for wireless sensing.[71] This configuration allows two half-redox reactions to be wirelessly coupled as potential is applied across two driving electrodes without direct contact with the deposited metal. Nanopore-supported nanoelectrodes have been successfully employed to image the dynamic collision process of single Ag NPs at the electrode/solution interface.[72] Additionally, it has facilitated single fluorescent molecule detection, demonstrating its utility in nanoconfined electrochemical sensing with single-molecule sensitivity.[73] As an alternative to deposited nanoelectrodes, our group recently developed a method to probe the transient electrochemical behavior of single Ag NPs wirelessly using a nanopore.[74] In this approach, rather than employing a fixed nanoscale metal deposit, we observed that when Ag NPs translocate through a glass pipette nanopore under an asymmetric nano-electrochemical environment, they behave as transient bipolar electrodes. This behavior couples two faradaic reactions (proton reduction and silver oxidation) resulting in significant current blockages. These findings indicate that transient bipolar electrochemistry can occur on metal NPs smaller than 50 nm when they translocate nanopores with highly localized electric fields. The ability to directly observe the electrochemical response of a single NP without requiring direct electrical connections is both scientifically intriguing and significant. This approach not only simplifies experimental setups for NP detection but also allows the application of higher driving voltages to induce redox reactions that might be unattainable under conventional UME conditions. For instance, chemically or biologically modified Au or Pt NPs may lose their electrocatalytic activity during UME-based detection with catalytic amplification.[41] However, by leveraging nanopore-based bipolar electrochemistry with an elevated bias voltage, it may be possible to overcome activation barriers and probe their redox behavior. A key limitation of this method, however, is NP clogging, which may arise due to the restricted internal volume of glass nanopipettes, and the high acid concentrations used within the pipette.

To overcome the aggregation issues, in Chapter 3, I report the development of a glass microbulb (GMB) nanopore and its use in studying the detailed bipolar electrochemical behavior of metal NPs. A GMB nanopore has a short pore length and a large internal volume making it feasible for recording hundreds or even thousands of particle translocation events without noticeable pore clogging. The bipolar electrochemistry response of a translocating Ag NP is obtained by holding a constant DC voltage across the nanopore and recording the nanopore's ionic current. The amperometric response is characterized by a simple biphasic current signal at lower applied voltages. At relatively higher voltages, an interesting oscillating current response can be seen that lasts more than 50 ms. This current fluctuation suggests nanobubbles can repeatedly form and dissolve on a moving NP as it translocates through a short glass nanopore. Detailed characterization and mechanistic understanding of the translocation behavior of single metal NPs and their bipolar electrochemistry response will benefit future research in designing ultrasensitive biosensors using the principles of single-entity bipolar electrochemistry.

1.3 Electrochemical Imaging

In the previous part, we focused on characterizing the electrochemical properties of single NPs using a current signal. However, “seeing is the truth,” electrochemical imaging combines high spatial resolution with real-time electrochemical sensing, enabling the detection, characterization, and visualization of individual entities at the nanoscale.

Current methodologies primarily employ two approaches: scanning probe techniques and combined electrochemical and optical (electro-optical) techniques. Scanning probe methods, including scanning electrochemical microscopy (SECM), scanning ion conductance microscopy (SICM), and scanning electrochemical cell microscopy (SECCM), utilize nanoscale probes (e.g., ultramicroelectrodes or nanopipettes) to raster-scan surfaces while monitoring faradaic or non-faradaic currents. These current measurements are then reconstructed into high-resolution (<100 nm)[75] maps of both electrochemical activity and/or surface topography.[76] Scanning probe methods have been widely used to image cells[77], electrocatalysts[78], surface corrosion[79], surface defect detection[80], and even single nanoparticles[81]. However, their sequential acquisition nature limits temporal resolution for dynamic processes. In comparison, electro-optical imaging integrates synchronized optical and current measurements, offering superior spatiotemporal resolution for real-time monitoring of redox processes.[82] Typically, in these setups, the optical measurement replaces the secondary electrical measurement and offers enhanced spatial resolution and sensitivity at a cost of decreased temporal resolution.

Electro-optical imaging has been adapted for transient signal detection in SEE. Among the light-generation mechanisms employed in optical-electrochemical imaging, fluorescence[83] and electrochemiluminescence (ECL)[84] are the most prevalent. Fluorescence imaging has been successfully applied to single-nanoparticle collision systems. For example, the collision of fluorescent insulating polymer beads was visualized with simulations and experiments establishing a correlation between the amperometric step height and the radial landing position of the bead on a UME. [85] Moreover, the dynamic collision of Ag NPs was imaged within a nano cell, where their oxidation/reduction processes produced distinct fluorescence profiles. This enabled real-time monitoring of the collision process at a Pt nanoelectrode.[72] Furthermore, nanoparticle translocation has also been imaged using electro-optical fluorescent imaging. Fluorescence imaging has also been coupled with resistive-pulse sensing to study nanoparticle translocation, including fluorescently labeled DNA,[86,87] H_2 formation on single freely diffusing 40 nm Ag NPs,[74] and single-pass translocations of 2 μm fluorescent polystyrene (PS) nanoparticles.[88] Additionally, the Brownian motion of nanoparticles exiting a nanopipette[89] and the multi-pass translocation of fluorescently labeled vesicles through a nanopore[90] have been optically tracked. While these methods provide direct transient optical information, their utility is limited by specialized laser illumination and photobleaching effects, which restrict long-term measurements and broader applicability. Furthermore, redox-induced fluorescence can lead to unbound mass transfer of the fluorophore post-generation, potentially contributing to elevated background signals.[91] ECL has also been employed to study the collision of individual nanoparticles at electrodes. One of the pioneering studies in electrocatalytic amplification replaced electrical detection with a photomultiplier tube (PMT) where Bard and co-workers observed that ECL precursor oxidation occurred exclusively at colliding Pt NPs, generating detectable photons, while the underlying ITO electrode remained inactive.[92] In a subsequent study, Bard and co-workers combined ECL detection with PMT-based optical readout in an emulsion droplet system, where droplet collisions triggered ECL precursor oxidation, followed by droplet reactions that produced measurable ECL signals.[93] This approach provided complementary optical measurements with reduced background compared to individual droplet collision events. Compared with fluorescence, the ECL process is triggered by an electrochemical reaction, which involves short-lifetime electro-generated radicals. The ECL emitting layer is thus confined to the electrode surface, which can effectively enhance the spatial resolution of the closed BPE array imaging system.[94] Nevertheless, the analyte must still be labeled or coupled with ECL luminophores.

To eliminate the need for analyte labeling, closed bipolar electrochemical imaging has emerged as a powerful analytical platform. In this configuration, a closed bipolar electrode (BPE) spatially couples a target redox process at one pole with an ECL reporting reaction at the opposite pole, enabling direct conversion of electrochemical activity into spatially resolved optical signals. [95] The closed BPE configuration employs a physical insulating barrier to isolate the cathodic and anodic compartments, allowing independent optimization of electrolyte conditions for both half-reactions. This design enables generic coupling between non-optical redox processes and light-generating reactions without requiring fluorescent or ECL labels on the target analyte. Significantly, the applied potential is delivered through driving electrodes rather than the BPE itself, facilitating the wireless operation of the electrode array. Our group has pioneered advanced implementations of this concept, including fluorescence-enabled electrochemical microscopy (FEEM) [96,97] and ECL-based closed bipolar electrochemical imaging systems. [98,99] These platforms enable real-time monitoring of dynamic redox processes across large-scale BPE arrays. The versatility of this approach has been demonstrated through diverse applications, including high-throughput electrocatalyst screening[99], detection of biomacromolecules [100] and cancer biomarkers[101], and live cell imaging[102]. Notably, the exceptional sensitivity of this platform has enabled single-entity detection, with demonstrated capability to resolve transient nanoparticle collision events at the single-particle level.[103]

Inspired by Chapter 3, where metal nanoparticles translocating through nanopores act as transient bipolar electrodes, in Chapter 4, I adapt this principle for imaging Au NP translocation. First, the feasibility of bipolar ECL on gold UMEs is tested, demonstrating coupled water/O_2 reduction and $Ru(bpy)_3^{2+}$/DBAE oxidation to generate spatially resolved optical signals. Next, I extend this approach to gold nanoclusters confined within nanopipettes, validating their function as nanoscale bipolar electrodes with localized ECL emissions. Finally, I attempt real-time ECL imaging of Au NPs translocations, revealing fundamental limitations imposed by transient residence times, faradaic efficiency, and optical sensitivity. My findings underscore the need for optimized nanopore geometries, enhanced ECL systems, and improved trapping strategies to achieve single-entity resolution. This study provides a framework for advancing ECL-based nanopore sensing, bridging nanoscale electrochemistry, and high-throughput biosensing applications.

Besides ECL, in Chapter 5, I present a label-free electrochemical imaging platform combining off-axis dark-field microscopy (DFM) with BPE to optically monitor copper deposition in real time. The system couples H_2O_2 oxidation at a Pt UME with cathodic copper deposition, enabling quantitative H_2O_2 detection.

This system is further applied to glucose sensing, achieving a 100 μM–1 mM linear range and 16.04 μM LOD via enzymatic H_2O_2 generation. The off-axis DFM configuration minimizes background interference while resolving nanoscale deposition dynamics. This work establishes a versatile approach for optically tracking electrochemical processes, with potential applications in biosensing and catalyst screening.

1.4 References

(1) Azimzadeh Sani, M.; Tschulik, K. Unveiling Colloidal Nanoparticle Properties and Interactions at a Single Entity Level. *Curr. Opin. Electrochem.* **2023**, *37*, 101195.

(2) Quinn, B. M.; Van 'T Hof, P. G.; Lemay, S. G. Time-Resolved Electrochemical Detection of Discrete Adsorption Events. *J. Am. Chem. Soc.* **2004**, *126*, 8360–8361.

(3) Defnet, P. A.; Zhang, B. Collision, Adhesion, and Oxidation of Single Ag Nanoparticles on a Polysulfide-Modified Microelectrode. *J. Am. Chem. Soc.* **2021**, *143*, 16154–16162.

(4) Sun, L.; Wang, W.; Chen, H. Y. Dynamic Nanoparticle-Substrate Contacts Regulate Multi-Peak Behavior of Single Silver Nanoparticle Collisions. *ChemElectroChem* **2018**, *5*, 2995–2999.

(5) Oja, S. M.; Robinson, D. A.; Vitti, N. J.; Edwards, M. A.; Liu, Y.; White, H. S.; Zhang, B. Observation of Multipeak Collision Behavior during the Electro-Oxidation of Single Ag Nanoparticles. *J. Am. Chem. Soc.* **2017**, *139*, 708–718.

(6) Xiao, X.; Bard, A. J. Observing Single Nanoparticle Collisions at an Ultramicroelectrode by Electrocatalytic Amplification. *J. Am. Chem. Soc.* **2007**, *129*, 9610–9612.

(7) Bard, A. J.; Zhou, H.; Kwon, S. J. Electrochemistry of Single Nanoparticles via Electrocatalytic Amplification. *Isr. J. Chem.* **2010**, *50*, 267–276.

(8) Zhou, Y. G.; Rees, N. V.; Compton, R. G. The Electrochemical Detection and Characterization of Silver Nanoparticles in Aqueous Solution. *Angew. Chem. Int. Ed.* **2011**, *50*, 4219–4221.

(9) Bai, Y. Y.; Yang, Y. J.; Xu, Y.; Yang, X. Y.; Zhang, Z. L. Current Lifetime of Single-Nanoparticle Electrochemical Collision for In Situ Monitoring Nanoparticles Agglomeration and Aggregation. *Anal. Chem.* **2023**, *95*, 4429–4434.

(10) Kirk, K. A.; Vasilescu, A.; Andreescu, D.; Senarathna, D.; Mondal, S.; Andreescu, S. Collision-Based Electrochemical Detection of Lysozyme Aggregation. *Anal. Chem.* **2021**, *93*, 2026–2037.

(11) Boika, A.; Bard, A. J. Time of First Arrival in Electrochemical Collision Experiments as a Measure of Ultralow Concentrations of Analytes in Solution. *Anal. Chem.* **2015**, *87*, 4341–4346.

(12) Stuart, E. J. E.; Zhou, Y. G.; Rees, N. V.; Compton, R. G. Determining Unknown Concentrations of Nanoparticles: The Particle-Impact Electrochemistry of Nickel and Silver. *RSC Adv.* **2012**, *2*, 6879–6884.

(13) Li, H.; Zhang, X.; Sun, Z.; Ma, W. Rapid Screening of Bimetallic Electrocatalysts Using Single Nanoparticle Collision Electrochemistry. *J. Am. Chem. Soc.* **2022**, *144*, 16480–16489.

(14) Wan, R.; Mahmoudi, M.; Edwards, M. A.; Zhang, B. Critical Role of Molecular Adsorption on Electrocatalysis at Single Nanoparticles. *Anal. Chem.* **2025**, *22*, 12.

(15) Pumford, A.; White, R. J. Controlling the Collision Type and Frequency of Single Pt Nanoparticles at Chemically Modified Gold Electrodes. *Anal. Chem.* **2024**, *96*, 4800–4808.

(16) Zhou, H.; Fan, F. R. F.; Bard, A. J. Observation of Discrete Au Nanoparticle Collisions by Electrocatalytic Amplification Using Pt Ultramicroelectrode Surface Modification. *J. Phys. Chem. Lett.***2010**, *1*, 2671–2674.

(17) Boika, A.; Thorgaard, S. N.; Bard, A. J. Monitoring the Electrophoretic Migration and Adsorption of Single Insulating Nanoparticles at Ultramicroelectrodes. *J. Phys. Chem. B.* **2013**, *117*, 4371–4380.

(18) Cheng, W.; Zhou, X. F.; Compton, R. G. Electrochemical Sizing of Organic Nanoparticles. *Angew. Chem. Int. Ed.* **2013**, *52*, 12980–12982.

(19) Kwon, S. J.; Bard, A. J. DNA Analysis by Application of Pt Nanoparticle Electrochemical Amplification with Single Label Response. *J. Am. Chem. Soc*. **2012**, *134*, 10777–10779.

(20) Castañeda, A. D.; Brenes, N. J.; Kondajji, A.; Crooks, R. M. Detection of MicroRNA by Electrocatalytic Amplification: A General Approach for Single-Particle Biosensing. *J. Am. Chem. Soc*. **2017**, *139*, 7657–7664.

(21) Dick, J. E. Electrochemical Detection of Single Cancer and Healthy Cell Collisions on a Microelectrode. *Chem. Commun.* **2016**, *52*, 10906–10909.

(22) Sepunaru, L.; Plowman, B. J.; Sokolov, S. V.; Young, N. P.; Compton, R. G. Rapid Electrochemical Detection of Single Influenza Viruses Tagged with Silver Nanoparticles. *Chem. Sci.* **2016**, *7*, 3892–3899.

(23) Kleijn, S. E. F.; Serrano-Bou, B.; Yanson, A. I.; Koper, M. T. M. Influence of Hydrazine-Induced Aggregation on the Electrochemical Detection of Platinum Nanoparticles. *Langmuir* **2013**, *29*, 2054–2064.

(24) Miao, R.; Shao, L.; Compton, R. G. Single Entity Electrochemistry and the Electron Transfer Kinetics of Hydrazine Oxidation. *Nano Res.* **2021**, *14*, 4132–4139.

(25) Chang, X.; Batchelor-McAuley, C.; Compton, R. G. Hydrogen Peroxide Reduction on Single Platinum Nanoparticles. *Chem. Sci.* **2020**, *11*, 4416–4421.

(26) Xiang, Z.; Deng, H.; Peljo, P.; Fu, Z.; Wang, S.; Mandler, D.; Sun, G.; Liang, Z. Electrochemical Dynamics of a Single Platinum Nanoparticle Collision Event for the Hydrogen Evolution Reaction. *Angew. Chem.* **2018**, *130*, 3522–3526.

(27) Bai, S.; You, Y.; Chen, X.; Liu, C.; Wang, L. Monitoring Bipolar Electrochemistry and Hydrogen Evolution Reaction of a Single Gold Microparticle under Sub-Micropipette Confinement. *Anal. Chem.* **2023**, *95*, 2054–2061.

(28) Kwon, S. J.; Zhou, H.; Fan, F. R. F.; Vorobyev, V.; Zhang, B.; Bard, A. J. Stochastic Electrochemistry with Electrocatalytic Nanoparticles at Inert Ultramicroelectrodes—Theory and Experiments. *Phys. Chem. Chem. Phys.* **2011**, *13*, 5394–5402.

(29) Xiao, Y.; Fan, F. R. F.; Zhou, J.; Bard, A. J. Current Transients in Single Nanoparticle Collision Events. *J. Am. Chem. Soc*. **2008**, *130*, 16669–16677.

(30) Dick, J. E.; Bard, A. J. Recognizing Single Collisions of PtCl62 − at Femtomolar Concentrations on Ultramicroelectrodes by Nucleating Electrocatalytic Clusters. *J. Am. Chem. Soc*. **2015**, *137*, 13752–13755.

(31) Zhou, M.; Yu, Y.; Hu, K.; Xin, H. L.; Mirkin, M. V. Collisions of Ir Oxide Nanoparticles with Carbon Nanopipettes: Experiments with One Nanoparticle. *Anal. Chem.* 2017, *89*, 2880–2885.

(32) German, S. R.; Edwards, M. A.; Chen, Q.; Liu, Y. Electrochemistry of Single Nanobubbles. Estimating the Critical Size of Bubble- Forming Nuclei for Gas-Evolving Electrode Reactions. Faraday Discuss. **2016**, *193*, 223–240.

(33) Dasari, R.; Tai, K.; Robinson, D. A.; Stevenson, K. J. Electrochemical Monitoring of Single Nanoparticle Collisions at Mercury- Modified Platinum Ultramicroelectrodes. *ACS Nano* **2014**, *8*, 4539–4546.

(34) Dasari, R.; Robinson, D. A.; Stevenson, K. J. Ultrasensitive Electroanalytical Tool for Detecting, Sizing, and Evaluating the Catalytic Activity of Platinum Nanoparticles. *J. Am. Chem. Soc*. **2013**, *135*, 570–573.

(35) Dasari, R.; Walther, B.; Robinson, D. A.; Stevenson, K. J. Influence of the Redox Indicator Reaction on Single-Nanoparticle Collisions at Mercury- and Bismuth-Modified Pt Ultramicroelectrodes. *Langmuir* **2013**, *29*, 15100–15106.

(36) Defnet, P. A.; Han, C.; Zhang, B. Temporally-Resolved Ultrafast Hydrogen Adsorption and Evolution on Single Platinum Nanoparticles. *Anal. Chem.* **2019**, *91*, 4023–4030.

(37) Lewis, T. H.; Zhang, B. Nanoparticle Adhesion and the Role of Nanobubbles in Single-Particle Collision Electrochemistry. *J. Phys. Chem. C* **2024**, *128*, 13074–13082.

(38) Roehrich, B.; Sepunaru, L. Nanoimpacts at Active and Partially Active Electrodes: Insights and Limitations. *Angew. Chem. Int. Ed.* **2020**, *59*, 19184–19192.

(39) Alligrant, T. M.; Anderson, M. J.; Dasari, R.; Stevenson, K. J.; Crooks, R. M. Single Nanoparticle Collisions at Microfluidic Microband Electrodes: The Effect of Electrode Material and Mass Transfer. *Langmuir* **2014**, *30*, 13462–13469.

(40) Castañeda, A. D.; Alligrant, T. M.; Loussaert, J. A.; Crooks, R. M. Electrocatalytic Amplification of Nanoparticle Collisions at Electrodes Modified with Polyelectrolyte Multilayer Films. *Langmuir* **2015**, *31*, 876–885.

(41) Castañeda, A. D.; Robinson, D. A.; Stevenson, K. J.; Crooks, R. M. Electrocatalytic Amplification of DNA-Modified Nanoparticle Collisions via Enzymatic Digestion. *Chem. Sci.* **2016**, *7*, 6450–6457.

(42) Zhang, Y.; Mao, J.; Ji, W.; Feng, T.; Fu, Z.; Zhang, M.; Mao, L. Collision of Aptamer/Pt Nanoparticles Enables Label-Free Amperometric Detection of Protein in Rat Brain. *Anal. Chem.* **2019**, *91*, 5654–5659.

(43) Coulter, W. H. Means for Counting Particles Suspended in a Fluid. Google Patents October 20, 1953.

(44) Ying, Y.-L.; Hu, Z.-L.; Zhang, S.; Qing, Y.; Fragasso, A.; Maglia, G.; Meller, A.; Bayley, H.; Dekker, C.; Long, Y.-T. Nanopore-Based Technologies beyond DNA Sequencing. *Nat. Nanotechnol.* **2022**, *17*, 1136–1146.

(45) Jain, M.; Abu-Shumays, R.; Olsen, H. E.; Akeson, M. Advances in Nanopore Direct RNA Sequencing. *Nat. Methods* **2022**, *19*, 1160–1164.

(46) Lucas, F. L. R.; Versloot, R. C. A.; Yakovlieva, L.; Walvoort, M. T. C.; Maglia, G. Protein Identification by Nanopore Peptide Profiling. *Nat. Commun.* **2021**, *12*, 5795.

(47) Varongchayakul, N.; Song, J.; Meller, A.; Grinstaff, M. W. Single-Molecule Protein Sensing in a Nanopore: A Tutorial. *Chem. Soc. Rev.* **2018**, *47*, 8512–8524.

(48) Lewandowski, K.; Xu, Y.; Pullan, S. T.; Lumley, S. F.; Foster, D.; Sanderson, N.; Vaughan, A.; Morgan, M.; Bright, N.; Kavanagh, J. Metagenomic Nanopore Sequencing of Influenza Virus Direct from Clinical Respiratory Samples. *J. Clin. Microbiol.* **2019**, *58*, 10–1128.

(49) Wang, R.; Zhang, Y.; Ma, Q. D. Y.; Wu, L. Recent Advances of Small Molecule Detection in Nanopore Sensing. *Talanta* **2024**, 126323.

(50) Tsutsui, M.; Takaai, T.; Yokota, K.; Kawai, T.; Washio, T. Deep Learning-Enhanced Nanopore Sensing of Single-Nanoparticle Translocation Dynamics. *Small Methods* **2021**, *5*, 2100191.

(51) Nivala, J.; Marks, D. B.; Akeson, M. Unfoldase-Mediated Protein Translocation through an α-Hemolysin Nanopore. *Nat. Biotechnol.***2013** *31*(3), 247–250.

(52) Hussein, E. A.; White, R. J. Silver Nanoneedle Probes Enable Sustained DC Current, Single-Channel Resistive Pulse Nanopore Sensing. *Anal. Chem.* **2021**, *93*, 11568–11575.

(53) Hussein, E. A.; Rice, B.; White, R. J. Recent Advances in Ion-Channel Probes for Nanopore Sensing: Insights into the Probe Architectures. *Anal. Chim. Acta.* **2022**, *1224*, 340162.

(54) Cao, C.; Long, Y. T. Biological Nanopores: Confined Spaces for Electrochemical Single-Molecule Analysis. *Acc. Chem. Res.* **2018**, *51*, 331–341.

(55) Xue, L.; Yamazaki, H.; Ren, R.; Wanunu, M.; Ivanov, A. P.; Edel, J. B. Solid-State Nanopore Sensors. *Nat. Rev. Mater.* **2020**, *5*(12), 931–951.

(56) Rahman, M.; Sampad, M. J. N.; Hawkins, A.; Schmidt, H. Recent Advances in Integrated Solid-State Nanopore Sensors. *Lab Chip* **2021**, *21*, 3030–3052.

(57) Lan, W. J.; Holden, D. A.; Zhang, B.; White, H. S. Nanoparticle Transport in Conical-Shaped Nanopores. *Anal. Chem.* **2011**, *83*, 3840–3847.

(58) Lan, W. J.; Holden, D. A.; Liu, J.; White, H. S. Pressure-Driven Nanoparticle Transport across Glass Membranes Containing a Conical-Shaped Nanopore. *J. Phys. Chem. C* **2011**, *115*, 18445–18452.

(59) Lastra, L. S.; Bandara, Y. M. N. D. Y.; Nguyen, M.; Farajpour, N.; Freedman, K. J. On the Origins of Conductive Pulse Sensing inside a Nanopore. *Nat. Commun.* **2022** *13*(1) 1–11.

(60) Goyal, G.; Freedman, K. J.; Kim, M. J. Gold Nanoparticle Translocation Dynamics and Electrical Detection of Single Particle Diffusion Using Solid-State Nanopores. *Anal. Chem.* **2013**, *85*, 8180–8187.

(61) Menestrina, J.; Yang, C.; Schiel, M.; Vlassiouk, I.; Siwy, Z. S. Charged Particles Modulate Local Ionic Concentrations and Cause Formation of Positive Peaks in Resistive-Pulse-Based Detection. *J. Phys. Chem. C* **2014**, *118*, 2391–2398.

(62) Chen, K.; Shan, L.; He, S.; Hu, G.; Meng, Y.; Tian, Y. Biphasic Resistive Pulses and Ion Concentration Modulation during Particle Translocation through Cylindrical Nanopores. *J. Phys. Chem. C* **2015**, *119*, 8329–8335.

(63) Sensale, S.; Peng, Z.; Chang, H. C. Biphasic Signals during Nanopore Translocation of DNA and Nanoparticles Due to Strong Ion Cloud Deformation. *Nanoscale* **2019**, *11*, 22772–22779.

(64) Marcuccio, F.; Soulias, D.; Chau, C. C. C.; Radford, S. E.; Hewitt, E.; Actis, P.; Edwards, M. A. Mechanistic Study of the Conductance and Enhanced Single-Molecule Detection in a Polymer-Electrolyte Nanopore. *ACS Nanosci. Au* **2023**, *3*, 172–181.

(65) Confederat, S.; Lee, S.; Vang, D.; Soulias, D.; Marcuccio, F.; Peace, T. I.; Edwards, M. A.; Strobbia, P.; Samanta, D.; Wälti, C.; et al. Next-Generation Nanopore Sensors Based on Conductive Pulse Sensing for Enhanced Detection of Nanoparticles. *Small* **2024**, *20*, 2305186.

(66) Maugi, R.; Hauer, P.; Bowen, J.; Ashman, E.; Hunsicker, E.; Platt, M. A Methodology for Characterising Nanoparticle Size and Shape Using Nanopores. *Nanoscale* **2019**, *12*, 262–270.

(67) Liu, S. C.; Ying, Y. L.; Li, W. H.; Wan, Y. J.; Long, Y. T. Snapshotting the Transient Conformations and Tracing the Multiple Pathways of Single Peptide Folding Using a Solid-State Nanopore. *Chem. Sci.* **2021**, *12*, 3282–3289.

(68) Kozak, D.; Anderson, W.; Vogel, R.; Chen, S.; Antaw, F.; Trau, M. Simultaneous Size and ζ-Potential Measurements of Individual Nanoparticles in Dispersion Using Size-Tunable Pore Sensors. *ACS Nano* **2012**, *6*, 6990–6997.

(69) Lan, W. J.; Kubeil, C.; Xiong, J. W.; Bund, A.; White, H. S. Effect of Surface Charge on the Resistive Pulse Waveshape during Particle Translocation through Glass Nanopores. *J. Phys. Chem. C* **2014**, *118*, 2726–2734.

(70) Nouri, R.; Tang, Z.; Guan, W. Calibration-Free Nanopore Digital Counting of Single Molecules. *Anal. Chem.* **2019**, *91*, 11178–11184.

(71) Hao, R.; Fan, Y.; Han, C.; Zhang, B. Bipolar Electrochemistry on a Nanopore-Supported Platinum Nanoparticle Electrode. *Anal. Chem.* **2017**, *89*, 12652–12658.

(72) Hao, R.; Fan, Y.; Zhang, B. Imaging Dynamic Collision and Oxidation of Single Silver Nanoparticles at the Electrode/Solution Interface. *J. Am. Chem. Soc*. **2017**, *139*, 12274–12282.

(73) Fan, Y.; Hao, R.; Han, C.; Zhang, B. Counting Single Redox Molecules in a Nanoscale Electrochemical Cell. *Anal. Chem.* **2018**, *90*, 13837–13841.

(74) Han, C.; Hao, R.; Fan, Y.; Edwards, M. A.; Gao, H.; Zhang, B. Observing Transient Bipolar Electrochemical Coupling on Single Nanoparticles Translocating through a Nanopore. *Langmuir* **2019**, *35*, 7180–7190.

(75) Bian, K.; Gerber, C.; Heinrich, A. J.; Müller, D. J.; Scheuring, S.; Jiang, Y. Scanning Probe Microscopy. *Nat. Rev. Methods Primers* **2021**, *1*, 36.

(76) Takahashi, Y.; Kumatani, A.; Shiku, H.; Matsue, T. Scanning Probe Microscopy for Nanoscale Electrochemical Imaging. *Anal. Chem.* **2017**, *89*, 342–357.

(77) Zhao, X.; Zhu, R.; Anikovskiy, M.; Wu, Q.; Ding, Z. Profiling H2O2 from Single COS-7 Cells by Means of Scanning Electrochemical Microscopy. *Biosens Bioelectron* **2023**, *227*, 115123.

(78) Sun, T.; Zhang, H.; Wang, X.; Liu, J.; Xiao, C.; Nanayakkara, S. U.; Blackburn, J. L.; Mirkin, M. V.; Miller, E. M. Nanoscale Mapping of Hydrogen Evolution on Metallic and Semiconducting MoS_2 Nanosheets. *Nanoscale Horiz.* **2019**, *4*, 619–624.

(79) Prabhakaran, V.; Kalsar, R.; Strange, L.; Marina, O. A.; Prabhakaran, R.; Joshi, V. V. Understanding Localized Corrosion on Metal Surfaces Using Scanning Electrochemical Cell Impedance Microscopy (SECCIM). *J. Phys. Chem. C* **2022**, *126*, 12519–12526.

(80) Tao, L.; Qiao, M.; Jin, R.; Li, Y.; Xiao, Z.; Wang, Y.; Zhang, N.; Xie, C.; He, Q.; Jiang, D.; et al. Bridging the Surface Charge and Catalytic Activity of a Defective Carbon Electrocatalyst. *Angew. Chem. Int. Ed.* **2019**, *58*, 1019–1024.

(81) Kleijn, S. E. F.; Lai, S. C. S.; Miller, T. S.; Yanson, A. I.; Koper, M. T. M.; Unwin, P. R. Landing and Catalytic Characterization of Individual Nanoparticles on Electrode Surfaces. *J. Am. Chem. Soc*. **2012**, *134*, 18558–18561.

(82) Peng, Z.; Wan, R.; Zhang, B. Single-Molecule Imaging for Probing the Electrochemical Interface. Curr. *Opin. Electrochem.* **2022**, *35*, 101047.

(83) Sambur, J. B.; Chen, P. Distinguishing Direct and Indirect Photoelectrocatalytic Oxidation Mechanisms Using Quantitative Single-Molecule Reaction Imaging and Photocurrent Measurements. *J. Phys. Chem. C* **2016**, *120*, 20668–20675.

(84) Xing, Z.; Lu, X.; Zhang, Z.; Zhao, Y.; Cao, Y.; Zhou, Y.; Zhu, J. J. Electrochemiluminescence Microscopy in Nano-Electrochemistry Research: Unraveling the Underlying Principles, Tracing the Evolutionary Developments, and Charting the Prospective Trajectories. *Adv. Funct. Mater* **2025**, 2425768.

(85) Fosdick, S. E.; Anderson, M. J.; Nettleton, E. G.; Crooks, R. M. Correlated Electrochemical and Optical Tracking of Discrete Collision Events. *J. Am. Chem. Soc*. **2013**, *135*, 5994–5997.

(86) McNally, B.; Singer, A.; Yu, Z.; Sun, Y.; Weng, Z.; Meller, A. Optical Recognition of Converted DNA Nucleotides for Single-Molecule DNA Sequencing Using Nanopore Arrays. *Nano Lett.* **2010**, *10*, 2237–2244.

(87) Ito, T.; Sun, L.; Crooks, R. M. Observation of DNA Transport through a Single Carbon Nanotube Channel Using Fluorescence Microscopy. *Chem. Commun.* **2003**, *3*, 1482–1483.

(88) Hauer, P.; Le Ru, E. C.; Willmott, G. R. Co-Ordinated Detection of Microparticles Using Tunable Resistive Pulse Sensing and Fluorescence Spectroscopy. *Biomicrofluidics* **2015**, *9*.

(89) Yu, Y.; Sundaresan, V.; Bandyopadhyay, S.; Zhang, Y.; Edwards, M. A.; McKelvey, K.; White, H. S.; Willets, K. A. Three-Dimensional Super-Resolution Imaging of Single Nanoparticles Delivered by Pipettes. *ACS Nano* **2017**, *11*, 10529–10538.

(90) Schmeltzer, A. J.; Peterson, E. M.; Harris, J. M.; Lathrop, D. K.; German, S. R.; White, H. S. Simultaneous Multipass Resistive-Pulse Sensing and Fluorescence Imaging of Liposomes. *ACS Nano* **2024**, *18*, 7241–7252.

(91) Qin, X.; Li, Z. Q.; Zhou, Y.; Pan, J. Bin; Li, J.; Wang, K.; Xu, J. J.; Xia, X. H. Fabrication of High-Density and Superuniform Gold Nanoelectrode Arrays for Electrochemical Fluorescence Imaging. *Anal. Chem.* **2020**, *92*, 13493–13499.

(92) Fan, F. F.; Bard, A. J. Observing Single Nanoparticle Collisions by Electrogenerated Chemiluminescence Amplification. *Nano Lett.* **2008**, *8*, 1746–1749.

(93) Dick, J. E.; Renault, C.; Kim, B.; Bard, A. J. Simultaneous Detection of Single Attoliter Droplet Collisions by Electrochemical and Electrogenerated Chemiluminescent Responses. *Agnew. Chem. Int. Ed.* **2014**, *126*, 12053–12056.

(94) Cui, C.; Jin, R.; Jiang, D.; Zhang, J.; Zhu, J. J. Electrogenerated Chemiluminescence in Submicrometer Wells for Very High-Density Biosensing. *Anal. Chem.* **2020**, *92*, 578–582.

(95) Yu, S.; Mehrgardi, M.; Shannon, C. A Bipolar Electrochemical Sensor with Square Wave Excitation and ECL Readout. *Electrochem. Commun.* **2018**, *88*, 24–28.

(96) Oja, S. M.; Guerrette, J. P.; David, M. R.; Zhang, B. Fluorescence-Enabled Electrochemical Microscopy with Dihydroresorufin as a Fluorogenic Indicator. *Anal. Chem.* **2014**, *86*, 6040–6048.

(97) Oja, S. M.; Zhang, B. Imaging Transient Formation of Diffusion Layers with Fluorescence-Enabled Electrochemical Microscopy. *Anal. Chem.* **2014**, *86*, 12299–12307.

(98) Anderson, T. J.; Defnet, P. A.; Zhang, B. Electrochemiluminescence (ECL)-Based Electrochemical Imaging Using a Massive Array of Bipolar Ultramicroelectrodes. *Anal. Chem.* **2020**, *92*, 6748–6755.

(99) Anderson, T. J.; Defnet, P. A.; Cheung, R. A.; Zhang, B. Electrocatalyst Screening on a Massive Array of Closed Bipolar Microelectrodes. *J. Electrochem. Soc.* **2021**, *168*, 106502.

(100) Wu, Y.; Gu, Q.; Wang, Z.; Tian, Z.; Liu, H.; Liu, S. Ultrasensitive Electrochemiluminescence Imaging Detection of Multiple MiRNAs in Single Cells with a Closed Bipolar Electrode Array Chip. *Anal. Chem.* **2024**, *96*, 12112–12119.

(101) Wu, M. S.; Liu, Z.; Shi, H. W.; Chen, H. Y.; Xu, J. J. Visual Electrochemiluminescence Detection of Cancer Biomarkers on a Closed Bipolar Electrode Array Chip. *Anal. Chem.* **2015**, *87*, 530–537.

(102) Wu, Y.; Gu, Q.; Wang, Z.; Tian, Z.; Wang, Z.; Liu, W.; Han, J.; Liu, S. Electrochemiluminescence Analysis of Multiple Glycans on Single Living Cell with a Closed Bipolar Electrode Array Chip. *Anal. Chem.* **2024**, *96*, 2165–2172.

(103) Defnet, P. A.; Zhang, B. Detection of Transient Nanoparticle Collision Events Using Electrochemiluminescence on a Closed Bipolar Microelectrode. *ChemElectroChem* **2020**, *7*, 252–259.

CHAPTER 2 THE CRITICAL ROLE OF MOLECULAR ADSORPTION ON ELECTROCATALYSIS AT SINGLE NANOPARTICLE[*]

2.1 *Introduction*

Metal nanoparticles (NPs) are attractive nanomaterials that have a wide range of applications in many research fields including electrocatalysis,[1] photoelectrochemistry,[2] and biosensors.[3,4] The constituent material, size, shape, ligands, and surface facets/defects of NPs all influence their (electro)catalytic rates and/or product distributions. To better characterize and control their electrocatalytic properties, it is essential to develop highly sensitive and highly resolving electroanalytical tools and methods that can reveal the electrocatalytic properties of single NPs. Toward this goal, numerous physical and analytical methods have been developed/applied to single particles including surface-plasmon resonance,[5] electrochemiluminescence microscopy,[6] single-molecule fluorescence microscopy,[7,8] dark-field microscopy,[9] scanning electrochemical microscopy (SECM),[10,11] and scanning electrochemical cell microscopy (SECCM).[12-15] One common drawback of these methods, however, is the limited throughput due to the use of surface-immobilized NPs.

The throughput challenge can be partially addressed by studying freely diffusing NPs and probing their electrochemical response when individual NPs collide on the surface of an ultramicroelectrode (UME)[16] or nanoelectrode.[17] A measurable change in the UME's electrochemical response is observed due to the collision and interaction of a NP with the electrode. Depending on the system under study, the collision signal can be obtained using one of the three major analytical strategies. First, an electrochemically inactive NP may block a fraction of the electroactive surface area on the UME resulting in a decrease in its faradaic response.[18] Second, an electrocatalytically active NP, such as Pt, may catalyze a redox reaction

---

[*] This chapter is adapted with permission from:
Wan, R.; Mahmoudi, M.; Edwards, M. A.; Zhang, B. Critical Role of Molecular Adsorption on Electrocatalysis at Single Nanoparticles. *Anal. Chem.* **2025**, *97* (7), 3955–3963. Copyright (2025) American Chemical Society.

when it collides with, and becomes electrically connected to, a more inert UME.[19-22] Thirdly, the NP may itself be oxidized/reduced leading to its dissolution/transformation when a proper potential is used along with the right solution condition.[23-25] Both the latter two methods will result in a (temporary) current increase due to more redox reactions occurring. Besides these three methods, one can also probe single NPs by allowing them to pass through a glass nanopore while recording their bipolar electrochemistry signal.[26]

The second strategy, which is often referred to as electrocatalytic amplification (ECA), can be particularly powerful when one wants to probe the intrinsic electrocatalytic activity of a certain type of NPs.[27] ECA has been successfully demonstrated using numerous inner-sphere reactions such as hydrogen evolution,[22, 28] oxygen reduction,[29, 30] water oxidation,[31] $NaBH_4$ oxidation,[32] and oxidation of hydrazine (N_2H_4).[19, 33, 34] Of these reactions, the oxidation of N_2H_4 has received considerable interest due to its importance in energy applications, such as fuel cells.[35] In ECA-based collision experiments using N_2H_4, a catalytic metal NP often generates a step-type current signal followed by a slow current decay due to NP deactivation with time.[36] The deactivation process can be accelerated when Hg is present on the UME surface generating a blip-type signal.[37, 38] A step-to-blip transition was also reported on a Ni UME when higher anodic potentials are used.[39] More complex current time traces have been attributed to multiple collision-detachment events in quick succession.[30]

Importantly, the magnitude of current step has been ascribed as the diffusion-limited NP response and used to analyze particle size distribution, redox concentration, and the diffusion coefficient of the redox species[40-42] according to the following equation,[19]

$$i_{\mathrm{ss}} = 4\pi ln(2)nFDC^{*}r \tag{1}$$

where n is the number of electrons transferred per redox molecule, F is the Faraday constant, D is the diffusion coefficient of the redox species (D = 1.39 × 10^{-5} cm^2s^{-1} for hydrazine),[43] C^* is the bulk concentration of the redox species, and r is the NP radius. To use Eqn. 1 with hydrazine as the redox molecule, one must assume that *the faradaic oxidation process is controlled by diffusion and the surface concentration of* N_2H_4 *at the NP surface drops to zero at the applied potential*. Yet experimentally measured step currents are significantly lower than the predicted value based on particle radius and N_2H_4

concentration (**Table 2.1**)[19,38, 44 - 48] suggesting that this assumption may be incorrect under certain conditions.

The pK_a of hydrazine is 8.1 at room temperature,[49] implying that in a neutral or acidic solution environment most of the N_2H_4 molecules are present as the protonated form ($N_2H_5^+$). Thus, their overall electrochemical oxidation can be described as the following reaction,[50]

$$N_2H_5^+ \rightarrow N_2(g) + 5H^+ + 4e^- \qquad (R1)$$

which can further be divided into the reversible deprotonation and adsorption of $N_2H_5^+$ onto Pt releasing one H^+ (reaction 2), followed by catalytic electro-oxidation of the adsorbed N_2H_4, releasing N_2, four H^+, and four electrons (reaction 3). Typically the first electron transfer step of reaction 3 is considered to be the rate determine step (RDS).[51]

$$N_2H_5^+ \rightleftarrows N_2H_{4(ads)} + H^+ \qquad (R2)$$

$$N_2H_{4(ads)} \rightarrow N_2 + 4H^+ + 4e^- \qquad (R3)$$

As H^+ appears as the product of reactions 2 and 3, for an insufficiently buffered solution these reactions could result in an increased concentration of H^+ in the vicinity of the NP/electrode surface. An increased H^+ concentration both decreases the amount of $N_2H_{4(ads)}$ by shifting the equilibrium of reaction 2 to the reactant and shifts the equilibrium potential of reaction 3, making it more difficult to proceed. Both phenomena predict a lower oxidation rate and thus a lower catalytic current. A similar analysis was used to explain the pH-dependent voltammetric features on a Pt UME toward hydrazine oxidation;[52] however, to our knowledge, it has not been used to interpret the electrocatalytic response of single metal NPs.

Herein, through NP collision experiments and experimentally informed numerical modeling, we show that the smaller-than-predicted step current for N_2H_4 oxidation on Pt NPs can be quantitatively understood by considering the hydrazine adsorption as a critical and ultimately rate-determining intermediate step. The oxidation reaction itself lowers the local pH making it more difficult for hydrazine to adsorb on the Pt surface. The step current can be enhanced toward the diffusion-limited value predicted by Eqn. 1 by either 1) increasing buffer capacity, 2) decreasing the N_2H_4 concentration, or 3) increasing solution pH, all of which reduce the shift in local pH upon electrooxidation. Our simulation results show that a significant amount of $N_2H_5^+$ is still present at the NP surface even at high applied potentials (e.g., 0.5 V vs Ag/AgCl), that is not reaching the mass transport-limited conditions required for Eqn. 1 to hold.

This work also reports an interesting observation of a sharp current spike associated with each collision event prior to the current step. With a peak duration less than 50 μs and no return to baseline, these current spikes are fundamentally different from the blip-type current signals previously reported for N_2H_4 oxidation for Pt NP collisions on Hg[37] or Ni UMEs[39] and are believed to be from the oxidation of the N_2H_4 species pre-adsorbed on the NP surface. An integration of the peak charge allows estimation of the number of pre-adsorbed N_2H_4 molecules.

2.2 Experimental Section

2.2.1 Reagents and Solutions

All chemical reagents were used as received. Methanol, 2-allylphenol (98%), ferrocene methanol (FcMeOH, 97%), and hydrazine (N_2H_4, anhydrous 98%) were purchased from Sigma Aldrich. Citrate-capped Pt NPs with diameters 32 ± 3 and 52 ± 7 nm dispersed in 2 mM sodium citrate were purchased from nanoComposix. Other chemicals were of at least analytical grade. Phosphate buffer solutions with pH below 4.0 were prepared with H_3PO_4 and KH_2PO_4, whereas solutions with pH between 5.8 and 7.4 were made using KH_2PO_4 and K_2HPO_4. All solutions were prepared with 18.2 MΩ-cm deionized water obtained from a Nanopure water purification system (Thermo Scientific).

2.2.2 Electrode Preparation

Fabrication of carbon-fiber disk microelectrodes (CFEs) followed a procedure that was previously described.[53] Briefly, a piece of 15-cm-long, 5-μm-diameter carbon fiber (Besfight G40−800) was aspirated into a piece of glass capillary (1.2 mm O.D./0.69 mm I.D., Sutter) and subsequently pulled into two separate tips on a Sutter P-97 glass puller. The thin glass/carbon fiber junction was further sealed by applying a small bead of epoxy. A tungsten wire and a bead of Ag-loaded epoxy were used to make an electric contact with the fiber from inside the glass capillary. The fiber protruding out of the pipette tip was then coated in a thin film of polyphenol using an electrochemical process and cut by an ultrasharp glass knife to expose a fresh carbon electrode surface prior to every collision measurement.

The 25-μm-diameter Pt disk UMEs were fabricated as previously reported.[54] Pt UMEs were freshly polished with fine 1200-grit sandpaper (Buehler) and rinsed with excess DI water before use. All the electrodes were characterized and screened by running cyclic voltammetry at 100 mV/s in an aqueous solution containing 1 mM FcMeOH and 100 mM KCl. To prepare Ag/AgCl quasi-reference electrodes, a piece of 0.5-mm-diameter Ag wire (99.99%, Alfa Aesar) was submerged in bleach for at least one hour and subsequently rinsed with DI water.

2.2.3 Electrochemical Measurements

All cyclic voltammograms (CVs) were recorded using a CHI-605 electrochemical workstation (CH Instruments). Amperometric current-time traces for NP collision were acquired using an Axopatch 200B current amplifier (Molecular Devices) with an internal low-pass filter of 10 kHz and digitized with a Digidata 1322 digitizer (Molecular Devices) at a sampling rate of 100 kHz. Amperometric data were further analyzed with Clampfit 10.7 (Molecular Devices). The few (<2% of total) collision peaks that were significantly higher than the rest, are indicative of particle aggregation and were excluded from the analysis herein. All electrochemical tests were conducted in a grounded, homemade Faraday cage. In all of the experiments detailed in this article, an Ag/AgCl quasi-reference electrode was utilized. All potentials are reported versus the quasi-reference electrode.

2.2.4 Finite Element Simulations

Numerical simulations of steady-state hydrazine oxidation on a 32-nm diameter Pt NP at the center of a 5-μm diameter carbon electrode were performed using COMSOL Multiphysics 6.1 with chemical reaction engineering add-on package. Using the simulations, which are described in detail in *Supporting*

Information section S11, the concentrations of $N_2H_5^+$, $H_2PO_4^-$, HPO_4^{2-}, N_2 and H^+ in solution were determined through solving the equations for diffusional transport coupled with the buffer equilibrium reaction. We used the experimentally measured average step currents to set the fluxes of N_2, $N_2H_5^+$ and H^+ on the surface of Pt NP while the fluxes on the surface of carbon-fiber electrode were set to the values measured from voltammetry of the carbon-fiber electrode. Further details of the implementation, including the solver conditions, are available in the automatically generated Comsol model report uploaded as a separate Supporting Information file.

2.3 Results and Discussion

2.3.1 Nanoparticle Collisions on a Carbon UME

The top trace in **Figure 2.1A** displays a typical 20 s amperometric trace recorded at 0.2 V vs. Ag/AgCl on a 5-μm-diameter CFE in a 10 mM phosphate buffer (pH = 7.5) solution containing 10 mM hydrazine and 32-nm-diameter Pt NPs at 4.4 pM (2.65×10^9 particles/ml). Eight discrete events are seen as well-resolved current increases due to single Pt NPs colliding and adhering on the CFE surface catalyzing the oxidation of N_2H_4. Such collision responses are only seen when both N_2H_4 and Pt NPs are present in the buffer solution along with a proper potential applied on the carbon UME as can be seen in the lower two traces which show examples where NPs and N_2H_4 are omitted.

Figure 2.1B shows a zoomed in view of the NP collision event highlighted with a red star in part A. Two characteristic features, which are visible in all amperometric collision responses, can be readily seen: an abrupt current increase followed by a fast current decay (i.e., a sharp current spike <50 μs in duration) and a slower (~1 ms) decay to a current step following the spike. Although the step-type current response has often been seen in the literature (see **Table 2.1** for summary of some previous measurements of Pt NP collisions for N_2H_4 electrooxidation),[19, 38, 44, 46, 47, 48] the ultrasharp spike-type current response has not been explicitly reported.

For each NP collision, we measure the spike current, step current, spike charge and spike width (full width half maximum; FWHM) as shown in **Figure 2.1B** (See *Appendix 2.1* for detailed information on data analysis). The spike currents are measured from the baseline before the collision. The slow (~1 ms) decay step after the spike is fitted by an exponential decay curve with an offset (*C* in Eqn. S1) equal to the value of the step current. The excess charge due to the sharp spike (fC; 10^{-15} coulombs) is calculated by integrating the area above the fitted curve (red shaded area in **Figure 2.1B**).

2.3.2 Influence of the Applied Potential

Figure 2.2A displays a series of representative amperometric collision peaks of 32-nm-diameter Pt NPs recorded at 0 to 0.5 V vs Ag/AgCl (see **Figure 2.9** for further examples) all recorded with the same solution conditions (10 mM phosphate buffer (pH 7.5), 10 mM N_2H_4, and 32-nm-diameter Pt NPs at 4.4 pM). At higher potentials, the sharp current spike becomes taller and faster, as evidenced by the higher amplitude of the spike current and the shorter duration (FWHM) (**Figure 2.2C** (blue points) and **2.2D**). The step current also increases with the increasing applied potential as can be seen in the red points in **Figure 2.2C**. As shown in **Figure 2.2B**, the spike charge increases with applied potential and reaches a plateau at ~16 fC at 0.2 V. As discussed below in more detail, we propose that the fast spike corresponds to oxidation of the N_2H_4 adsorbed prior to the collision. This is a finite resource the oxidation of which can be achieved more rapidly at higher potentials. A slight increase in the spike charge at 0.5 V may be caused by the increased noise level and the inadequate resolution in discerning the sharp spikes from the slow decay process. Notably, for all statistics determined, there is considerable variability from particle-to-particle, as indicated by the error bars (1 standard deviation) or box and whisker plots (part B). The variability is much larger than that in the particle size distribution (32 ± 3 nm) indicating differences in the electrocatalytic behavior between particles that can only be assessed at the single-particle level.

The short peak durations of the spikes (FWHM >40 μs) (**Figure 2.2D**) when the applied potential exceeds 0.2 V approaches the 33 μs instrument limit with a 10 kHz low-pass filter[55-57] used in this study, suggesting sharp spikes could be even faster than our measured value. While we were unable to find adequate information on instrument filtering settings used in earlier research on Pt NPs collision, the lower sampling rates used (e.g., 1 kHz[19], and 50 Hz[47]) would not be sufficient to resolve spike-like responses we report here. To confirm this we examined the impact of filter frequency and sampling rate on NP collision response as reported in **Figure 2.12**. Low-pass filtering frequency at 1 kHz and sampling rate at 1 kHz completely eliminates fast current spikes, replicating the step response reported in previous works.

To better compare decay kinetics among different potentials, we plotted the average exponential decay curves to the step value using 50 collision events from each potential (**Figure 2.2E**). As one can see, an increase in the applied potential causes a slower current decay except for the 0.5 V case, which shows a faster decay compared to the 0.3 and 0.4 V cases. Herein, we are interested in developing a deeper understanding of the collision responses focusing on quantitatively analyzing the shape and magnitude of the current spikes and the magnitude of the current steps.

Collisions for 52-nm diameter Pt NPs, which are reported in **Figure 2.10** also show the sharp current spikes becoming progressively faster and higher with higher potentials. A limiting value of ~50 fC is observed in the spike charge limit at around 0.2 V, after which the spike charge continues to increase at 0.5 V. Interestingly, as the voltage is increased to 0.5 V, we also observe transient oscillation on the amperometric traces (**Figure 2.11**). The high-frequency current oscillation are consistent with the transient formation and dissolution of small nanobubbles on the particles/electrode interface,[58] but further discussion will be covered in a forthcoming report.

2.3.3 Dependence on Hydrazine Concentration

Figure 2.3 shows NP collision events recorded in N_2H_4 solutions ranging from 2.5 to 20 mM (all 0.2 V and 10 mM pH 7.5 phosphate buffer). The use of N_2H_4 concentrations >20 mM is prohibited due to excessive aggregation of Pt NPs.[59] As one can see from **Figure 2.3A**, the spike current increases with hydrazine concentration reaching a limit at around 10 mM. Interestingly, the spike charge remains somewhat unchanged among different hydrazine concentrations (**Figure 2.3B),** which is consistent with the quantity of adsorbed hydrazine not changing over this concentration range. This would be expected of a strongly adsorbing species in the saturation limit of an adsorption isotherm (complete surface coverage). While it is expected that there is a lower threshold concentration below which decreases in the amount of adsorbed N_2H_4 would be observed, as detecting particle collisions at concentrations lower than 2.5 mM has proved to be more challenging than at higher concentrations, we have been unable to observe such a decrease.

A somewhat slow increasing trend is observed between the step current and hydrazine concentration (red line, **Figure 2.3C**, i_{ss} (pA)= 7.45C^*(mM), $R^2 = 0.88$) suggesting that the step current is dependent on hydrazine concentration. Yet, like the results with 10 mM N_2H_4 in **Figure 2.1**, the step current measured under all hydrazine concentrations is significantly smaller than the diffusion-limited current, which is shown by the green line (i_{ss} (pA)= 74.8C^*(mM), from equation 1). Previous research did not provide a satisfactory explanation for the smaller step current but sometimes explained it from possible variations in hydrazine's diffusion coefficient; however, this would require a change of ~10× in the diffusion coefficient, which appears highly unlikely.

2.3.4 Effect of the Solution pH

As reported in **Figure 2.4**, we conducted measurements of Pt NP collisions under three pH conditions: 3.1, 5.8, and 7.5 (all 10 mM phosphate buffer, 0.2 V vs. Ag/AgCl and 10 mM hydrazine). Both the spike current and step current increase with increasing solution pH (**Figure 2.13** and **Figure 2.4A**), yet in all cases the step current is still more than 10× lower than 750 pA predicted by Eqn. 1, indicating that the reaction is not transport limited. Moreover, the spike charge is increased as the solution changes from acidic to neutral (**Figure 2.4B**), which is likely due to an increased surface coverage of the adsorbed N_2H_4 at higher pH, which is consistent with reaction 2 in which H^+ is on the right-hand side.

2.3.5 Effect of Buffer Capacity

As the electrocatalytic oxidation of protonated hydrazine yields five equivalents of protons **(**reaction 1**)**, the interfacial pH at the electrode surface can be heavily decreased during the Pt NPs collision process, leading to a lower electrochemical response. Increasing the buffer capacity can help maintain the interfacial pH during the abovementioned process.[52] **Figure 2.5** presents statistics for Pt NPs collisions with phosphate buffer concentration from 10 to 50 mM (all pH 7.5, 0.2 V, 10 mM N_2H_4; see **Figure 2.14** for representative events). Note: phosphate buffer concentrations higher than 50 mM were not tested due to concerns of NP aggregation with high ionic strength.[60] We notice that the spike charge remains constant until the phosphate buffer reaches 40 mM and higher (**Figure 2.5A**), which is consistent with the amount of adsorbed N_2H_4 prior to the collision depending only on the solution pH and bulk N_2H_4 concentration. Larger error bars are seen at 40 and especially 50 mM phosphate buffer, which may suggest that some of the large peaks are due to particle aggregation at these conditions. **Figure 2.5B** shows an increasing trend in the step current amplitude with higher buffer concentrations, which is consistent with higher buffering capacity leading to smaller pH swings and reactions 2 and 3 both being more favorable.

2.3.6 Discussion of the Sharp Current Spike and the Small Step Current.

We have considered two possible mechanisms for the appearance of a sharp amperometric spike preceding the step current as seen in **Figure 2.1**. First, when a NP collides on a carbon UME poised at a potential that is different than the particle's resting potential, the surface of the NP will undergo double-layer charging. Second, the surface of the Pt NP may be covered by N_2H_4 molecules prior to their collision on the carbon UME due to strong Pt-N interaction.[61] These adsorbed molecules can undergo quick oxidation leading to a sharp amperometric peak. We can easily rule out double-layer charging with a simple calculation. For a 32-nm-diameter NP, the total number of charges transferred during double-layer charging can be estimated as 1.2×10^{-16} C, or 0.12 fC ($Q=C\times\Delta E$). This is only about 1% of the total integrated charge measured in our experiments. As such, it is unlikely that double-layer charging contributes significantly to the sharp current spikes.

As briefly mentioned during the discussion of **Figure 2.1** to **2.5** the results support our second hypothesis that the sharp spike is due to the fast oxidation of adsorbed N_2H_4. The 16 fC integrated charge corresponds to a total of 4.15×10^{-20} mol (25,000 molecules) of N_2H_4 pre-adsorbed on a 32-nm-diameter particle ($Q = nFN$), which corresponds to a little over one N_2H_4 for every 2 of the 42,000 Pt surface atoms (see Supporting Information, section S9 for details of the calculations).

Note, these calculations make an assumption of no surface roughness, yet our previous research suggest the NPs have a rough surface with a significant amount of internal voids, which would both increase the number of available binding sites.[22] As such, considering that N_2H_4 is a small neutral molecule, the idea of having a layer of adsorbed N_2H_4 molecules oxidizing when a NP collides on the electrode is quite reasonable. The spike charge remains the same under various hydrazine concentrations, suggesting that the particle reaches its maximum hydrazine monolayer coverage at and above 2.5 mM hydrazine concentration. There is no time-dependent change of spike charge following Pt NPs addition to N_2H_4 solution (**Figure 2.16**), suggesting that adsorption is fast relative to the other experimental steps. Note, similar spike-to-step transitions of pre-adsorbed species have also been suggested for the oxygen reduction[30] and hydrogen oxidation[40] although in each case with much slower transitions.

The step-type response has been ascribed to the continuous catalytic oxidation of N_2H_4 on the surface of the Pt NP. In line with most reported values in the literature (**Table 2.1**), the current step is seen to be significantly smaller than the diffusion-limited current, which can be estimated by **Eqn. 1**. For a 32-nm-diameter NP, the diffusion-limited steady-state current is ~750 pA in 10 mM N_2H_4 solution. Our measured step height is only ~90 pA at 0.2 V, or ~12% of the diffusion-limited current! Increasing the applied potential only results in a slight increase in the step current (**Figure 2.2**).

To better understand the oxidation process of hydrazine on Pt, we performed cyclic voltammetry on a 25 μm diameter Pt UME in 10 mM phosphate buffer solutions (pH 7.5) containing 2.5 to 20 mM hydrazine (**Figure 2.6**). To further investigate the effect of pH and buffer strength, we also collected CVs of a 25 μm Pt UME in 10 mM hydrazine and 10 mM phosphate buffer at different pH values (**Figure 2.13B**), and CVs in 10 mM to 50 mM phosphate buffer (pH 7.5) (**Figure 2.15**), respectively.

Two oxidation waves separated by a plateau are observed on the CV, a first oxidation wave with a half-wave potential at about -0.45 V and a second wave at +0.15 V. While both waves increase with N_2H_4 concentration, only the highest plateau current scales linearly with the hydrazine concentration and is in agreement with the diffusion-limited steady-state current ($i_{\mathrm{ss,disk}} = 4naFDC^*$, a: electrode radius).[62] This suggests that at sufficiently high driving potentials, the oxidation of N_2H_4 is transport-limited, meaning every molecule coming from solution to the Pt surface gets oxidized immediately. Only one oxidation wave is observed when N_2H_4 concentration is below ~2 mM in 10 mM buffer. Increasing the solution pH and the buffer concentration both result in a dramatic increase in the height of the 1st wave (**Figure 2.13 and Figure 2.15**). It appears the 2nd wave may totally disappear when the buffer concentration is higher than 100 mM in 10 mM N_2H_4.

This finding is consistent with an earlier report on linear sweep voltammograms of electrocatalytic hydrazine oxidation on a Pt UME.[52] The authors suggested that electro-oxidation of hydrazine caused a large drop in interfacial pH in a solution with a low buffer capacity. This change in interfacial pH leads to a decrease in the local concentration of hydrazine and a lower current on the first steady-state feature. Other papers have also explored the crucial role of pH in the electrocatalytic oxidation of hydrazine.[63, 64] Based on our CV results, we speculate that the smaller step current is largely caused by an interfacial pH drop when hydrazine oxidation proceeds on the surface of the Pt NPs.

With a pK_a of 8.1 at room temperature, it is important to note that the majority of N_2H_4 molecules are protonated ($N_2H_5^+$) at neutral or acidic pH. In a solution with insufficient buffer capacity, the electro-oxidation of hydrazine decreases the interfacial pH from 7 to ~ 2.5,[52] which then leads to the shifting of the adsorption equilibrium (reaction 2) and thus diminishes the current on the first steady state. In a solution with adequate buffer strength, however, the change in interfacial pH is minimal, which promotes the adsorption of N_2H_4 yielding a higher steady-state current.[52] Our measured step current increases from <100 pA in 10 mM buffer to >700 pA in 50 mM buffer, which supports our hypothesis (**Figure 2.5**).

2.3.7 Proposed Mechanism

Figure 2.7 provides a simple illustration of our proposed mechanism for the transient collision and electrocatalytic behavior of single Pt NPs on a carbon UME. Hydrazine is present mainly as the protonated form $N_2H_5^+$ in a neutral or acidic solution environment. Neutral N_2H_4 adsorbs onto Pt via both nitrogen lone pairs, while cationic $N_2H_5^+$, with only one lone pair, cannot bind stably. [65] Thus, protonated hydrazine would interact with the surface of the Pt NP forming a monolayer of adsorbed N_2H_4. When a Pt NP collides with the carbon UME, most of the adsorbed N_2H_4 undergoes a quick oxidation giving rise to the sharp current spike. The amplitude and duration of the current spike and total charge transferred would depend on the initial concentration of hydrazine, the applied potential, the buffer concentration, and the solution pH, and reflect the amount of the adsorbed N_2H_4.

As the adsorbed N_2H_4 is oxidized the equilibrium of reaction 2 changes and more $N_2H_5^+$ is adsorbed, this in turn sets up a concentration gradient driving $N_2H_5^+$ from bulk to the NP continuously replenishing the N_2H_4 on the Pt surface. Therefore, the oxidation of N_2H_4 can be sustained resulting in a continuous steady-state oxidation current following the collision event as measured by the step current. However, as the adsorption of each $N_2H_5^+$ and oxidation of N_2H_4 releases 1 and 4 protons, respectively, when many N_2H_4 molecules are oxidized on the NP surface, the released H^+ may cause a dramatic decrease in the local pH near the NP. This low pH environment will in turn shift the equilbrium of reaction 2 away from the product (adsorbed N_2H_4) thereby decreasing the amount of adsorbed N_2H_4, resulting in a smaller steady-state current. An increase in the buffer capacity can better maintain the interfacial pH, which leads to a higher surface coverage of $N_2H_{4(ads)}$ and a higher step current.

2.3.8 Numerical Simulation

A key goal of the simulation work is to compute the spatial distribution of some of the key chemical species near the surface of a Pt NP when it collides and adheres onto the carbon UME. Such information can be especially helpful for our understanding of the smaller catalytic current observed in the amperometric recordings. The simulations, which are described in detail in appendix (**Figure 2.17-2.20**), make no assumptions on the reaction kinetics or mechanism. Instead the average step current measured during a NP collision (at a given potential) is used to provide the steady-state fluxes of $N_2H_5^+$, N_2 and H^+ on the NP surface at that same potential using the stoichiometry from eq. 1. Similarly, the fluxes on the CFE surface are informed from measurements of voltammetric measurements of its rate (**Figure 2.18**). Using experimental data to enforce the fluxes for the overall reaction allows the model to capture all nuances of the potential-reaction rate relationship without an explicit description of the steps in the reaction mechanism or corresponding rates, it also obviates the need for explicit description of surface species that are part of those intermediate steps.

Figure 2.8 shows the solution and average surface concentrations of H^+, $N_2H_5^+$, and $H_2PO_4^-$ at various applied potentials. In the pH range considered, the buffer is a mixture of $H_2PO_4^-$ and HPO_4^{2-} with a total concentration of 10 mM, thus the concentration of HPO_4^{2-}, which is not plotted may be determined as 10 mM-[$H_2PO_4^-$]. Herein, we did not consider N_2H_4 in solution as a major species in our simulation because we know the majority of N_2H_4 is present in the protonated form at neutral or acidic pH.

Figure 2.8A & **B** show the concentration of $N_2H_5^+$ in solution. Even at the highest driving potential considered (0.5 V vs Ag/AgCl) the carbon electrode has relatively little impact on its concentration only decreasing the bulk 10 mM $N_2H_5^+$ concentration to ~9 mM at the carbon surface. In contrast, the Pt NP which is at the center of the electrode and can be seen most easily in the zoomed in view of **Figure 2.8B** influences the concentration of $N_2H_5^+$ more significantly, but only over a short distance less than 10× its radius, and nowhere is the concentration of $N_2H_5^+$ depleted to 0.

Figure 2.8C shows average surface concentrations of three key species H^+, $N_2H_5^+$, and $H_2PO_4^-$ as a function of applied potential. In general, the surface concentration of $N_2H_5^+$ drops as we increase the applied potential from 0 to 0.5 V. While the solid lines represent simulated data from measured currents, the dashed lines are obtained using current values extrapolated from the overall trend. Interestingly, even at 0.5 V. the concentration of $N_2H_5^+$ at the interfacial region is ~6 mM, which is only 40% lower than that of the bulk. This suggests the oxidation of $N_2H_5^+$ on a colliding NP is never limited by diffusion. Instead, it is likely that the overall oxidation kinetics is limited by the slower adsorption process ($N_2H_5^+ \leftrightarrow N_2H_{4\,(ads)} + H^+$), a chemical step in the overall reaction.

A second interesting finding is on the surface concentrations of $H_2PO_4^-$ and H^+. As one can see, the local proton concentration is well maintained until ~0.1 V. After passing 0.1 V, proton concentration starts to increase more rapidly at higher potentials. Meanwhile, the concentration of $H_2PO_4^-$ increases close to 10 mM, indicating that all the buffer is in this form and almost no HPO_4^{2-} remains. This loss of buffering capacity is matched by the surface H^+ concentration increasing, which as described above affects the adsorption process making it more difficult to adsorb onto the Pt.

2.4 Conclusions

In conclusion, we have demonstrated, through the use of a NP-collision approach and fast amperometric recording at high bandwidth (10 kHz), that the electrocatalytic response of a single Pt NP consists of a sharp, ultrafast oxidation spike and a long-lasting current step. The spike response is likely generated from the quick oxidation of $N_2H_{4(ads)}$ which was adsorbed on the surface of the NP prior to collision, whereas the step response comes from the continuous oxidation of $N_2H_5^+$, which must go through chemical steps of deprotonation and adsorption.

While the step-type catalytic current response has often been reported, the underlying mechanism as to why it is *significantly* smaller than the diffusion-limited current has not been fully discussed before. We used a numerical model with potential dependent rates taken directly from experimentally measured currents and no assumptions about the steps in the reaction mechanism or their rate to visualize the surface concentrations. The model allowed us to conclude that the smaller step current originates from a large pH shift when hydrazine is oxidized on the surface of the NP and the carbon UME. In a poorly buffered solution, the proton concentration near the NP surface increases causing a shift in hydrazine's adsorption equilibrium toward the freely diffusing $N_2H_5^+$. This shift of a chemical step of the overall reaction leads to an oxidation signal below the transport-limited value.

Many of the ECA-based studies involve the use of inner-sphere redox molecules, which adsorb on the surface of the NP. Our study further emphasizes the importance of understanding the molecular mechanisms toward a better understanding of the electrocatalytic signals in these experiments. Although it is appealing to assume a step current that does not change with potential is indicative of reaching a diffusion-limited regime, it is important to acknowledge that other (slower) processes may invalidate this assumption.

2.5 Figures and Table

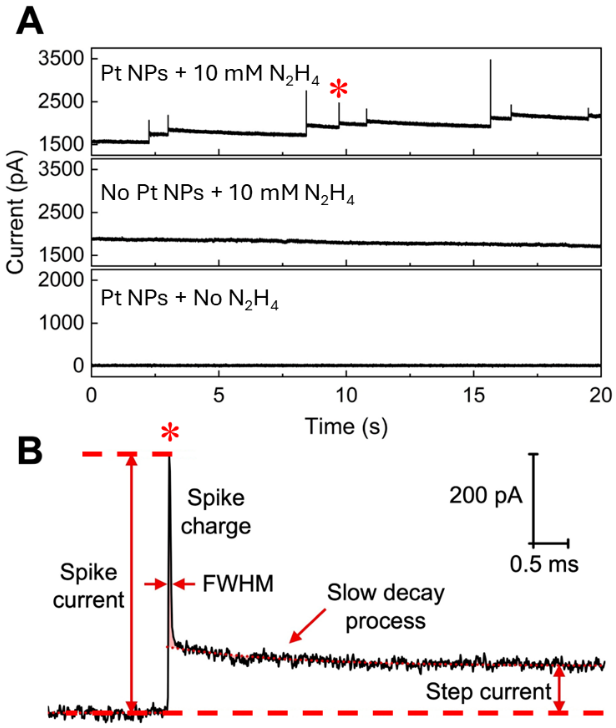

Figure 2.1. Example of current-time traces and zoom-in view of the collision event.
(A) 20-s current-time traces showing 8 individual collision events of single 32-nm-diameter Pt NPs on a 5-µm-diameter CFE biased at 0.2 V vs Ag/AgCl in a 10 mM phosphate buffer (pH=7.5) solution containing 10 mM hydrazine. (B) A zoom-in view of the collision event indicated by ∗ in part A. Characteristic measurements of the initial sharp current spike and current step are indicated. Red shaded area indicates the charge attributed to the current spike which is measured vs the slow exponentially decaying baseline (red dotted line).

Table 2.1. Summary of Some Previous Work Observing Step-type Current Response Collisions of Individual Pt NPs in Aqueous Phosphate Buffered Hydrazine Solutions.

Electrode material	Pt NP diameter (nm)	N_2H_4 conc. (mM)	Phosphate buffer conc. (mM)	Experimental step current (pA)	Predicted current (pA) (Eqn. 1)	Ref.
Au	3.3 ± 1.0	10	10	20 - 50	77.1 ± 23.4	44
Au	3.6	15	50	40 - 65	126.2	19
Au	5.5 ± 2.0	15	50	25 - 1100	192.8 ± 70.1	38
Au	22.0 ± 4.0	10	50	51 ± 41	514.0 ± 93.5	46
C	23.0 ± 5.4	50	10	100 ± 60	2686.8 ± 630.8	48
C	24.7 ± 4.0	10	10	130 ± 50	577.3 ± 93.5	47

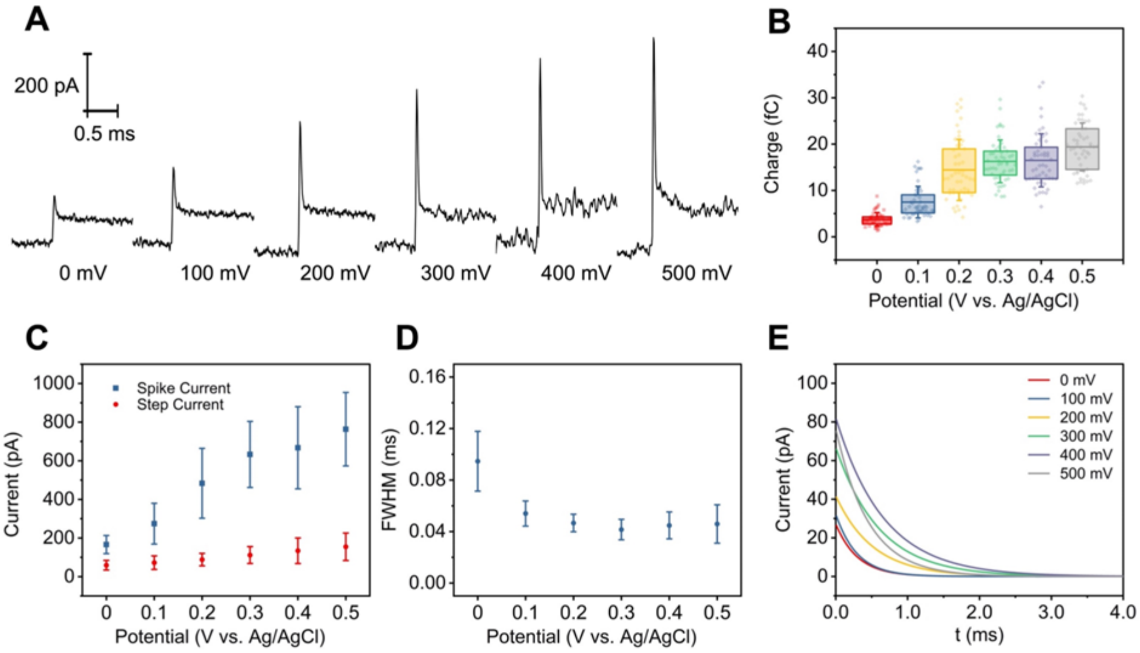

Figure 2.2. Potential dependent NP collision.
(A) Representative amperometric collision events for 32-nm-diameter Pt NPs on a CFE collected in 10 mM N_2H_4 and 10 mM phosphate buffer (pH 7.5) at different potentials. Changes in: (B) the integrated spike charge, (C) the spike and step currents, and (D) the FWHM of the spike, as a function of the applied potential. (E) Average fitted curves for slow step decay signals. The "*n*" values for (B) to (E) are all equal to 50. Datapoints on (B), (C), and (D) are presented as mean ± SD.

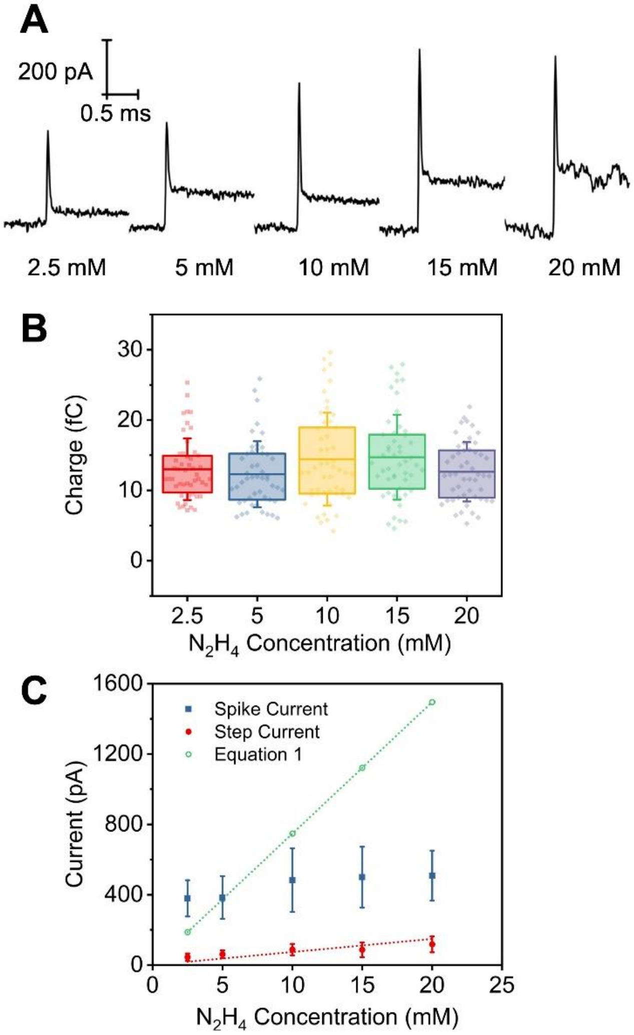

Figure 2.3. Hydrazine concentration-dependent NP collisions.
(A) Representative collision events for 32-nm-diameter Pt NP in various concentrations of hydrazine and 10 mM phosphate buffer (pH 7.5) at 200 mV. (B) Integrated spike charge vs N_2H_4 concentration (the same experimental conditions). (C) Comparison of spike current and step currents with the theoretical diffusion-limited current calculated using Equation 1. The "*n*" values for (B) and (C) are both equal to 50. Datapoints on (B) and (C) are presented as mean ± SD.

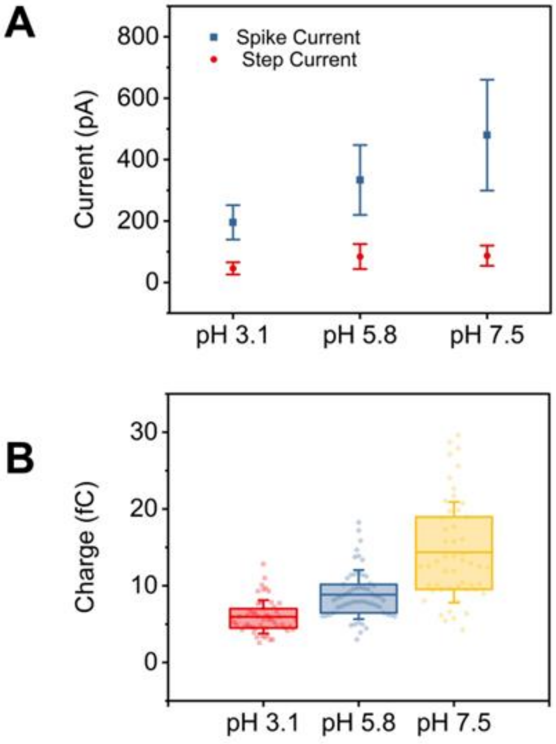

Figure 2.4. pH-dependent NP collisions.
(A) Comparison of spike current and step currents for the same conditions. (B) Integrated spike charge for 32-nm-diameter Pt NPs collision in 10 mM hydrazine in phosphate buffer at various pH values; all at 200 mV. The "*n*" values for (A) and (B) are both 50. Datapoints in (A) are presented as mean ± SD.

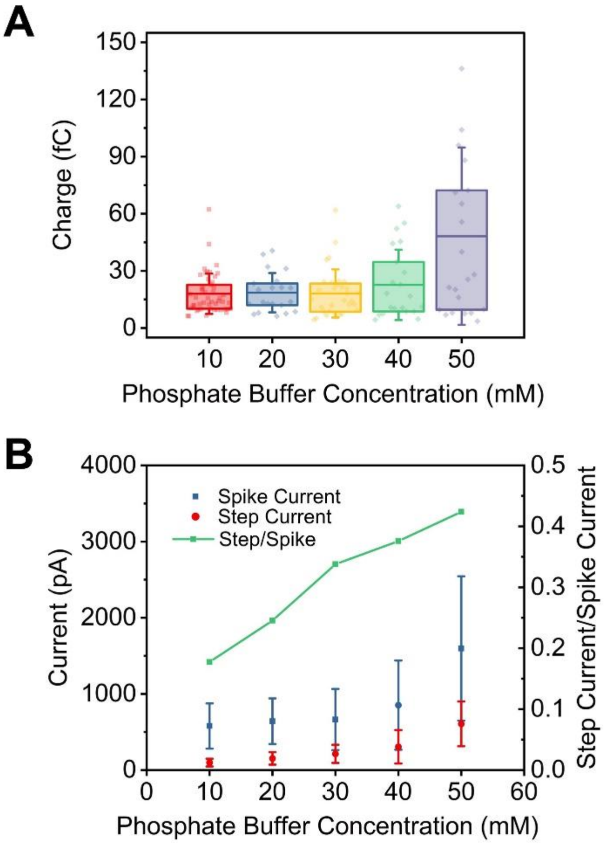

Figure 2.5. Buffer concentration-dependent NP collisions.
(A) Integrated spike charge for 32-nm-diameter Pt NPs collision events in various concentrations of phosphate buffer (all pH 7.5) and 10 mM hydrazine at 200 mV. (B) Comparison of spike and step currents under varied buffer capacity (conditions as A). "Step/Spike" indicates the ratio of step current to spike current. The "*n*" values for 10, 20, 30, 40, and 50 mM phosphate buffer measurements are 49, 21, 32, 22, and 22, respectively. Datapoints on (B) are presented as mean ± SD.

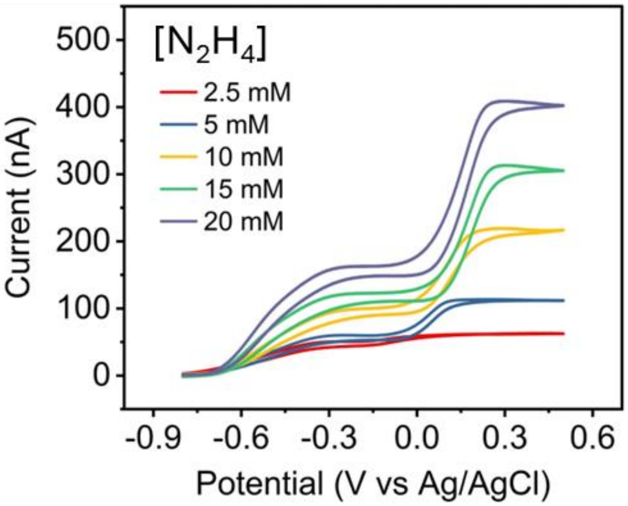

Figure 2.6. Hydrazine oxidation CVs on a Pt UME.
Hydrazine oxidation CVs in a 10 mM phosphate buffer (pH 7.5) on a 25 μm diameter Pt UME for various hydrazine concentrations (as labelled). Scan rate: 100 mV/s.

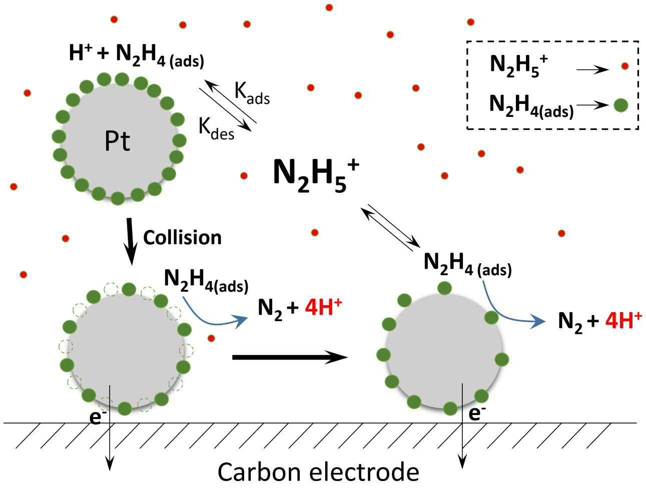

Figure 2.7. Proposed mechanism.
Proposed mechanism for the amperometric current response of single Pt NPs colliding with a carbon UME and catalyzing N_2H_4 oxidation.

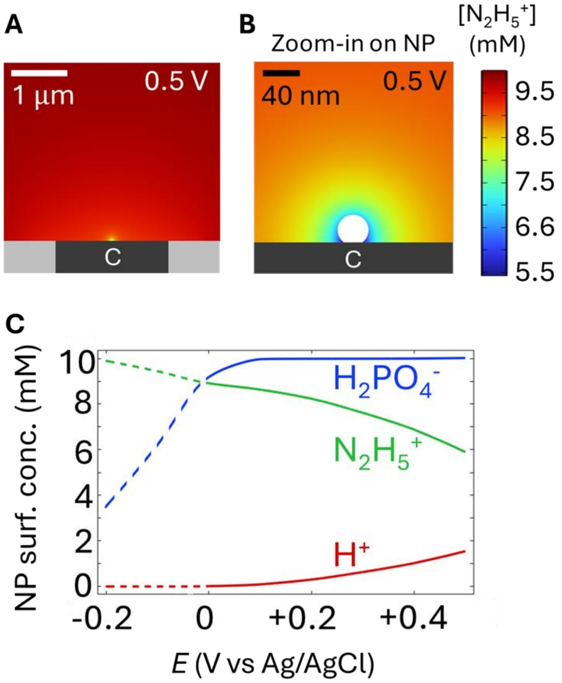

Figure 2.8. Simulated steady-state concentrations of several key species during the collision of single Pt NPs on a 5-μm-diameter CFE in 10 mM hydrazine.

Simulated steady-state concentrations of several key species during the collision of single 32-nm-diameter Pt NPs on a 5-μm-diameter CFE in a 10 mM phosphate buffer (pH=7.5) solution containing 10 mM hydrazine. A zoom-out view (A) and a zoom-in view of (B) of the simulated concentration profile of $N_2H_5^+$ near the NP surface at 0.5 V. (C) A summary plot showing the average surface concentration of three key species: H^+, $N_2H_5^+$, and $H_2PO_4^-$ as a function of potential.

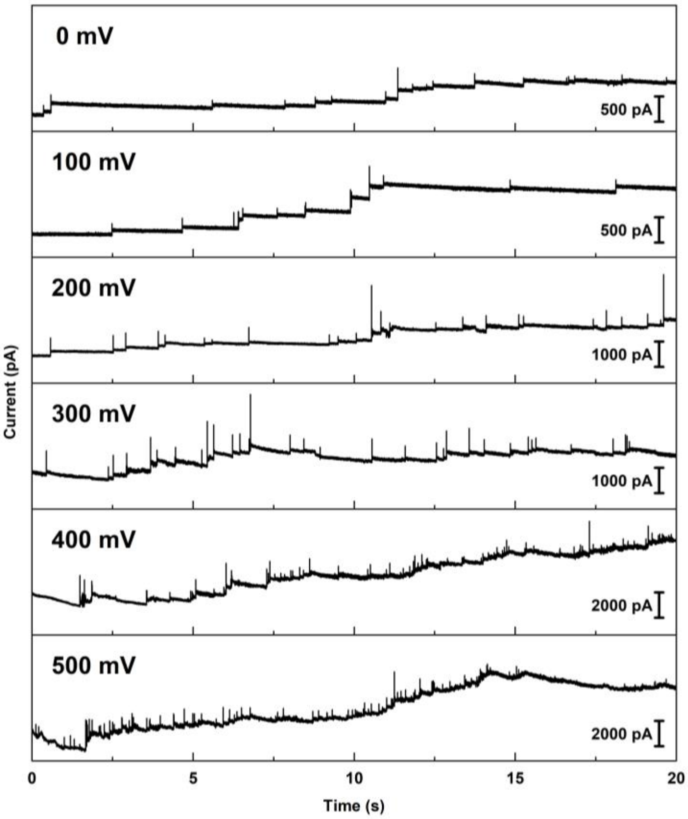

Figure 2.9. Examples collision amperometric traces under different applied potentials. Example traces of Pt NP collision peaks at various potentials (all vs Ag/AgCl). Traces were recorded in 10 mM hydrazine and 10 mM phosphate buffer (pH 7.5) with 32-nm diameter Pt NPs. See **Figure 2.2A** for zoomed-in examples of individual collisions.

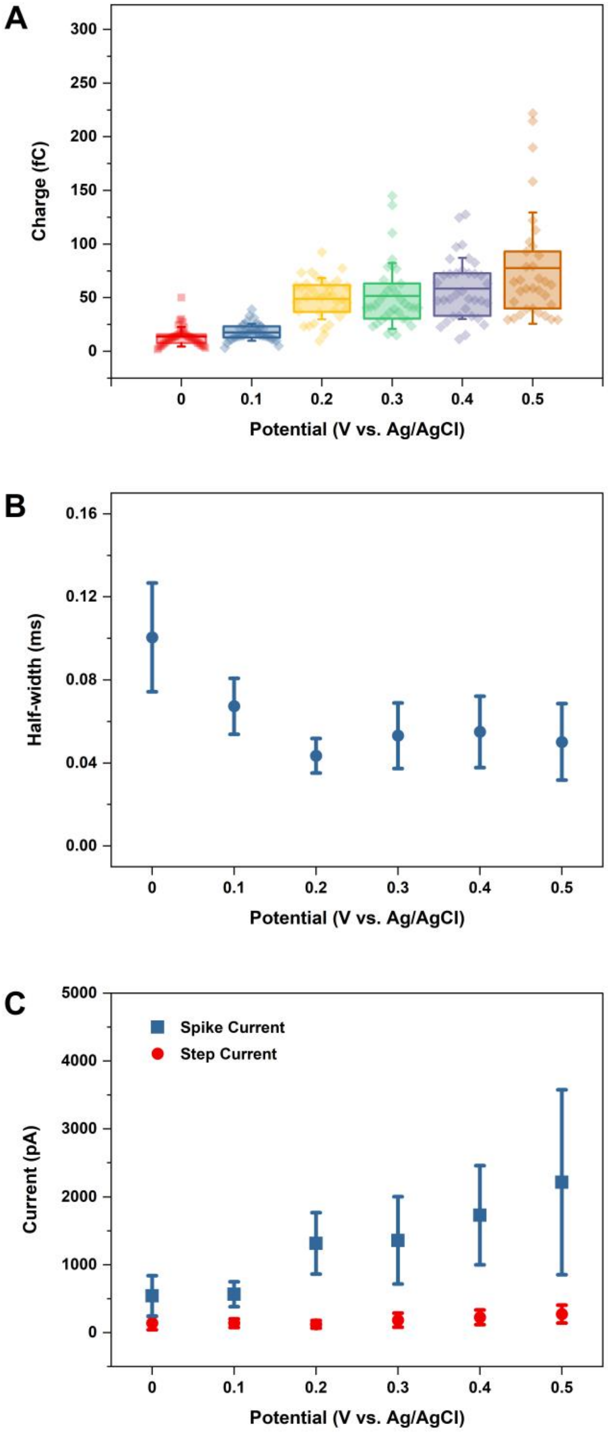

Figure 2.10. NP collision statistics as a function of potential for 52-nm diameter Pt NPs. (A) Integrated spike charge at various applied potentials. (B) Spike current and step current at various potentials. (C) The FWHM of the sharp current spike at various potentials. The "*n*" values for (A) to (C) are all equal to 35. Datapoints in parts B and C are presented by mean ± standard deviation.

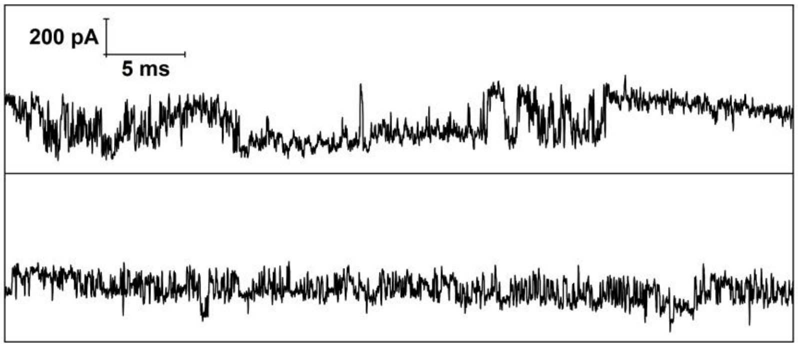

Figure 2.11. Transient current oscillation of colliding nanoparticles.
Recorded transient oscillation. Top trace was recorded in 10 mM hydrazine and 10 mM phosphate buffer (pH 7.5) across 32 nm Pt NP at 400 mV, the bottom trace was recorded at 500 mV. We consider this response us due to transient N_2 nanobubble formation on the surface of colliding Pt NP. The rapid on/off current response is similar to the scatter intensity oscillation observed on the Pd-Ag nanoparticle during nanobubble formation.[66]

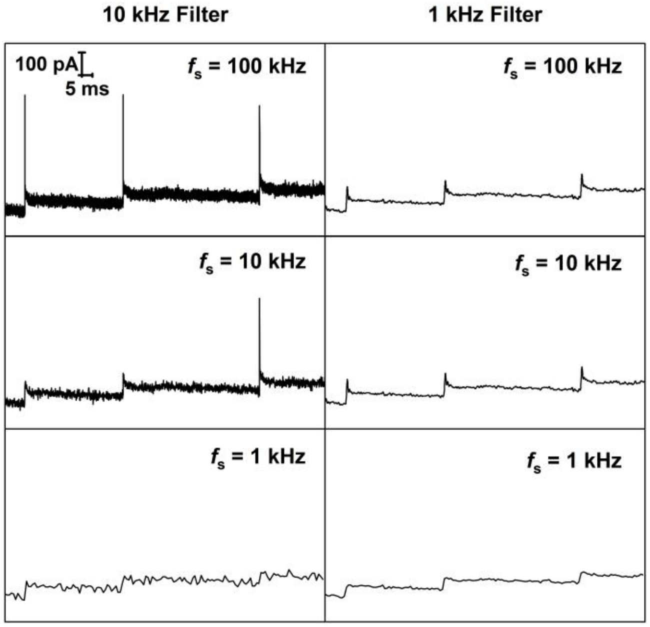

Figure 2.12 Effect of low-pass filter frequency and sampling rate.
Representative NP peaks recorded for 32-nm diameter Pt NP collisions in 10 mM hydrazine and 10 mM phosphate buffer (pH 7.5) acquired with 4-pole lowpass Bessel filter at 10 kHz and 100 kHz sampling rate (f_s). Signals were filtered or down sampled (averaging) using Clampfit software to obtain signals under various low-pass filter frequencies and sampling rates.

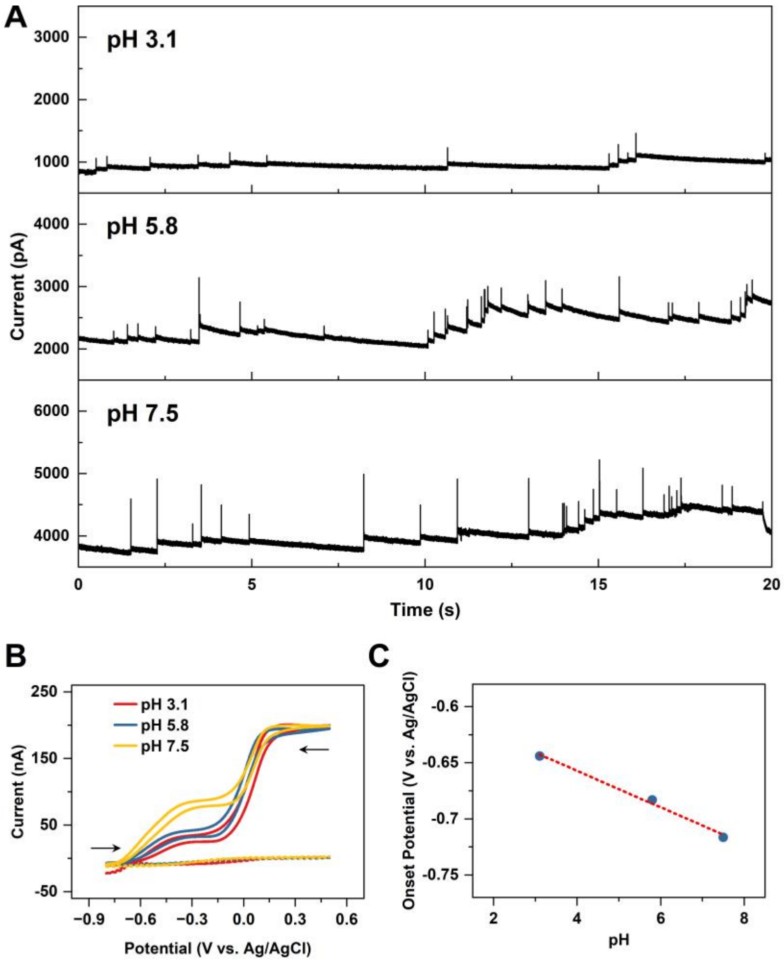

Figure 2.13. pH-dependent NP collisions.
(A) Example traces of 32-nm diameter Pt NP collision events in various pH of hydrazine and 10 mM phosphate buffer (pH as labelled) at 200 mV vs Ag/AgCl. (B) Cyclic voltammograms (CVs) of a 25-µm diameter Pt disk UME in 10 mM phosphate buffer at various pH in the absence (dashed line) and presence (solid line) of 10 mM hydrazine. Scan rate: 100 mV/s. (C) Onset potential for hydrazine oxidation vs. pH. Onset potential was measured from **Figure 2.14B**. The fitted line describes how the potential changed per pH unit. Based on the value of the slope, the pH-dependence of the onset potential for hydrazine oxidation is -16 mV per pH unit, which is not consistent with the Nernstian pH-effect of -59 mV per pH unit.

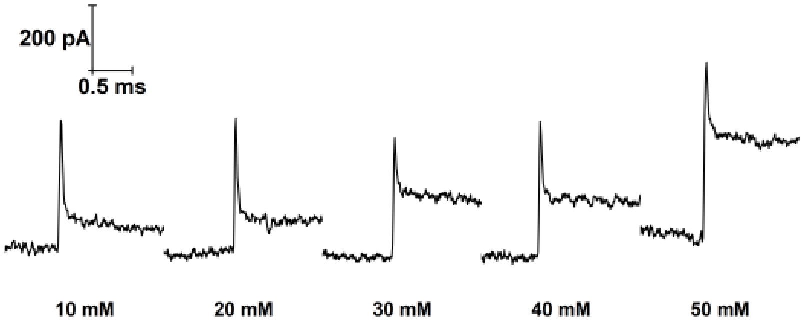

Figure 2.14. Pt NP collisions under different buffer concentrations.
Example collision events recorded at 200 mV vs Ag/AgCl for 32-nm diameter Pt NPs in 10 mM hydrazine in pH 7.5 phosphate buffer with concentrations as labelled.

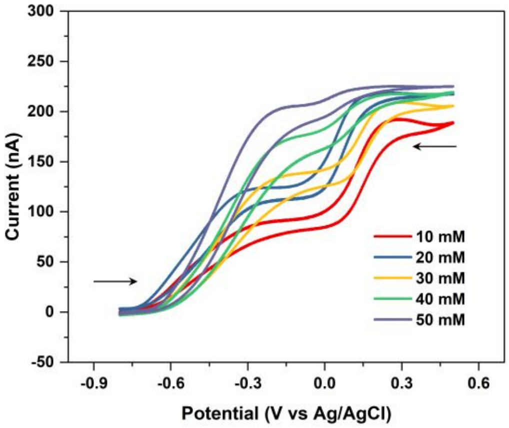

Figure 2.15. Hydrazine oxidation on Pt microelectrodes in phosphate buffer of different concentrations.

CVs for the electrocatalytic oxidation of 10 mM hydrazine in pH 7.5 phosphate buffer solutions of various concentrations on a 25-μm diameter Pt disk UME. Scan rate: 100 mV/s.

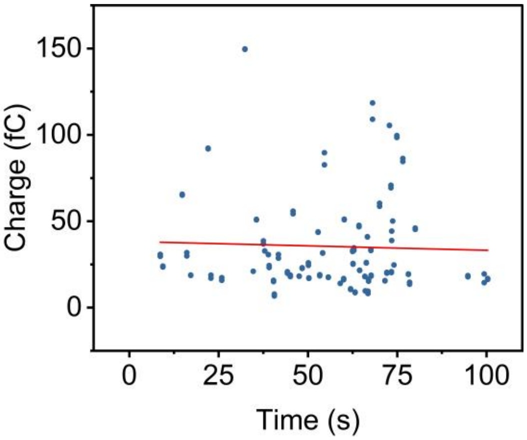

Figure 2.16. Time-Dependent change of spike charge following Pt NPs addition to N_2H_4 solution. Spike charge over time after the addition of Pt NPs to the N_2H_4 solution. The experiment was conducted using 32-nm diameter Pt NP collision events in a solution containing 10 mM hydrazine and 10 mM phosphate buffer at 200 mV vs. Ag/AgCl (n = 132). The R^2 value of the fitted line is 0.00136, indicating no time-dependent spike charge following the addition of Pt NPs to the N_2H_4 solution.

Appendix 2.1

Description of Data Analysis and Curve Fitting

The baselines were measured by averaging 200 data points (2 ms) before the sharp current spike arose. The slow decay step signals were fitted as an exponential decay:

$$f(t) = Ae^{-t/\tau} + C \qquad (S1)$$

where t is the time ($t = 0$ set to be the start of the decay region), A is current at the beginning of decaying, τ is the exponential time constant, and C is a constant. Curves were fitted starting directly after the sharp current spike for 2 ms. Correlation values were >0.99 for all the fitted signals. The fitted curve was then extrapolated and overlapped with the rising side of the spike current to obtain information regarding the spike charge. See red dashed lines in **Figure 2.1** of the main text for examples of the baseline and exponential decay.

Appendix 2.2

Calculation of Coverage of Adsorbed N_2H_4 on Pt NPs Surface

Herein we estimate the fractional coverage of hydrazine on the Pt NP's surface upon collision. We calculate the amount of $N_2H_{4(ads)}$ oxidized, $n_{\mathrm{N_2H_4}}$ (molecules), using Equation S2:

$$n_{\mathrm{N_2H_4}} = Q/q_{\mathrm{e}}n \tag{S2}$$

where Q is the spike charge, q_e is the elementary charge (1.6×10^{-19} C), and n (= 4) is the number of electrons transferred per $N_2H_{4(ads)}$ oxidized.

Knowing the geometric of the Pt NP is ($4\pi\ r_{NP}^2$), where r_{NP} *is* the nanoparticle radius (16 or 26 nm), and Pt atom density (1.3×10^{15} atoms/cm^2)[67] and assuming no roughness, we can calculate the number of Pt atoms (mol) on the surface as

$$n_{\mathrm{Pt}} = 4\pi\, r_{\mathrm{NP}}^2 \times 1.3 \times 10^{15}\ \mathrm{atoms/cm^2} \tag{S3}$$

Thus, the fraction of Pt atoms occupied is

$$\theta_{\mathrm{N_2H_4}} = \frac{n_{\mathrm{N_2H_4}}}{n_{\mathrm{Pt}}} \tag{S4}$$

Appendix 2.3

Description of Simulations

Description of Simulations

We simulated the oxidation of $N_2H_5^+$ on a 32-nm diameter Pt nanoparticle on a 5-µm diameter polyphenol coated carbon-fiber disk electrode on which $N_2H_5^+$ oxidation was also occurring to determine concentration distributions in solution. We used experimentally measured currents to set the applied flux on the surface of Pt nanoparticle and carbon-fiber electrode, as described below in more detail. We simulated the system in the axisymmetric geometry shown in **Figure 2.17**, assuming the Pt nanoparticle (green) is at the center of the carbon-fiber electrode (red). All simulations were performed at a steady state.

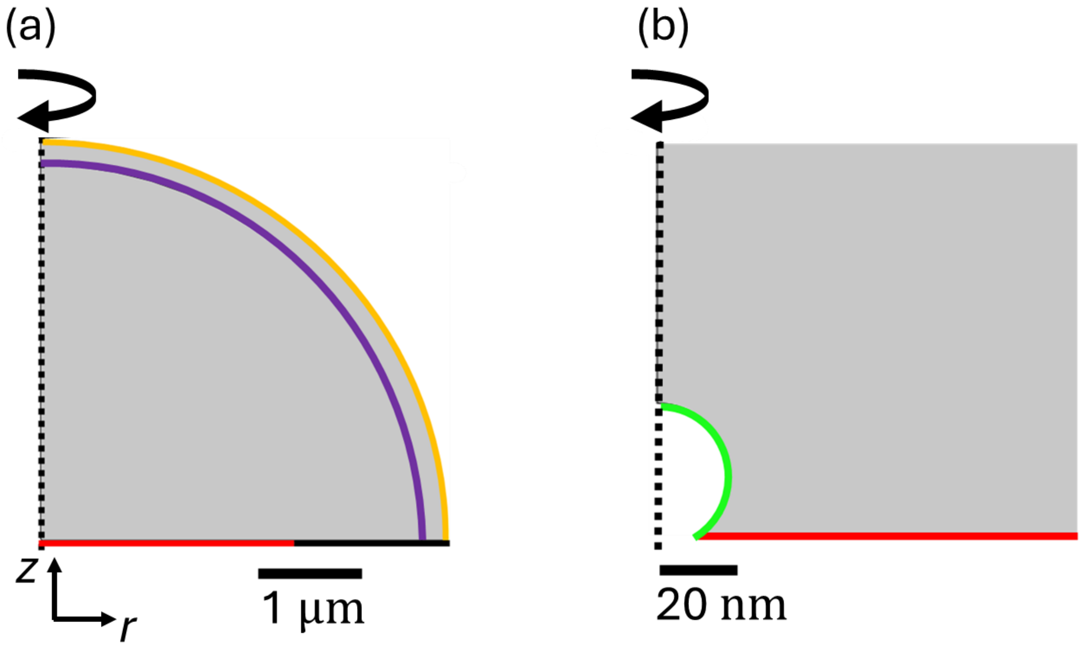

Figure 2.17. 2D-axisymmetric geometry used in simulations.
(a) Entire simulation domain. (b) zoom-in to center of 5-µm diameter carbon-fiber electrode (red) showing 32-nm diameter Pt nanoparticle (green). The solid black and yellow boundaries represent insulator and bulk, respectively, while the dashed line is the axis of symmetry. The region bounded by the purple and yellow lines is the 'infinite elements' domain in which a coordinate transform maps the yellow boundary to infinity.

The concentrations of $N_2H_5^+$, $H_2PO_4^-$, HPO_4^{2-}, N_2 and H^+ in solution were determined through solving the equations for diffusional transport coupled with the buffer equilibrium reaction. Solution of these equations was performed in COMSOL Multiphysics (version 6.1) with chemical reaction engineering add-on package.

Below we provide details of the model equations, boundary conditions, and mesh. To aid in reproduction of the model, our description is supported by an automatically generated COMSOL 'model report', which is included as a separate Supporting Information file, which contains additional details such as the solver parameters.

Solution transport and reactions

H_3PO_4 is a triprotic acid with pK_a values of 2.1, 7.2, and 12.0.[68] The initial pH of the solution is 7.5, while the lowest pH observed during simulations is ~5 (*vide infra*), thus species H_3PO_4 and PO_4^{3-} will not be present in appreciable quantities. As such, we do not simulate these species in our model. Moreover, under these conditions, hydrazine predominantly exists in its protonated form, $N_2H_5^+{}_{(aq)}$ ($pK_{a,\mathrm{hydrazine}}$ = 8.1)[49] and so the deprotonated form was not considered. Under these conditions, water autoprotolysis contributes minimally to changes in H^+ concentration and so is ignored. The transport of the species present in solution is assumed to be by diffusion only and is described by:

$$\frac{d[\mathrm{N_2H_5^+}]}{dt} = D_{\mathrm{N_2H_5^+}}\nabla^2[\mathrm{N_2H_5^+}] \tag{S5}$$

$$\frac{d[\mathrm{H_2PO_4^-}]}{dt} = D_{\mathrm{H_2PO_4^-}}\nabla^2[\mathrm{H_2PO_4^-}] - R \tag{S6}$$

$$\frac{d[\mathrm{HPO_4^{2-}}]}{dt} = D_{\mathrm{HPO_4^{2-}}}\nabla^2[\mathrm{HPO_4^{2-}}] + R \tag{S7}$$

$$\frac{d[\mathrm{H^+}]}{dt} = D_{\mathrm{H^+}}\nabla^2[\mathrm{H^+}] + R \tag{S8}$$

$$\frac{d[\mathrm{N_2}]}{dt} = D_{\mathrm{N_2}}\nabla^2[\mathrm{N_2}] \tag{S9}$$

where the diffusion coefficients have values of $D_{\mathrm{N_2H_5^+}} = 10^{-5}$ cm²/s, $D_{\mathrm{N_2}} = 2 \times 10^{-5}$ cm²/s, $D_{\mathrm{HPO_4^{2-}}} = D_{\mathrm{H_2PO_4^-}} = 8.46 \times 10^{-5}$ cm²/s, and $D_{\mathrm{H^+}} = 9.31 \times 10^{-5}$ cm²/s.[52,69] R is the net forward rate of the buffer protonation/deprotonation reaction S10:

$$\mathrm{H_2PO_4^-} \leftrightharpoons \mathrm{HPO_4^{2-}} + \mathrm{H^+} \tag{S10}$$

which is assumed to be at equilibrium throughout the solution as described by

$$K_{a,2} = \frac{[\mathrm{H^+}][\mathrm{HPO_4^{2-}}]}{[\mathrm{H_2PO_4^-}]} \tag{S11}$$

where $K_{a,2} = 7.5 \times 10^{-8}$ M[52]. The equilibrium was implemented using the 'Equilibrium Reaction' option in COMSOL Multiphysics. Note: in equation S10, we are implicitly assuming that all activities can be replaced by concentrations. We solve equations S5 to S8 in steady state. i.e., the left-hand side is set to zero. To account for the electrode being in a semi-infinite volume of solution, we use the 'infinite element domain' feature, which performs a coordinate transform mapping the bulk boundary and the domain proximal to it toward infinity.

Boundary Conditions

The simulations were set up with boundary conditions that were selected to align with the experimental conditions. At the boundary representing bulk solution, we set the proton concentration from the initial pH, $\mathrm{pH_{init}}$, as $[\mathrm{H^+}]_{\mathrm{init}} = 10^{-\mathrm{pH_{init}}}$. The initial concentration of the protonated hydrazine was set to its initial value, $[\mathrm{N_2H_5^+}]_{\mathrm{init}}$.

The total concentration of the buffer was set to its initial value, $\text{Total Buffer}_{\mathrm{init}} = [\mathrm{HPO_4^{2-}}]_{\mathrm{init}} + [\mathrm{H_2PO_4^-}]_{\mathrm{init}}$ with its speciation determined and from $[\mathrm{H^+}]_{\mathrm{init}}$ and the buffer equilibrium (eq S11) as

$$[\mathrm{HPO_4^{2-}}]_{\mathrm{init}} = \frac{\text{Total Buffer}_{\mathrm{init}} \times K_a}{K_a + [\mathrm{H^+}]_{\mathrm{init}}} \tag{S12}$$

No flux of any species was permitted to pass through the insulator or the axis of symmetry, which for all species i (= $N_2H_5^+$, $H_2PO_4^-$, HPO_4^{2-}, N_2 and H^+), is defined by

$$J_i \cdot \underline{n} = 0 \tag{S13}$$

where J_i is the flux of species i as defined by:

$$J_i = -D_i\nabla[i] \tag{S14}$$

and $\underline{n}$ is the inward pointing unit normal to the interface.

On both electrode surfaces (Pt and C) $H_2PO_4^-$ and HPO_4^{2-} are neither produced nor consumed and thus they are also described by a no normal flux boundary condition (eqn. S13).

On the surface of the carbon-fiber electrode and Pt nanoparticle, we used the experimentally measured currents, i_C and i_{Pt}, taken at appropriate experimental conditions to inform the fluxes of $N_2H_5^+$, N_2, and H^+. For the carbon electrode the current comes from the forward scan of microelectrode voltammetry (**Figure 2.17**), while for Pt nanoparticles we use the average step current (**Figure 2.18**).

Specifically, for each experimental condition (pH, $[\mathrm{N_2H_5^+}]_{\mathrm{init}}$, and Total $\mathrm{Buffer_{init}}$) we take the current density at a 5-mm diameter carbon electrode and Pt nanoparticle as a function of the applied potential, $j(E_{\mathrm{app}})$, from experimental data taken in identical conditions (taking oxidations to be positive current).

We used the stoichiometry of the overall Reaction S15:

$$\mathrm{N_2H_5^+} \rightarrow \mathrm{N_2} + 5\mathrm{H^+} + 4e^- \tag{S15}$$

to determine the surface normal fluxes on carbon-fiber electrode and Pt NP as:

$$J_{\mathrm{N_2}} \cdot \underline{n} = \frac{j(E_{\mathrm{app}})}{4F} \tag{S16}$$

$$J_{\mathrm{N_2H_5^+}} \cdot \underline{n} = -\frac{j(E_{\mathrm{app}})}{4F} \tag{S17}$$

$$J_{\mathrm{H^+}} \cdot \underline{n} = \frac{5j(E_{\mathrm{app}})}{4F} \tag{S18}$$

where the current density j is determined by dividing the current (**Figure 2.17** and **Figure 2.18**) by the relevant surface area, i.e., $j = i_c/\pi(2.5\ \mu\mathrm{m})^2$ and $j = i_{\mathrm{Pt}}/4\pi\ (16\ \mathrm{nm})^2$ on the surface of the CFE and PtNP, respectively.

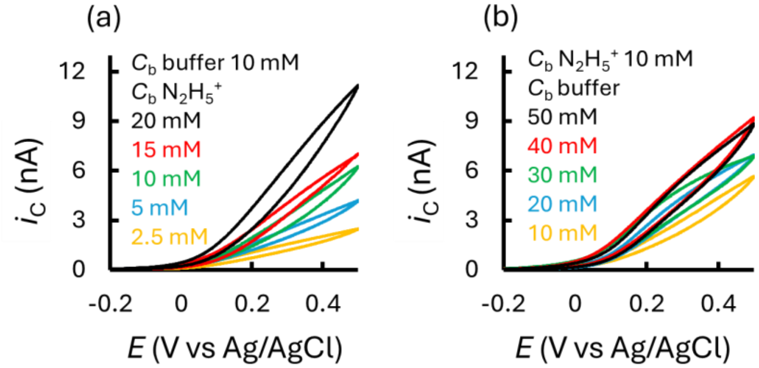

Figure 2.18. Simulated current as a function of potential on 5-µm diameter carbon fiber electrode. (a) Current as a function of potential on 5-µm diameter carbon fiber electrode with 10 mM phosphate buffer, pH 7.5, rate scan = 100 mV/s and different bulk concentrations (C_b) of hydrazine as labelled. (b) Current as a function of potential on 5-µm diameter carbon fiber electrode with 10 mM hydrazine, pH 7.5, rate scan = 100 mV/s and different bulk concentrations of buffer (C_b) as labelled.

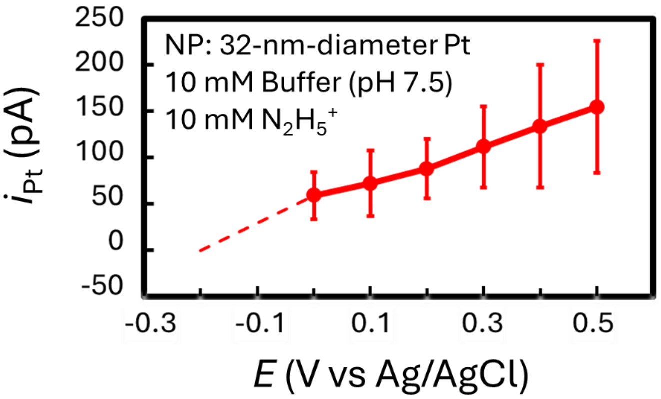

Figure 2.19. Experimentally measured current on the surface of Pt nanoparticles.
10 mM hydrazine, 10 mM phosphate buffer, pH 7.5, rate scan = 100 mV/s. The "n" value for the data is equal to 50 and the datapoints are presented as mean ± SD. The data below 0 V (dashed line) is extrapolated, and it is not based on experiments. (Note, this figure is from the data for step current from **Figure 2.2C** in main manuscript).

Mesh

The equations were subjected to discretization using a mesh that was finest in the vicinity of the NP and the carbon electrode, as depicted in **Figure 2.19**.

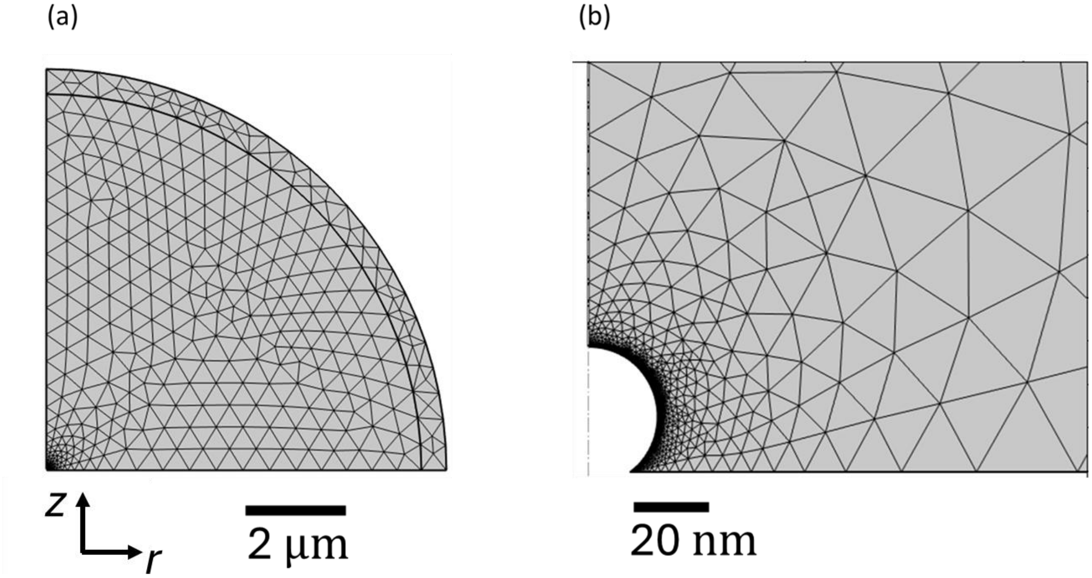

Figure 2.20. Example mesh used for solving the transport equations.
(a) is the mesh for the whole geometry and (b) is a zoomed in image of the mesh around the nanoparticle.

Appendix 2.4

Calculation to rule out the possible contribution from the Cottrell response (diffusion and consumption of the redox) to the observed sharp current spike

This is the equation that describes how the current changes with time according to the Cottrell equation. For a 32 nm diameter NP, it would take ~60 ns for the current to decay to the level of the diffusion limited current.

$$i_{\mathrm{d}}(\mathrm{t}) = nFAD_O C_O^* \left[\frac{1}{(\pi D_O t)^{\frac{1}{2}}} + \frac{1}{r_0} \right] \qquad \text{(S19)}$$

Our observed current spikes are more than 500 times longer (>30 μs)!

Therefore, these spikes cannot be from the Cottrell process (diffusional consumption).

2.6 References

(1) Wordsworth, J.; Benedetti, T. M.; Somerville, S. V.; Schuhmann, W.; Tilley, R. D.; Gooding, J. J. The Influence of Nanoconfinement on Electrocatalysis. *Angew. Chemie - Int. Ed.* **2022**, *61*, e202200755.

(2) Laskowski, F. A. L.; Oener, S. Z.; Nellist, M. R.; Gordon, A. M.; Bain, D. C.; Fehrs, J. L.; Boettcher, S. W. Nanoscale Semiconductor/Catalyst Interfaces in Photoelectrochemistry. *Nat. Mater.* **2020**, *19*, 69–76.

(3) Farka, Z.; Juřík, T.; Kovář, D.; Trnková, L.; Skládal, P. Nanoparticle-Based Immunochemical Biosensors and Assays: Recent Advances and Challenges. *Chem. Rev.* **2017**, *117*, 9973–10042.

(4) Oja, S. M.; Fan, Y.; Armstrong, C. M.; Defnet, P.; Zhang, B. Nanoscale Electrochemistry Revisited. *Anal. Chem.* **2016**, *88*, 414–430.

(5) Pan, S.; Li, X.; Yadav, J. Single-Nanoparticle Spectroelectrochemistry Studies Enabled by Localized Surface Plasmon Resonance. *Phys. Chem. Chem. Phys.* **2021**, *23*, 19120–19129.

(6) Wei, Y.; Zhang, Y.; Pan, J.; Chen, T.; Xing, X.; Zhang, W.; Lu, Z. Plasmon-Enhanced Electrochemiluminescence at the Single-Nanoparticle Level. *Angew. Chemie - Int. Ed.* **2023**, *62,* e202214103.

(7) Chen, P.; Zhou, X.; Shen, H.; Andoy, N. M.; Choudhary, E.; Han, K. S.; Liu, G.; Meng, W. Single-Molecule Fluorescence Imaging of Nanocatalytic Processes. *Chem. Soc. Rev.* **2010**, *39*, 4560–4570.

(8) Hao, R.; Fan, Y.; Howard, M. D.; Vaughan, J. C.; Zhang, B. Imaging Nanobubble Nucleation and Hydrogen Spillover during Electrocatalytic Water Splitting. *Proc. Natl. Acad. Sci. U. S. A.* **2018**, *115*, 5878–6588.

(9) Ma, Y.; Highsmith, A. L.; Hill, C. M.; Pan, S. Dark-Field Scattering Spectroelectrochemistry Analysis of Hydrazine Oxidation at Au Nanoparticle-Modified Transparent Electrodes. *J. Phys. Chem. C* **2018**, *122*, 18603–18614.

(10) Sun, T.; Wang, D.; Mirkin, M. V. Tunneling Mode of Scanning Electrochemical Microscopy: Probing Electrochemical Processes at Single Nanoparticles. *Angew. Chemie - Int. Ed.* **2018**, *57*, 7463–7467.

(11) Sun, T.; Yu, Y.; Zacher, B. J.; Mirkin, M. V. Scanning Electrochemical Microscopy of Individual Catalytic Nanoparticles. *Angew. Chemie - Int. Ed.* **2014**, *53*, 14120–14123.

(12) Saha, P.; Hill, J. W.; Walmsley, J. D.; Hill, C. M. Probing Electrocatalysis at Individual Au Nanorods via Correlated Optical and Electrochemical Measurements. *Anal. Chem.* **2018**, *90*, 12832–12839.

(13) Choi, M.; Siepser, N. P.; Jeong, S.; Wang, Y.; Jagdale, G.; Ye, X.; Baker, L. A. Probing Single-Particle Electrocatalytic Activity at Facet-Controlled Gold Nanocrystals. *Nano Lett.* **2020**, *20*, 1233–1239.

(14) Gao, R.; Edwards, M. A.; Qiu, Y.; Barman, K.; White, H. S. Visualization of hydrogen evolution at individual platinum nanoparticles at a buried interface *J. Am. Chem. Soc.* **2020**, *142*, 8890-8896.

(15) Chen, C. H.; Jacobse, L.; McKelvey, K.; Lai, S. C. S.; Koper, M. T. M.; Unwin, P. R. Voltammetric Scanning Electrochemical Cell Microscopy: Dynamic Imaging of Hydrazine Electro-Oxidation on Platinum Electrodes. *Anal. Chem.* **2015**, *87*, 5782–5789.

(16) Kwon, S. J.; Zhou, H.; Fan, F. -R. F.; Vorobyev, V.; Zhang, B.; Bard, A. J. Stochastic electrochemistry with electrocatalytic nanoparticles at inert ultramicroelectrodes—theory and experiments. *Phys. Chem. Chem. Phys.* **2011**, *13*, 5394– 5402.

(17) Zhang, F.; Edwards, M. A.; Hao, R.; White, H. S.; Zhang, B. Collision and Oxidation of Silver Nanoparticles on a Gold Nanoband Electrode *J. Phys. Chem. C* **2017**, *121*(42), 23564–23573.

(18) Deng, Z.; Renault, C. Detection of Individual Insulating Entities by Electrochemical Blocking. *Curr. Opin. Electrochem.* **2021**, *25*, 1–7.

(19) Xiao, X.; Fan, F. R. F.; Zhou, J.; Bard, A. J. Current Transients in Single Nanoparticle Collision Events. *J. Am. Chem. Soc.* **2008**, *130*, 16669–16677.

(20) Xiao, X.; Pan, S.; Jang, J. S.; Fan, F. R. F.; Bard, A. J. Single Nanoparticle Electrocatalysis: Effect of Monolayers on Particle and Electrode on Electron Transfer. *J. Phys. Chem. C* **2009**, *113*, 14978–14982.

(21) Goines, S.; Dick, J. E. Review—Electrochemistry's Potential to Reach the Ultimate Sensitivity in Measurement Science. *J. Electrochem. Soc.* **2020**, *167*, 037505.

(22) Defnet, P. A.; Han, C.; Zhang, B. Temporally-Resolved Ultrafast Hydrogen Adsorption and Evolution on Single Platinum Nanoparticles. *Anal. Chem.* **2019**, *91*, 4023–4030.

(23) Defnet, P. A.; Anderson, T. J.; Zhang, B. Stochastic Collision Electrochemistry of Single Silver Nanoparticles. *Curr. Opin. Electrochem.* **2020**, *22*, 129–135.

(24) Saw, E. N.; Kratz, M.; Tschulik, K. Time-resolved impact electrochemistry for quantitative measurement of single-nanoparticle reaction kinetics *Nano Research* **2017**, *10*, 3680–3689.

(25) Bentley, C. L.; Kang, M.; Unwin, P. R. Time-Resolved Detection of Surface Oxide Formation at Individual Gold Nanoparticles: Role in Electrocatalysis and New Approach for Sizing by Electrochemical Impacts. *J. Am. Chem. Soc.* **2016**, *138*, 12755–12758.

(26) Han, C.; Hao, R.; Fan, Y. S.; Edwards, M. A.; Gao, H. F.; Zhang, B. Observing Transient Bipolar Electrochemical Coupling on Single Nanoparticles Translocating through a Nanopore. *Langmuir* **2019**, *35*, 7180– 7190.

(27) Li, M.; Ge, Z.; Zhang, S.; He, P.; Gu, Y.; Qi, L.; Shao, Y. Electrocatalytic Reduction of Hydrogen Peroxide by Pd−Ag Nanoparticles Based on the Collisional Approach. *ChemElectroChem* **2018**, *5*, 3021–3027.

(28) Roehrich, B.; Sepunaru, L. Nanoimpacts at Active and Partially Active Electrodes: Insights and Limitations. *Angew. Chemie - Int. Ed.* **2020**, *59*, 19184–19192.

(29) Zhang, Y.; Feng, T.; Xu, M.; Tang, Q.; Zhang, M. Observing Single Hollow Porous Carbon Catalyst Collisions for Oxygen Reduction at Gold Nanoband Electrode. *ChemPhysChem* **2019**, *20*, 529–532.

(30) Zhang, Y.; Robinson, D. A.; McKelvey, K.; Ren, H.; White, H. S.; Edwards, M. A. A High-Pressure System for Studying Oxygen Reduction During Pt Nanoparticle Collisions. *J. Electrochem. Soc.* **2020**, *167*, 166507.

(31) Zhang, F.; Defnet, P. A.; Fan, Y.; Hao, R.; Zhang, B. Transient Electrocatalytic Water Oxidation in Single-Nanoparticle Collision. *J. Phys. Chem. C* **2018**, *122*, 6447–6455.

(32) Zhou, H.; Fan, F. R. F.; Bard, A. J. Observation of Discrete Au Nanoparticle Collisions by Electrocatalytic Amplification Using Pt Ultramicroelectrode Surface Modification. *J. Phys. Chem. Lett.* **2010**, *1*, 2671–2674.

(33) Zhou, H.; Park, J. H.; Fan, F. R. F.; Bard, A. J. Observation of Single Metal Nanoparticle Collisions by Open Circuit (Mixed) Potential Changes at an Ultramicroelectrode. *J. Am. Chem. Soc.* **2012**, *134*, 13212–13215.

(34) Ortiz-Ledón, C. A.; Zoski, C. G. Pt Nanoparticle Collisions Detected by Electrocatalytic Amplification and Atomic Force Microscopy Imaging: Nanoparticle Collision Frequency, Adsorption, and Random Distribution at an Ultramicroelectrode Surface. *Anal. Chem.* **2017**, *89*, 6424–6431.

(35) Rees, N. V.; Compton, R. G. Carbon-Free Energy: A Review of Ammonia- and Hydrazine-Based Electrochemical Fuel Cells. *Energy Environ. Sci.* **2011**, *4*, 1255–1260.

(36) Aldous, L.; Compton, R. G. The Mechanism of Hydrazine Electro-Oxidation Revealed by Platinum Microelectrodes: Role of Residual Oxides. Phys. *Chem. Chem. Phys.* **2011**, *13*, 5279–5287.

(37) Dasari, R.; Robinson, D. A.; Stevenson, K. J. Ultrasensitive Electroanalytical Tool for Detecting, Sizing, and Evaluating the Catalytic Activity of Platinum Nanoparticles. *J. Am. Chem. Soc.* **2013**, *135*, 570–573.

(38) Alligrant, T. M.; Anderson, M. J.; Dasari, R.; Stevenson, K. J.; Crooks, R. M. Single Nanoparticle Collisions at Microfluidic Microband Electrodes: The Effect of Electrode Material and Mass Transfer. *Langmuir* **2014**, *30*, 13462–13469.

(39) Jung, A. R.; Lee, S.; Joo, J. W.; Shin, C.; Bae, H.; Moon, S. G.; Kwon, S. J. Potential-Controlled Current Responses from Staircase to Blip in Single Pt Nanoparticle Collisions on a Ni Ultramicroelectrode. *J. Am. Chem. Soc.* **2015**, *137*, 1762–1765.

(40) Jiao, X.; Batchelor-Mcauley, C.; Lin, C.; Kätelhön, E.; Tanner, E. E. L.; Young, N. P.; Compton, R. G. Role of Nanomorphology and Interfacial Structure of Platinum Nanoparticles in Catalyzing the Hydrogen Oxidation Reaction. *ACS Catal.* **2018**, *8*, 6192–6202.

(41) Chang, X.; Batchelor-McAuley, C.; Compton, R. G. Hydrogen Peroxide Reduction on Single Platinum Nanoparticles. *Chem. Sci.* **2020**, *11*, 4416–4421.

(42) El Arrassi, A.; Liu, Z.; Evers, M. V.; Blanc, N.; Bendt, G.; Saddeler, S.; Tetzlaff, D.; Pohl, D.; Damm, C.; Schulz, S.; Tschulik, K. Intrinsic Activity of Oxygen Evolution Catalysts Probed at Single CoFe2O4 Nanoparticles. *J. Am. Chem. Soc.* **2019**, *141*, 9197–9201.

(43) Karp, S.; Meites, L. The Voltammetric Characteristics and Mechanism of Electroöxidation of Hydrazine. *J. Am. Chem. Soc.* **1962**, *84*, 906–912.

(44) Kleijn, S. E. F.; Serrano-Bou, B.; Yanson, A. I.; Koper, M. T. M. Influence of Hydrazine-Induced Aggregation on the Electrochemical Detection of Platinum Nanoparticles. *Langmuir* **2013**, *29*, 2054–2064.

(45) Castañeda, A. D.; Alligrant, T. M.; Loussaert, J. A.; Crooks, R. M. Electrocatalytic Amplification of Nanoparticle Collisions at Electrodes Modified with Polyelectrolyte Multilayer Films. *Langmuir* **2015**, *31*, 876–885.

(46) Castañeda, A. D.; Robinson, D. A.; Stevenson, K. J.; Crooks, R. M. Electrocatalytic Amplification of DNA-Modified Nanoparticle Collisions via Enzymatic Digestion. *Chem. Sci.* **2016**, *7*, 6450–6457.

(47) Zhang, Y.; Mao, J.; Ji, W.; Feng, T.; Fu, Z.; Zhang, M.; Mao, L. Collision of Aptamer/Pt Nanoparticles Enables Label-Free Amperometric Detection of Protein in Rat Brain. *Anal. Chem.* **2019**, *91*, 5654–5659.

(48) Qiu, X.; Tang, H.; Dong, J.; Wang, C.; Li, Y. Stochastic Collision Electrochemistry from Single Pt Nanoparticles: Electrocatalytic Amplification and MicroRNA Sensing. *Anal. Chem.* **2022**, *94*, 8202–8208.

(49) *CRC Handbook of Chemistry and Physics, 95th ed.*; Haynes, W. M., Ed.; CRC Press: Boca Raton, FL, **2014**.

(50) Rosca, V.; Duca, M.; DeGroot, M. T.; Koper, M. T. M. Nitrogen Cycle Electrocatalysis. *Chem. Rev.* **2009**, *109*, 2209–2244.

(51) Percival, S. J.; Zhang, B. Fast-Scan Cyclic Voltammetry Allows Determination of Electron-Transfer Kinetic Constants in Single Nanoparticle Collision. *J. Phys. Chem. C* **2016**, *120*, 20536–20546.

(52) Arulrajan, A. C.; Renault, C.; Lai, S. C. S. How Changes in Interfacial pH Lead to New Voltammetric Features: The Case of the Electrochemical Oxidation of Hydrazine. *Phys. Chem. Chem. Phys.* **2018**, *20*, 11787–11793.

(53) Strein, T. G.; Ewing, A. G. Characterization of Submicron-Sized Carbon Electrodes Insulated with a Phenol-Allylphenol Copolymer. *Anal. Chem.* **1992**, *64*, 1368–1373.

(54) Oja, S. M.; Robinson, D. A.; Vitti, N. J.; Edwards, M. A.; Liu, Y.; White, H. S.; Zhang, B. Observation of Multipeak Collision Behavior during the Electro-Oxidation of Single Ag Nanoparticles. *J. Am. Chem. Soc.* **2017**, *139*, 708–718.

(55) Robinson, D. A.; Edwards, M. A.; Ren, H.; White, H. S. Effects of Instrumental Filters on Electrochemical Measurement of Single-Nanoparticle Collision Dynamics. *ChemElectroChem* **2018**, *5*, 3059–3067.

(56) Gao, R.; Edwards, M. A.; Harris, J. M.; White, H. S. Shot Noise Sets the Limit of Quantification in Electrochemical Measurements. *Curr. Opin. Electrochem.* **2020**, *22*, 170–177.

(57) Ma, H.; Zhong, C. B.; Ying, Y. L.; Long, Y. T. Seeing Is Not Believing: Filtering Effects on Random Nature in Electrochemical Measurements of Single-Entity Collision. *ACS Meas. Sci. Au* **2022**, *2*, 325–331.

(58) Lewis, T. H.; Zhang, B. Nanoparticle Adhesion and the Role of Nanobubbles in Single-Particle Collision Electrochemistry. *J. Phys. Chem. C* **2024**, *128*, 31, 13074–13082.

(59) Robinson, D. A.; Duay, J.; Kondajji, A. M.; Stevenson, K. J. Mechanistic Aspects of Hydrazine-Induced Pt Colloid Instability and Monitoring Aggregation Kinetics with Nanoparticle Impact Electroanalysis. *Faraday Discuss*. **2016**, *193*, 293–312.

(60) Robinson, D. A.; Kondajji, A. M.; Castañeda, A. D.; Dasari, R.; Crooks, R. M.; Stevenson, K. J. Addressing Colloidal Stability for Unambiguous Electroanalysis of Single Nanoparticle Impacts. *J. Phys. Chem. Lett.* **2016**, *7*, 2512–2517.

(61) Watkins, J. J.; Chen, J.; White, H. S.; Abruña, H. D.; Maisonhaute, E.; Amatore, C. Zeptomole Voltammetric Detection and Electron-Transfer Rate Measurements Using Platinum Electrodes of Nanometer Dimensions. *Anal. Chem.* **2003**, *75*, 3962–3971.

(62) Bard, A. J.; Faulkner, L. J. Electrochemical Methods: Fundamentals and Applications, 2nd ed.; Wiley: New York, **2001**.

(63) Yue, G.; Zeng, Q.; Huang, J.; Wang, L. Mechanism Studies of Hydrazine Electro-Oxidation by a Platinum Ultramicroelectrode: Effects of Supporting Electrolytes. *J. Electrochem. Soc.* **2018**, *818*, 19–25.

(64) Kim, K. J.; Han, Y.; Kwon, S. J. Exploring Single-Entity Electrochemistry beyond Conventional Potential Windows: Mechanistic Insights into Hydrazine/Hydrazinium Ion Oxidation. *Nanoscale* **2024**, *16*, 18488–18493.

(65) Alberas, D. J.; Kiss, J.; Liu, Z. M.; White, J. M. Surface Chemistry of Hydrazine on Pt(111). *Surf. Sci.* **1992**, *278*, 51–61.

(66) Li, S.; Du, Y.; He, T.; Shen, Y.; Bai, C.; Ning, F.; Hu, X.; Wang, W.; Xi, S.; Zhou, X. Nanobubbles: An Effective Way to Study Gas-Generating Catalysis on a Single Nanoparticle. *J. Am. Chem. Soc.* **2017**, *139* (40), 14277–14284.

(67) Doña Rodríguez, J. M.; Herrera Melián, J. A.; Pérez Peña, J. Determination of the Real Surface Area of Pt Electrodes by Hydrogen Adsorption Using Cyclic Voltammetry. *J. Chem. Educ.* **2000**, *77*, 1195–1197.

(68) Pourbaix, M. *Atlas of Electrochemical Equilibria in Aqueous Solutions*, 2d English ed.; National Association of Corrosion Engineers: Houston, Texas, **1974**.

(69) Cadogan, S. P.; Maitland, G. C.; Trusler, J. P. M. Diffusion Coefficients of CO_2 and N_2 in Water at Temperatures between 298.15 K and 423.15 K at Pressures up to 45 MPa. *J. Chem. Eng. Data* **2014**, *59* (2), 519–525.

CHAPTER 3 TRANSIENT BIPOLAR AMPEROMETRIC BEHAVIOR OF SINGLE METAL NANOPARTICLES[*]

3.1 *Introduction*

The recent two decades have seen an increasing interest in probing the electrochemical response of single metal nanoparticles.[1-3] This is in part due to the desire to develop ultrasensitive biosensors using metal nanoparticles as a novel electrochemical label.[4-8] Some studies have been motivated by the possibility of correlating the electrochemical and electrocatalytic property of nanoparticles with their size and structure.[9-14] We[15-17] and others[18-20] have been interested in probing the transient electrochemical behavior of single nanoparticles as a way to better understand the dynamic nature of the electrochemical interface.[21,22]

Some pioneering work in the field of single-entity collision electrochemistry includes the study of discrete current blockage on an ultramicroelectrode (UME) by particle adsorption,[23] current enhancement due to effect of electrocatalytic amplification,[24] and the direct electrolysis of single nanoparticles.[25] Due to the small size of single nanoparticles and their fast diffusional movement, their electrochemical current signal is often in the picoampere (pA) range lasting micro- or milliseconds.[26] As such, accurately recording their electrochemical response may represent an analytical challenge and usually requires the use of a UME (e.g., Pt,[27] Au,[28] C,[29] Hg,[30] or other conductive materials[31,32]) and highly sensitive electronics with low noise and sufficient bandwidth.[33] While other methods may be considered,[34-36] a key recording method has been chronoamperometry, which gives μs time resolution depending on the electrode characteristics and instrument limitation.

In our previous work,[37] we described another method to probe the transient electrochemistry behavior of single Ag nanoparticles *wirelessly* with a nanopore. In that paper, we used a glass nanopipette[38] to study single 40 nm Ag nanoparticles passing through the pipette pore under a small DC voltage bias. In addition

---

[*] This chapter is adapted with permission from:
Gao, H.[+]; Wan, R.[+] ([+]Equal Contribution); Zhang, B. Transient Bipolar Amperometric Behavior of Single Metal Nanoparticles. (Under review)

to observing conventional ionic current blockage signals at voltages lower than 1.0 V, we detected very large current blockages at voltages between 1.0 and 2.5 V (*all voltages are applied from inside the pipette pore to the outside*), which suggests the formation of single H_2 nanobubbles from the coupled redox reactions across the two extremities of the same nanoparticle (e.g., oxidation of Ag metal, $Ag + Br^- = AgBr + 1e^-$, coupled to the reduction of protons, $H^+ + 1e^- = 1/2H_2$). Being able to directly observe the electrochemical response of a single nanoparticle without making a wire connection is both interesting and significant not only because one can simplify the experimental setup for particle detection, one may also consider exerting much higher driving voltages on the particle to induce redox reactions that may not be feasible under normal conditions on an UME. For example, a chemically or biologically modified Au or Pt nanoparticle may lose its electrocatalytic activity during particle detection on a UME with electrocatalytic amplification.[39] We may be able to probe its bipolar electrochemistry response with a nanopore and a higher voltage bias to overcome its activation barrier.

During our previous study with a glass nanopipette, we encountered a critical challenge for prolonged recording of particle translocation events: the pipette tends to be clogged fairly quickly after the first several minutes. The clogging issue is likely due to the restricted internal volume of the glass nanopipette (**Figure 3.1**, upper panel) and the 0.1 M HCl used inside the pipette. Once a Ag nanoparticle enters the pipette, it is likely that the citrate ligands will become protonated[40] or detached from the particle surface leading to particle aggregation or irreversible adsorption on the inner pore walls.

To address this issue, we have developed a new type of glass nanopore at the end of a glass micropipette (**Figure 3.1**, lower panel). A glass microbulb (GMB) nanopore is formed by blowing a small, micron-sized glass bulb from a closed glass micropipette followed by milling a single nanopore on the ultrathin glass walls (see details in *experimental section*). Compared with a nanopipette, a GMB nanopore has a large internal volume, e.g., between 30 to 60 μm in diameter, and a thin glass membrane <500 nm making it significantly more resistant to pore clogging. With these GMB pores, we have been able to continuously record thousands of particle translocation events using the same chemical conditions as in our previous study. Importantly, their high stability and longevity have allowed us to study the bipolar electrochemical property of single metal nanoparticles with great details that have been unachievable before using pipette pores.

With our current experimental setting (i.e., 0.1 M HCl inside the pore and 0.01 M NaBr outside), the bipolar amperometric response of a Ag nanoparticle passing through a thin glass nanopore is characterized by a transient biphasic current signal. In general, it starts with a small, yet noticeable upward current peak followed by a more significant downward current peak before returning to the baseline. With its relatively small magnitude (between 1% and 3% at voltages between -1.5 and -4.0 V), the upward current peak is believed to be caused by an increase in the local ionic conductivity due to the surface charges on the nanoparticle as it approaches the pore orifice. The downward current peak, on the other hand, increases in current magnitude from ~3.8% at -1.5 V to ~20% at -5.0 V. The separation between the upward peak and the downward peak is seen to decrease from 324 ms at -1.5 V to 2.5 ms at -5.0 V. This suggests the applied voltage is effective in pulling particles into the nanopore. Interestingly, while a somewhat smooth current signal is seen at -1.5 and -2.0 V, an oscillating current signal is seen at higher negative voltages after the current reaches the minimum value on the downward peak but before it reaches the baseline. The oscillating current is seen to superimpose on the increasing current and lasts ~50 ms indicating slow particle translocation. The large amplitude of the current blockage, the oscillating current, and the slow movement of the particle (once it reaches the maximum current blockage) all suggest that a nanobubble is formed when the particle reaches a certain location, which likely undergoes repeated formation and dissolution during its translocation through the glass nanopore.

A more detailed characterization of the translocation process and a better understanding of the bipolar electrochemistry behavior of single metal nanoparticles will likely benefit our future research in designing single-entity electrochemical biosensors using metal nanoparticles as a unique biolabeling agent. In addition to its application in studying bipolar electrochemistry of single nanoparticles, we believe our GMB nanopore can be a useful analytical tool for more general use in resistive pulse sensing of nanoparticles[41,42] and many other studies.[43]

3.2 *Experimental Section*

3.2.1 *Chemicals and Materials*

All of the following chemicals and materials were used as received from the manufacturers. Potassium chloride (KCl, Fisher Chemical, 99.1%), hydrochloric acid (HCl, Fisher Scientific, 1N), sodium bromide (NaBr, Aldrich, >99%), 80 ± 4 nm diameter Ag nanoparticles (sodium citrate capped, dispersed in 2 mM citrate, nanoComposix). All aqueous solutions were prepared using deionized water (>18 MΩ cm) from a Barnstead Nanopure water purification system.

3.2.2 *Fabrication of Glass Microbulb*

Figure 3.2A depicts the two-step fabrication process of a glass microbulb (GMB). First, a glass micropipette was prepared by pulling borosilicate capillary (0.69 mm I.D./1.2 mm O.D.) on a P-2000 laser puller (Sutter) with a two-line pulling program: heat = 350, filament = 4, velocity = 30, delay = 140, pull = 60; heat = 310, filament = 2, velocity = 30, delay = 140, pull = 60. Second, the GMB was fabricated on an MF-83 patch-pipette microforge (Narishige) that uses a Pt wire as heating filament to melt glass. The pulled borosilicate pipette was mounted on an electrode holder. The pipette was heated with heat value of 55 on the microforge for several seconds to form a complete seal at the pipette tip. The back end of the pipette was then connected to a N_2 gas tank allowing pressurized N_2 (~ 20 to 30 psi) to be directed into the pipette while the sealed pipette was heated with heat value of 60 until the glass wall at the pipette tip fully expanded to form a spherical GMB (about 40-60 μm in diameter), as shown in **Figure 3.2B, C, E**.

The GMB was later coated with a thin carbon film (~100 nm) using a 0.8 mm diameter (0.4 g/m) carbon fiber filament (Ted Pella) in a SPI-Module sputter coater (SPI Supplies). A single nanopore was fabricated by focused-ion beam (FIB) milling[44] on an XL830 dual-beam FIB/SEM (FEI); a beam current of 1 pA and a magnification of 150,000x were consistently utilized in order to achieve reproducible pore diameters and geometries. Subsequent to FIB milling, the carbon layer was removed in a Femto plasma cleaning system (Diener Electronic) using a power of 40 W and an oxygen pressure of 150 mtorr with an etch time of 30 minutes. The nanopore was then characterized by SEM and electrochemical methods.

3.2.3 Cell Configuration and Data Acquisition

All the electrochemical experiments were performed using a Dagan potentiostat (Chem-Clamp, Dagan) or an Epsco PSR-12-50 DC regulated power supply (Epsco Incorporated) connected with a Keithley 427 current amplifier. Amperometry data were recorded on a Dell PC through a Digidata 1322A digitizer (Axon Instruments). The rise time was set to 0.3 milliseconds. Amperometric traces were recorded using Axoscope 10.4 software (Molecular Devices) with a 50 kHz sampling frequency. All experiments were performed using a two-electrode setup placed in a lab-built Faraday cage. All potentials reported herein are the potentials applied onto an Ag/AgCl wire quasi-reference electrode (QRE) inside the GMB versus a Pt QRE placed in the bulk solution. SEM imaging was performed on an XL830 dual-beam FIB/SEM (FEI) operating at a 5 kV accelerating potential. All samples were sputter-coated with a thin layer of carbon prior to their SEM examination.

3.3 Results and Discussions

3.3.1 Fabrication and Characterization of GMB

Borosilicate glass is the material of choice for this study due to its lower softening temperature[45] and the desire to precisely heat and expand the glass tip with a 100-µm-diameter Pt wire as the heating filament. By adjusting the glass-filament distance, the heating temperature of the filament, and the heating time, one can control the amount of heat delivered onto the glass microtip. This, along with a suitable gas pressure applied from inside the pipette, e.g., 15 psi, allows one to expand the glass pipette tip into a microbulb and significantly reduce the thickness of the glass wall from ~3-5 µm to <200 nm. A sub-micron glass wall thickness is preferred for constructing glass nanopores with high sensitivity and mechanical stability for studying single nanoparticles.[46]

Compared with conventional glass micro- or nanopipettes, a nanopore fabricated on a GMB has a significantly large internal volume (**Figure 3.2B, E**). When NPs translocate through a GMB nanopore into the interior, it is expected that they will pass the short sensing zone and quickly enter the large internal volume. This makes them less likely to collide with and stick onto the glass pore walls (*vide infra*) compared with the long neck of a glass nanopipette. This makes GMB nanopores an attractive analytical platform for continuous nanoparticle sensing applications.

We use FIB milling to prepare a circular nanopore along the equator of a GMB.[47] Both the bright field micrograph (**Figure 3.2B**) and the SEM image (**Figure 3.2C**) show a round GMB with an outer diameter of ~50 μm. From the optical image, one can also see the well expanded glass structure and the ultrathin glass walls compared to un-expanded regions on the same pipette. The geometry of a GMB can be assumed as a hollow microsphere with an overall diameter D and the thickness of the glass membrane L. While it is difficult to measure the thickness of the glass membrane with optical microscopy, one can estimate the GMB diameter from an optical micrograph. **Figure 3.2D** shows an SEM micrograph of the elliptical pore with a minor axis of 120 nm. The elliptical pore shape is likely due to sample charging and slight sample drift during FIB milling.[48] To examine the quality and thickness of the glass membrane walls, we also milled a GMB in half along the equator (**Figure 3.2E**). The SEM image of cross section of a GNB was taken at a 52° angle from perpendicular (**Figure 3.2F**). The thickness of the glass membrane in **Figure 3.2F** was seen to be around 500 nm.

Similar to how one characterizes other types of nanopores,[49] a current-voltage (*i*-*V*) response can be readily obtained to evaluate the basic performance of a GMB pore in sensing and transport measurements. **Figure 3.2G** shows the *i*-*V* response of the GMB pore shown in **Figure 3.2D** measured in 100 mM KCl between -0.5 and +0.5 V at room temperature. A linear *i*-*V* response was obtained suggesting that the ionic current response is largely ohmic and there is no apparent rectification effect to the ionic current.[50] This is expected due to the short pore length and the more cylindrical pore shape compare to the ultralong, conical pores found in glass nanopipettes.[51] With GMB pores characterized with microscopy and voltammetry, we are ready to use them to study single nanoparticle translocation and bipolar electrochemistry.

3.3.2 Nanoparticle Translocation and Bipolar Electrochemistry

A key goal in developing these GMB nanopores has been the study of *transient bipolar electrochemical behavior* of single metal nanoparticles, especially Ag particles. Our previous study used glass and quartz nanopipettes,[37] which allowed us to observe unusually large current blockages when single Ag nanoparticles translocate into a pipette pore containing an acid solution (e.g., 0.1 M HCl). These large current signals are likely caused by the coupled bipolar electrochemical processes: the oxidation of Ag and H_2O on one end of the Ag nanoparticle and the reduction of H^+ and H_2O on the opposite end, which generate gaseous molecules (H_2 and O_2) and their nanobubbles blocking the ionic pathway of the pipette pore.

With the harsh chemical environment inside the pore (i.e., pH~1), however, a pipette pore is easily clogged due to nanoparticles losing their chemical stability and adhering to the inner glass walls once they enter the pipette. As a result, only a few particle translocation events can be seen in a normal amperometric recording lasting a few hundred seconds. As an example, **Figure 3.3A** shows a 380-second current-time recording of a 150-nm diameter quartz nanopipette detecting 80 nm Ag nanoparticles. Several distinct nanoparticle translocation events can be seen, each having a large transient current pulse suggesting the formation of a gas nanobubble from the coupled electrochemical reactions across the nanoparticle.[37] Importantly, one can clearly see a decreasing trend in the nanopore's baseline current, which is likely caused by nanoparticles translocating into the pore and adhering onto the pore walls resulting in a continuous increase in the ionic resistance.

To make a fair comparison between our newly developed GMB pore and the pipette pore, we used the same chemical condition (i.e., 100 mM HCl inside the pore, and 10 mM NaBr in the bulk) to study the translocation of 80 nm Ag nanoparticles and their transient bipolar electrochemistry response. With an inner volume significantly greater than that of a pipette pore, our GMB nanopore can greatly reduce the issue of pore clogging allowing one to record hundreds or even thousands of nanoparticles in a single run. As shown in **Figure 3.3B**, in the absence of Ag nanoparticles, a stable baseline current of -88 nA was recorded. When 80 nm Ag nanoparticles were present in the bulk solution at 3.8×10^7 particles/ml, hundreds of particle translocation events were detected in the amperometry trace at both -1.5 V and -2.0 V applied potentials (**Figure 3.3C**). Although the maximum duration of recording used in this study was 30 min (**Figure 3.9**), we believe the GMB pores can yield stable NP recordings without significant clogging for at least two hours.

Interestingly, all of the particle translocation events take place at negative potentials, which is opposite to our previous work using glass nanopipettes. In the absence of a pressure-driven flow, one can expect to have two major driving forces for the particles to enter the nanopore (pipette or GMB), the *electroosmotic force* and the *electrophoretic force*.[52] In the case of a nanopipette, the primary driving force for particle translocation is likely the electroosmotic force originated from the positive charges on the inner glass walls in 0.1 M acid (pH ~1),[53] as shown in **Figure 3.4** (left panel)**.** For a short glass nanopore, the primary driving force seems to be the electrophoretic force (**Figure 3.4**, right panel).

Similar to our previous observation, each translocation event is detected as an interesting biphasic current response with an initial upward current peak followed by a longer "waiting period" and a downward current peak at the end of the translocation event. Representative current spikes recorded at -1.5 and -2.0 V are given in **Figure 3.3C** as the inset. The shape of the biphasic current signal reflects the translocation dynamics of a Ag NP and *the unique bipolar electrochemical coupling response*.[37] Take the recording at -1.5 V as an example, the nanopore's ionic current initially experiences a slight increase (1.8 ± 0.9 %), which then decreases to the baseline. This upward peak is followed by a fairly long period (~300 ms) of somewhat stable current and an additional current decrease (3.8 ± 2.0 %). The ionic current then goes back to the baseline after the short, <10 ms downward peak. The average peak to peak duration is 324 ± 199 ms.

The shape of the resistive current pulse can be qualitatively understood from an examination of the possible redox processes. Without considering the possible electrochemical reactions on the particle, a translocating Ag nanoparticle may cause an observable change to the nanopore's ionic current, which may be a decrease in the ionic current due to the nanoparticle blocking the ionic pathway or an enhancement to the ionic current if the particle surface is charged and can cause an enhancement to the local ionic conductivity.[54] The true observable ionic signal will likely reflect a combination of these two opposite effects.[54] When a greater voltage is applied across the nanopore, the nanoparticle may start behaving like a bipolar nanoelectrode coupling two separate redox reactions across its two opposite ends. On the anodic side, the two possible reactions are the oxidation of Ag metal itself ($Ag + Br^- = AgBr + 1e^-$, $E^0 = 0.0711$ V vs NHE; or $Ag = Ag^+ + 1e^-$, $E^0 = 0.799$ V vs NHE) or the H_2O molecules[55] ($2H_2O = 4H^+ + O_2 + 4e^-$, $E^0 =$ 1.23 V vs NHE). On the cathodic side, there are also two possible reactions, the reduction of protons ($2H^+ + 2e^- = H_2$, $E^0 = 0$ V vs NHE) and the reduction of H_2O ($2H_2O + 2e^- = H_2 + 2OH^-$, $E^0 = -0.828$ V vs NHE).

Figure 3.5 is a cartoon which depicts our understanding of the translocation signal. The initial upward peak is likely due to the extra ionic charges the Ag nanoparticle brings to the vicinity of the pore and the possible coupled redox reactions across the nanoparticle surface releasing ions in the nearby solution, which enhances the local ionic conductivity of the pore.[37] The citrate ligands on the Ag nanoparticle have pKa values of 3.14, 4.76, 6.40.[56] This means that while Ag nanoparticles are initially negatively charged at neutral pH (e.g., in bulk NaBr solution), they may become neutral or even positively charged at lower pH (e.g., in 0.1 M HCl). The initial current increase (*a*-*b* on **Figure 3.5**) therefore may reflect the change in its surface charge from neutral to positive. As the particle enters the pore and continues to move inwards, the blocking effect becomes more and more significant and eventually outweighs the enhancement. This corresponds to the downward trend following the upward peak (*b*-*c* on **Figure 3.5**). As the NP moves further into the pore, it experiences an increasing local electric field, which triggers the oxidation of the Ag metal and H_2O, and the reduction of H^+ and H_2O. Two of these reactions generate gaseous molecules, which eventually nucleate into small nanobubbles causing a more dramatic decrease in the ionic current (*c*-*d* on **Figure 3.5**). As the NP moves out of the nanopore, the local electric field decreases leading to a smaller driving force for the coupled redox reactions. This in turn reduces the rate of formation for the gas molecules (H_2 and O_2) leading to the disappearance of the bubble. The ionic current increases back to the baseline when the particle goes completely out of the pore into the inner volume (*d*-*e* on **Figure 3.5**).

The detection frequencies (average number of current spikes detected per second) were 0.27 events/s and 1.0 events/s at -1.5 V and -2.0 V, respectively, in **Figure 3.3C**. As shown in **Figure 3.6**, the detection frequency increases linearly with particle concentration (7.6×10^7, 3.8×10^8 and 7.6×10^8 particles/mL), which further suggests that these current spikes were indeed caused by particle translocation events.

3.3.3 Voltage Dependence

Our further studies show that both the frequency of particle translocation and the shape of the resistive peak depend strongly on the magnitude of the applied voltage bias across the nanopore. **Figure 3.7** shows a series of *i-V* recordings of 80 nm Ag nanoparticles translocating through a 120-nm-diameter GMB nanopore at three different voltages, -3.0, -4.0, and -5.0 V. The same solution condition was used: bulk solution of 10 mM NaBr containing 80 nm Ag nanoparticles at 3.8×10^7 particles/ml and 0.1 M HCl inside the GMB pore. A clear increasing trend can be seen between the frequency of particle translocation and the applied voltage bias; The average detection frequency was 2.1 particles/s at -3.0 V, 6.3 particles/s at -4.0 V, and 8.9 particles/s at -5.0 V (**Figure 3.7D**).**Table 3.2** gives a summary of the characteristics of the translocation signal collected at five different voltages comparing their current increase, current blockage, peak-to-peak duration, and the detection frequency.

The fact that particles are driven into the GMB pore faster at more negative voltages further suggests that electrophoresis is the key driving force for particle translocation. While the biphasic peaks at -2.0 V are similar in shape to those at -1.5 V, their average peak to peak duration (178 ± 104 ms) is 45% shorter than that at -1.5 V (324 ± 199 ms) (shown in **Figure 3.1C** by the vertical dashed lines). The short event duration is in agreement with our hypothesis that the particles are driven primarily by the applied voltage across the nanopore.

By further increasing the negative voltage, we saw some interesting changes to the shape of the translocation signal. While both the upward and downward peaks are well defined in the translocation events at lower negative voltages, the upwards peak becomes much smaller and narrower at higher negative voltages and the translocation signal becomes more dominated by the downward peak (**Figure 3.7**). Moreover, the downward peak becomes significantly wider than the upward current spike. The current blockage increases from 8.8 ± 3.9 % at -3 V to 17.3 ± 3.3 % at -4 V and 20.0 ± 2.3 % at -5 V, respectively (**Figure 3.11**).

The transition of the upward peak into a short spike suggests the higher potential is more effective in pulling the particle into the pore mouth reducing the amount of time it spends from *a* through *c* (**Figure 3.5**).[57] Meanwhile, the current is seen to decay quickly reaching the lowest point within 1 ms suggesting the higher potential is also more effective in triggering the bipolar redox reactions leading to a faster nucleation of the gas nanobubble.[58] The increase in the percent blockage from 3.8% at -1.5 V to 20% at -5.0 V suggests the size of the nanobubble grows with increasing voltage bias across the nanopore. This is understandable as higher rates of coupled redox reactions can be expected at higher potentials.

An interesting observation has been made to the shape of the blockage signal in **Figure 3.7**. The current signal becomes very "noisy" at these higher potentials with large current fluctuations at high frequencies observed starting from the peak of the blockage signal until it returns to the baseline current. This oscillating current response is in good agreement with our hypothesis that nanobubbles are formed during the translocation process: A large bubble (primarily of H_2 from the reduction of H^+) is formed causing the ionic current to reach the lowest point; the formation of the nanobubble inevitably blocks the transport of protons from inside the pore to the outside; this reduces the rate of proton reduction causing the bubble to shrink in size, which causes the ionic current to increase and allows more H^+ to reach the outside; the availability of more H^+ ions allows the coupled redox reactions to resume generating more H_2 gas molecules and resuming the size of the nanobubble; the greater bubble size also leads to a large current blockage. This process has been illustrated in **Figure 3.8**.

3.4 Conclusions

In summary, we have developed a method for fabricating individual glass nanopores in a glass microbulb with an ultrathin glass membrane. As an interesting application of the GMB nanopore, we studied the bipolar electrochemistry response of single Ag nanoparticles when they pass through the nanopore. Compared with a long and skinny nanopipette, a GMB nanopore has a shorter pore length and a greater internal volume allowing us to continuously record hundreds or even thousands of particle translocation events without pore clogging.

With our current experimental setting (0.1 M HCl inside the nanopore and 0.01 M NaBr in the bulk), the bipolar electrochemistry response of a translocating Ag nanoparticle is characterized by a biphasic current signal on an amperometric recording. It starts with a small but noticeable upward current spike followed by a more significant downward current peak before returning to the baseline. Using our GMB nanopore, we were able to obtain more detailed information about the amperometric signal at relatively higher voltages and better understand the translocation process and its associated bipolar nanoparticle electrochemistry at single Ag nanoparticles. Our results suggest nanobubbles can repeatedly form and dissolve on a moving nanoparticle as it translocates through a short glass nanopore. Such behavior is reflected as fast current oscillations that last tens of milliseconds during single translocation events. A higher applied voltage bias promotes such oscillating response suggesting fast bipolar coupled electrochemical kinetics and fast nucleation dynamics of nanobubbles.

A more detailed understanding of the bipolar electrochemistry behavior of single metal nanoparticles will likely benefit our future research in designing ultrasensitive biosensors using the principles of single-entity electrochemistry and metal nanoparticles as a unique biolabeling agent.

3.5 Figures and Table

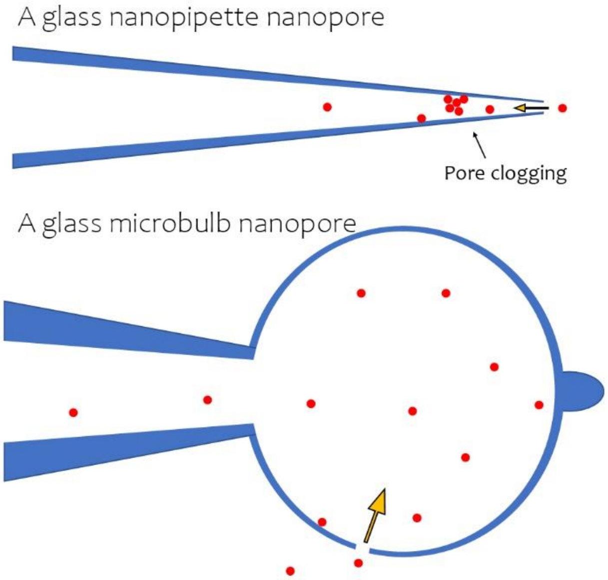

Figure 3.1. Schematic of a glass nanopipette and a glass microbulb (GMB) nanopore.
A schematic drawing of a glass nanopipette (upper panel) and a glass microbulb (GMB) nanopore (lower panel). The nanopipette has an ultralong and thin neck making it easily clogged by nanoparticles adsorbing on the pipette walls. A glass microbulb pore has a large inner volume and an ultrathin glass membrane to circumvent the clogging issue.

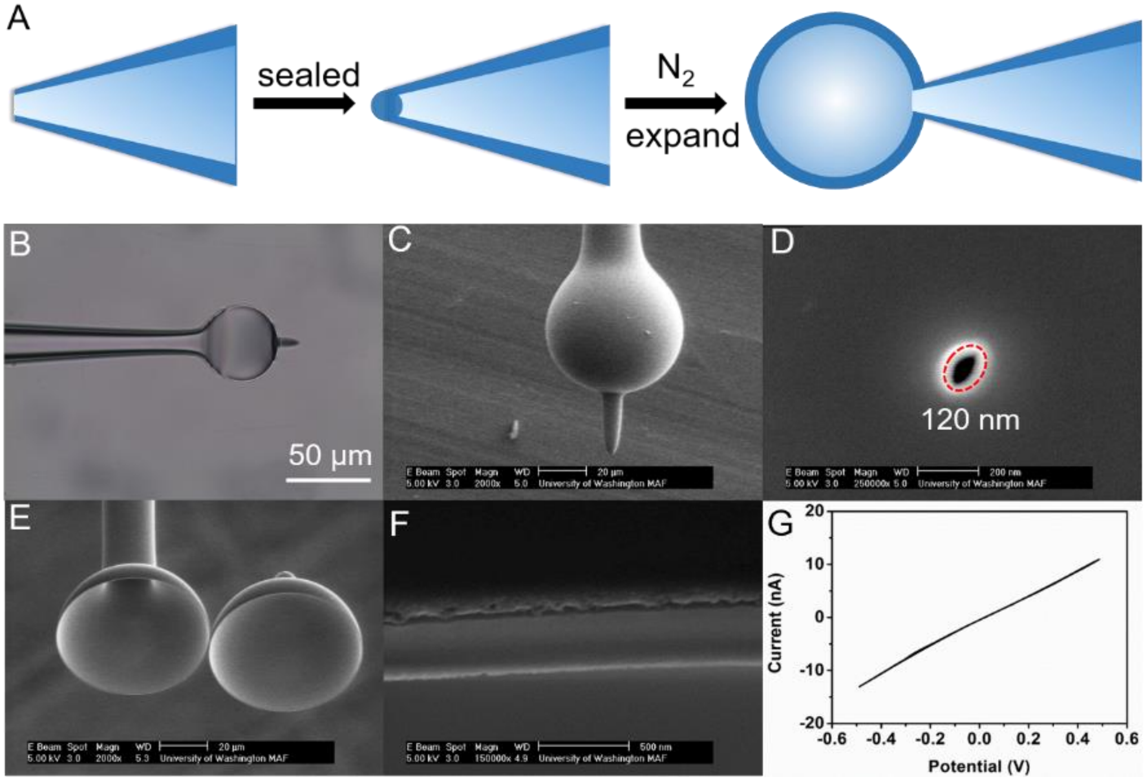

Figure 3.2. Fabrication and characterization of GMB.
(A) Schematic depicts the fabrication of GMB. A bright field optical image (B) and an SEM image (C) of a GMB. (D) An SEM of a 120 nm diameter pore milled in a GMB. (E) An SEM image of a GMB milled in half along the equator. (F) An SEM image showing the cross-section of the GMB membrane with a thin carbon layer. (G) A representative *i*-*V* curve of a 120 nm diameter glass nanopore in 100 mM KCl. The scan rate was 100 mV/s.

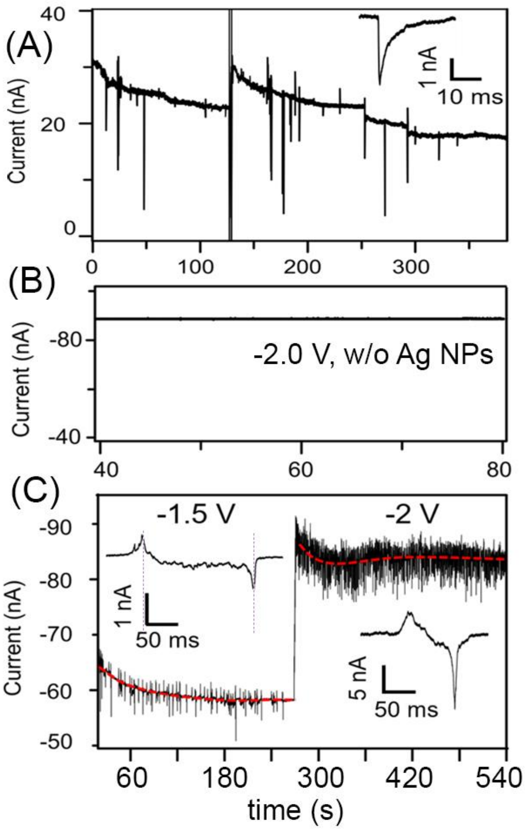

Figure 3.3. Example of current-time traces of the translocation events.
(A) A 380-second i-t trace of a 150-nm-diameter quartz nanopipette containing 0.1 M HCl immersed in a bulk solution containing 10 mM NaBr and 80 nm Ag nanoparticles at 3.8×10^7 NPs/ml. (B) A 40-second i-t trace of an FIB-milled 120 nm GMB nanopore recorded at -2.0 V in the absence of Ag NPs. The solution inside the GMB was 0.1 M HCl while the outside solution contained 10 mM NaBr. (C) A 540-second i-t trace showing translocation events of Ag nanoparticles recorded at -1.5 and -2.0 V after adding 80 nm Ag nanoparticles in the bulk solution to a final concentration of 3.8×10^7 particles/ml. Insets are zoom-in views of representative current spikes with two vertical dashed lines showing the upward and downward peaks.

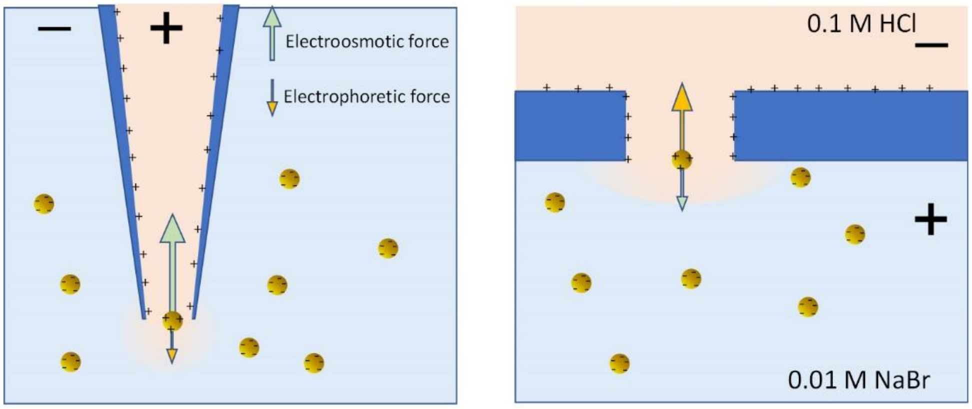

Figure 3.4. Driving forces for particle translocation.
A cartoon showing the different driving forces for particle translocation with a glass nanopipette pore (left) and a GMB pore (right). For a nanopipette, the electroosmotic force dominate the electrophoretic force; Whereas for a shorter glass nanopore, the electrophoretic force outweighs the electroosmotic force.

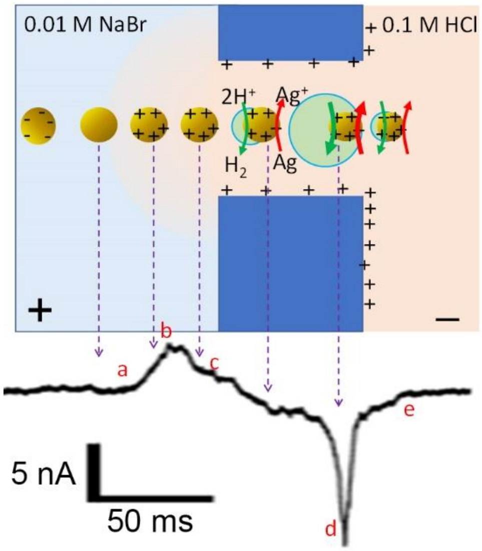

Figure 3.5. Proposed mechanism of biphasic signal.
A cartoon showing our proposed mechanism to the observed biphasic current signal of a Ag nanoparticle translocating through a glass nanopore. Only one of the possible redox reactions is shown on each of the two opposite poles.

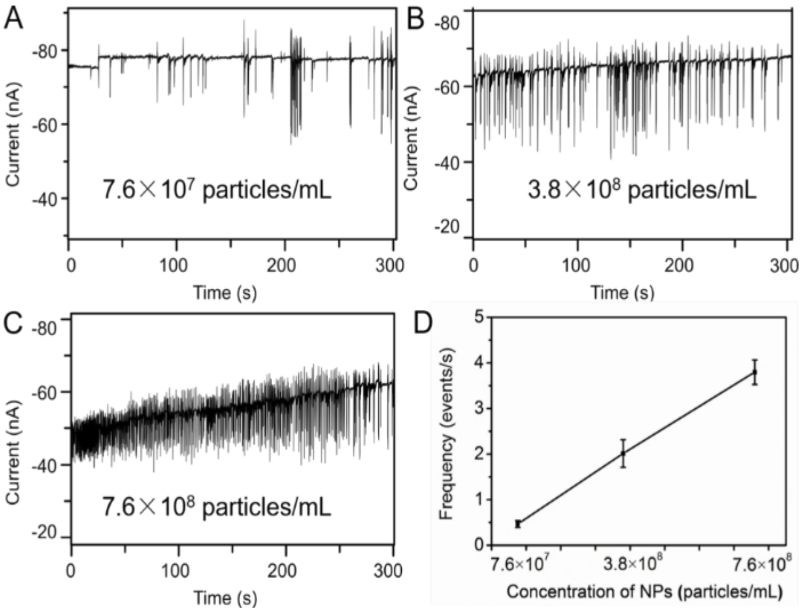

Figure 3.6. Concentration-dependent translocation.

Amperometric recordings for a 120 nm GMB nanopore at -3.0 V in a 10 mM NaBr solution containing 80 nm Ag nanoparticles at three different concentrations (A) 7.6 × 10^7, (B) 3.8 × 10^8, and (C) 7.6 × 10^8 NPs/ml. (D) Frequency of particle detection (events/s) plotted verses particle concentration.

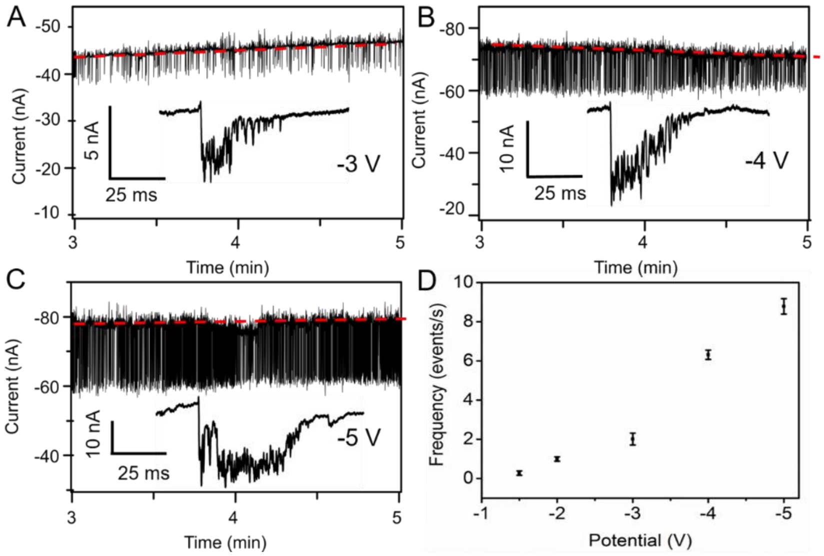

Figure 3.7. Voltage-dependent translocation.

Amperometric recordings for a 120-nm-diameter GMB nanopore in a 10 mM NaBr solution containing 80 nm Ag nanoparticles at 3.8 × 10^7 particles/ml at three different potentials, -3.0 (A), -4.0 (B), and -5.0 V (C). (D) Detection frequency (events/s) as a function of applied voltage.

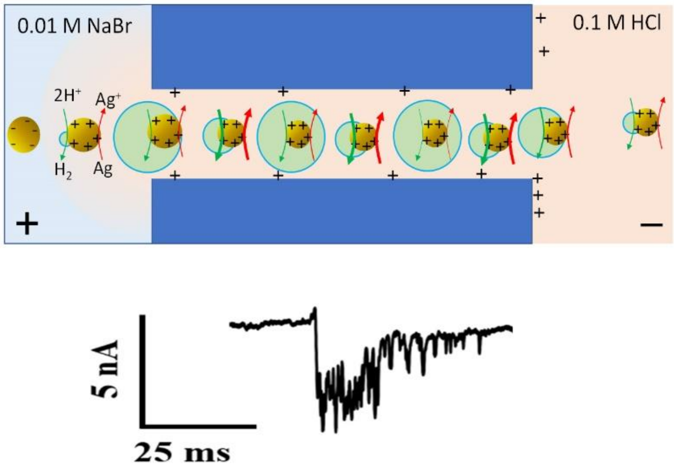

Figure 3.8. Proposed mechanism for current oscillation.

A cartoon showing the proposed mechanism for the current oscillation in the current signal. The repeated formation and dissolution of a single nanobubble likely causes the nanopore's ionic resistance to fluctuate causing the ionic current to oscillate. A typical translocation current signal is given at the bottom to show the fast current fluctuation.

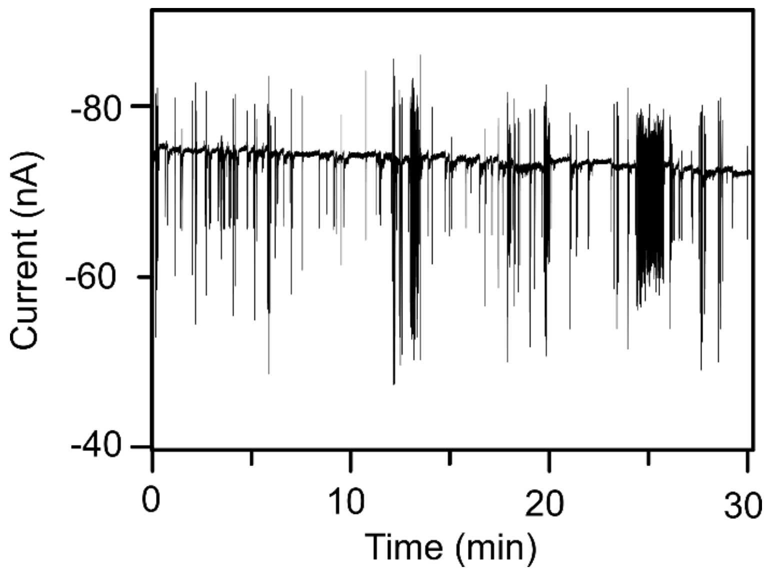

Figure 3.9. Clog-free detection of GMB.

Representative current-time traces showing individual Ag nanoparticles translocation events recorded at -2 V in 30 min. The solution inside the GMB nanopore was 0.1 M HCl while the outside solution contains 10 mM NaBr and 3.8×10^7 particles/mL 80 nm Ag nanoparticles.

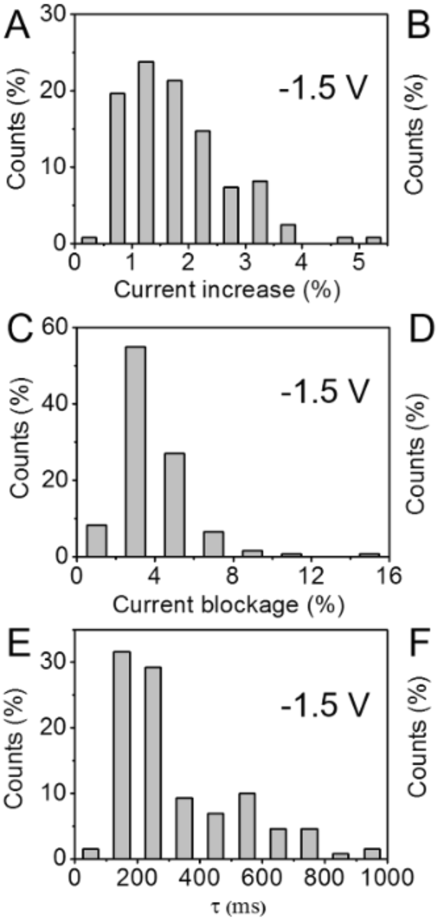

Figure 3.10. Statistics of current increase (%), current blockage (%) and peak-peak duration at -1.5 V and -2 V.

Histograms of the current increase (%) of the current spikes at -1.5 V (A) and -2.0 V (B). Histograms of the current blockage (%) at -1.5 V (C) and -2.0 V (D). Histograms of the peak-peak duration (ms) of the current spikes at -1.5 V (E) and -2.0 V (F). The counts were divided by the total number of counts to obtain the counts (%). The solution inside the GMB nanopore was 0.1 M HCl while the outside solution contained 10 mM NaBr and 80 nm Ag nanoparticles at 3.8×10^7 particles/mL.

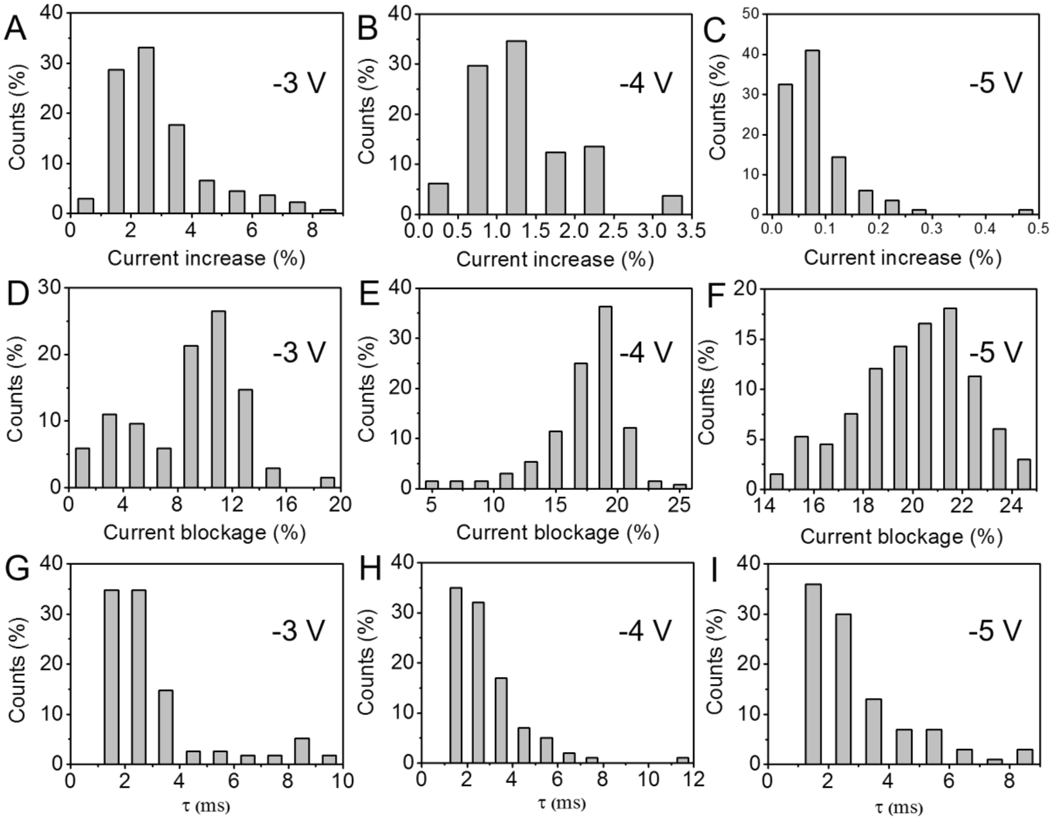

Figure 3.11. Statistics of current increase (%), current blockage (%) and peak-peak duration at -3 V, -4 V, and -5 V.

Histograms of the current increase (%) of the current spikes at -3 V (A), -4 V (B) and -5 V (C). Histograms of the current blockage (%) of the current spikes at -3 V (D), -4 V (E) and -5 V (F). Histograms of the peak-to-peak duration (ms) of the current spikes at -3 V (G), -4 V (H) and -5 V (I). The counts were divided by the total number of counts to obtain the counts (%). The solution inside the GMB nanopore was 0.1 M HCl while the outside solution contains 10 mM NaBr and 3.8 × 10^7 particles/ml 80 nm Ag nanoparticles.

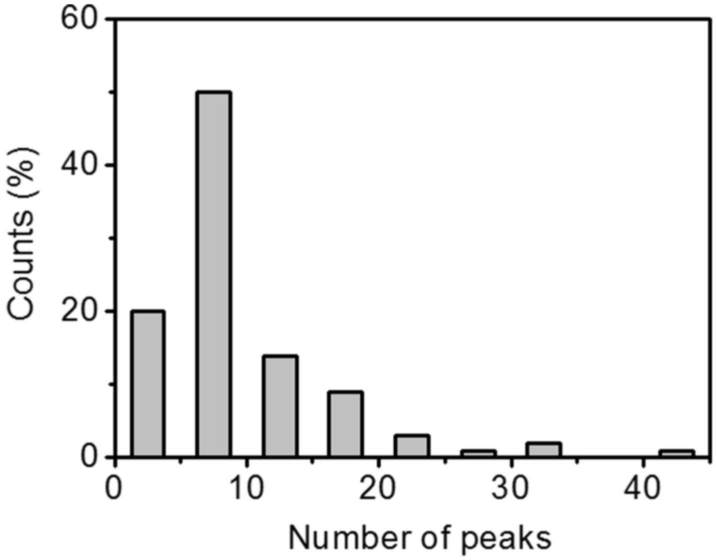

Figure 3.12. Statistics of oscillating spikes within one biphasic signal.
Histograms of the number of oscillating spikes within one biphasic signal of individual Ag nanoparticles translocation events recorded at -3 V. The solution inside the GMB nanopore was 0.1 M HCl while the outside solution contains 10 mM NaBr and 3.8×10^7 particles/mL 80 nm Ag nanoparticles.

Table 3.2. Characteristics for Translocation Signals of Ag nanoparticles at Different Voltages.

Voltage (V)	Current increase (%)	Current blockage (%)	Peak to peak duration (ms)	Frequency (events/s)
-1.5	1.8 ± 0.9	3.8 ± 2.0	324 ± 199	0.28 ± 0.10
-2.0	2.3 ± 0.6	4.3 ± 1.4	178 ± 104	0.99 ± 0.11
-3.0	2.9 ± 1.5	8.8 ± 3.9	2.5 ± 2.0	2.01 ± 0.30
-4.0	1.3 ± 0.7	17.3 ± 3.3	2.3 ± 1.6	6.32 ± 0.24
-5.0	0.09 ± 0.07	20.0 ± 2.3	2.5 ± 1.7	8.79 ± 0.39

3.6 References

(1) Kwon, S. J.; Zhou, H.; Fan, F.-R. F.; Vorobyev, V.; Zhang, B.; Bard, A. J. Stochastic electrochemistry with electrocatalytic nanoparticles at inert ultramicroelectrodes—theory and experiments. *Phys. Chem. Chem. Phys.* **2011**, *13*, 5394–5402.

(2) Anderson, T. J.; Zhang, B. Single-Nanoparticle Electrochemistry through Immobilization and Collision. *Acc. Chem. Res.* **2016**, *49*, 2625–2631.

(3) Clarke, T. B.; Krushinski, L. E.; Vannoy, K. J.; Colon-Quintana, G.; Roy, K.; Rana, A.; Renault, C.; Hill, M. L.; Dick, J. E. Single Entity Electrocatalysis. *Chem. Rev.* **2024**, *124*, 9015–9080.

(4) Yang, Y. J.; Bai, Y. Y.; Huangfu, Y. Y.; Yang, X. Y.; Tian, Y. S.; Zhang, Z. L. Single-Nanoparticle Collision Electrochemistry Biosensor Based on an Electrocatalytic Strategy for Highly Sensitive and Specific Detection of H7N9 Avian Influenza Virus. *Anal. Chem.* **2022**, *94*, 8392–8398.

(5) Kwon, S. J.; Bard, A. J. DNA Analysis by Application of Pt Nanoparticle Electrochemical Amplification with Single Label Response. *J. Am. Chem. Soc.* **2012**, *134*, 10777–10779.

(6) Castañeda, A. D.; Brenes, N. J.; Kondajji, A.; Crooks, R. M. Detection of microRNA by Electrocatalytic Amplification: A General Approach for Single-Particle Biosensing. *J. Am. Chem. Soc.* **2017**, *139*, 7657–7664

(7) Zhang, J.-H.; Shen, Q.; Zhou, Y.-G. Quantification of Tumor Protein Biomarkers from Lung Patient Serum Using Nanoimpact Electrochemistry. *ACS Sens.* **2021**, *6*, 2320–2329.

(8) Karimi, A.; Hayat, A.; Andreescu, S. Biomolecular detection at ssDNA-conjugated nanoparticles by nano-impact electrochemistry. *Biosens. Bioelectron.* **2017**, *87*, 501–507.

(9) Quast, T.; Varhade, S.; Saddeler, S.; Chen, Y.-T.; Andronescu, C.; Schulz, S.; Schuhmann, W. Single Particle Nanoelectrochemistry Reveals the Catalytic Oxygen Evolution Reaction Activity of Co_3O_4 Nanocubes. *Angew. Chem. Int. Ed.* **2021**, *60*, 23444–23450.

(10) Chen, S.; Kucernak, A. Electrocatalysis under Conditions of High Mass Transport Rate: Oxygen Reduction on Single Submicrometer-Sized Pt Particles Supported on Carbon. *J. Phys. Chem. B* **2004**, *108*, 3262–3276.

(11) Li, Y.; Cox, J. T.; Zhang, B. Electrochemical Responses and Electrocatalysis at Single Au Nanoparticles *J. Am. Chem. Soc.* **2010**, *132*, 3047–3054.

(12) Hill, C. M.; Kim, J.; Bard, A. J. Electrochemistry at a Metal Nanoparticle on a Tunneling Film: A Steady-State Model of Current Densities at a Tunneling Ultramicroelectrode. *J. Am. Chem. Soc.* **2015**, *137*, 11321–11326.

(13) Wahab, O. J.; Kang, M.; Unwin, P. R. Scanning electrochemical cell microscopy: A natural technique for single entity electrochemistry. *Curr. Opin. Electrochem.* **2020**, *22*, 120–128.

(14) Lai, S. C. S.; Dudin, P. V.; Macpherson, J. V.; Unwin, P. R. Visualizing Zeptomole (Electro)Catalysis at Single Nanoparticles within an Ensemble. *J. Am. Chem. Soc.* **2011**, *133*, 10744–10747.

(15) Oja, S. M.; Robinson, D. A.; Vitti, N. J.; Edwards, M. A.; Liu, Y.; White, H. S.; Zhang, B. Observation of Multipeak Collision Behavior during the Electro-Oxidation of Single Ag Nanoparticles. *J. Am. Chem. Soc.* **2017**, *139*, 708–718.

(16) Hao, R.; Fan, Y.; Zhang, B. Imaging Dynamic Collision and Oxidation of Single Silver Nanoparticles at the Electrode/Solution Interface. *J. Am. Chem. Soc.* **2017**, *139*, 12274–12282.

(17) Robinson, D. A.; Liu, Y.; Edwards, M. A.; Vitti, N. J.; Oja, S. M.; Zhang, B.; White, H. S. Collision Dynamics during the Electrooxidation of Individual Silver Nanoparticles. *J. Am. Chem. Soc.* **2017**, *139*, 16923–16931.

(18) Ustarroz, J.; Kang, M.; Bullions, E.; Unwin, P. R. Impact and Oxidation of Single Silver Nanoparticles at Electrode Surfaces: One Shot Versus Multiple Events. *Chem. Sci.* **2017**, *8*, 1841–1853.

(19) Ma, W.; Ma, H.; Chen, J.-F.; Peng, Y.-Y.; Yang, Z.-Y.; Wang, H.-F.; Ying, Y.-L.; Tian, H.; Long, Y.-T. Tracking Motion Trajectories of Individual Nanoparticles Using Time-Resolved Current Traces. *Chem. Sci.* **2017**, *8*, 1854–1861.

(20) Ma, H.; Chen, J. F.; Wang, H. F.; Hu, P. J.; Ma, W.; Long, Y. T. Exploring Dynamic Interactions of Single Nanoparticles at Interfaces for Surface-Confined Electrochemical Behavior and Size Measurement. *Nat. Commun.* **2020**, *11*, 2307.

(21) Lewis, T. H.; Zhang, B. Nanoparticle Adhesion and the Role of Nanobubbles in Single-Particle Collision Electrochemistry. *J. Phys. Chem. C* **2024**, *128*, 13074–13082.

(22) Wan, R.; Mahmoudi, M.; Edwards, M. A.; Zhang, B. The Critical Role of Molecular Adsorption on Electrocatalysis at Single Nanoparticles. *Anal. Chem.* **2025**, *97*, 3955-3963.

(23) Quinn, B. M.; van't Hof, P. G.; Lemay, S. G. Time-Resolved Electrochemical Detection of Discrete Adsorption Events. *J. Am. Chem. Soc.* **2004**, *126*, 8360–8361.

(24) Xiao, X.; Fan, F.-R. F.; Zhou, J.; Bard, A. J. Current Transients in Single Nanoparticle Collision Events *J. Am. Chem. Soc.* **2008**, *130*, 16669–16677

(25) Cheng, W.; Compton, R. G. Electrochemical detection of nanoparticles by 'nano-impact' methods. *TrAC Trends Anal. Chem.* **2014**, *58*, 79– 89.

(26) Defnet, P. A.; Han, C.; Zhang, B. Temporally-Resolved Ultrafast Hydrogen Adsorption and Evolution on Single Platinum Nanoparticles. *Anal. Chem.* **2019**, *91*, 4023–4030.

(27) Park, J. H.; Thorgaard, S. N.; Zhang, B.; Bard, A. J. Single particle detection by area amplification: single wall carbon nanotube attachment to a nanoelectrode. *J. Am. Chem. Soc.* **2013**, *135*, 5258– 5261.

(28) Park, J. H.; Zhou, H.; Percival, S. J.; Zhang, B.; Fan, F.-R. F.; Bard, A. J. Open Circuit (Mixed) Potential Changes Upon Contact Between Different Inert Electrodes-Size and Kinetic Effects. *Anal. Chem.* **2013**, *85*, 964–970.

(29) Defnet, P. A.; Anderson, T. J.; Zhang, B. Stochastic collision electrochemistry of single silver nanoparticles. *Curr. Opin. Electrochem.* **2020**, *22*, 129–135.

(30) Dasari, R.; Robinson, D. A.; Stevenson, K. J. Ultrasensitive Electroanalytical Tool for Detecting, Sizing, and Evaluating the Catalytic Activity of Platinum Nanoparticles *J. Am. Chem. Soc.* **2013**, *135*, 570-573

(31) Jung, A. R.; Lee, S.; Joo, J. W.; Shin, C.; Bae, H.; Moon, S. G.; Kwon, S. J. Potential-Controlled Current Responses from Staircase to Blip in Single Pt Nanoparticle Collisions on a Ni Ultramicroelectrode. *J. Am. Chem. Soc.* **2015**, *137*, 1762–1765.

(32) Defnet, P. A.; Zhang, B. C. Collision, Adhesion, and Oxidation of Single Ag Nanoparticles on a Polysulfide-Modified Microelectrode. *J. Am. Chem. Soc.* **2021**, *143*, 16154–16162.

(33) Gao, R.; Edwards, M. A.; Harris, J. M.; White, H. S. Shot noise sets the limit of quantification in electrochemical measurements. *Curr. Opin. Electrochem.* **2020**, *22*, 170–177.

(34) Mirkin, M. V.; Sun, T.; Yu, Y.; Zhou, M. Electrochemistry at One Nanoparticle. *Acc. Chem. Res.* **2016**, *49*, 2328–2335.

(35) Percival, S. J.; Zhang, B. Fast-Scan Cyclic Voltammetry Allows Determination of Electron-Transfer Kinetic Constants in Single Nanoparticle Collision. *J. Phys. Chem. C* **2016**, *120*, 20536–20546.

(36) Guo, Z.; Percival, S. J.; Zhang, B. Chemically Resolved Transient Collision Events of Single Electrocatalytic Nanoparticles. *J. Am. Chem. Soc.* **2014**, *136*, 8879–8882.

(37) Han, C.; Hao, R.; Fan, Y.; Edwards, M. A.; Gao, H.; Zhang, B. Observing Transient Bipolar Electrochemical Coupling on Single Nanoparticles Translocating through a Nanopore. *Langmuir* **2019**, *35*, 7180-7190

(38) Morris, C. A.; Friedman, A. K.; Baker, L. A. Applications of Nanopipettes in the Analytical Sciences. *Analyst* **2010**, *135*, 2190–2202.

(39) Castañeda, A. D.; Robinson, D. A.; Stevenson, K. J.; Crooks, R. M. Electrocatalytic Amplification of DNA-modified Nanoparticle Collisions via Enzymatic Digestion. *Chem. Sci.* **2016**, *7*, 6450–6457.

(40) Park, J.-W.; Shumaker-Parry, J. S. Structural Study of Citrate Layers on Gold Nanoparticles: Role of Intermolecular Interactions in Stabilizing Nanoparticles. *J. Am. Chem. Soc.* **2014**, *136*, 1907–1921.

(41) Luo, L.; German, S. R.; Lan, W.-J.; Holden, D. A.; Mega, T. L.; White, H. S. Resistive-pulse analysis of nanoparticles. *Annul. Rev. Anal. Chem.* **2014**, *7*, 513–535.

(42) Shi, W.; Friedman, A. K.; Baker, L. A. Nanopore sensing. *Anal. Chem.* **2017**, *89*, 157–188.

(43) Yang, R.; Kvetny, M.; Brown, W.; Ogbonna, E. N.; Wang, G. A Single-Entity Method for Actively Controlled Nucleation and High-Quality Protein Crystal Synthesis. *Anal. Chem.* **2023**, *95*, 9462–9470.

(44) Gunderson, C. G.; Barlow, S. T.; Zhang, B. FIB-Milled Quartz Nanopores in a Sealed Nanopipette. *J. Electro. Chem.* **2019**, *833*, 181–188.

(45) Lima, M. M.; Monteira, R. Characterization and thermal behavior of a borosilicate glass. *Themocheima Acta* **2001**, *373*, 69-74.

(46) Ito T, Sun L, Crooks R M. Simultaneous Determination of the Size and Surface Charge of Individual Nanoparticles Using a Carbon Nanotube-Based Coulter Counter. *Anal. Chem.* **2003**, *75*, 2399-2406.

(47) Li, G.; Wen, L.; Sun, R.; Hao, R. Imaging electrochemically regulated water–air nanointerfaces with single-molecule fluorescence. *Chem. Sci.* **2025**, *Advanced Article*.

(48) Gunderson, C. G.; Barlow, S. T.; Zhang, B. FIB-milled quartz nanopores in a sealed nanopipette. *J. ElectroAnal. Chem.* **2019**, *833*, 181–188.

(49) Perry, D.; Momotenko, D.; Lazenby, R. A.; Kang, M.; Unwin, P. R. Characterization of Nanopipettes. *Anal. Chem.* **2016**, *88*, 5523–5530.

(50) Wei, C.; Bard, A. J.; Feldberg, S. W. Current Rectification at Quartz Nanopipet Electrodes. *Anal. Chem.* **1997**, *69*, 4627– 4633.

(51) Guerrette, J. P.; Zhang, B. Scan-rate-dependent current rectification of cone-shaped silica nanopores in quartz nanopipettes. *J. Am. Chem. Soc.* **2010**, *132*, 17088–17091.

(52) German, S. R.; Luo, L.; White, H. S.; Mega, T. L. Controlling nanoparticle dynamics in conical nanopores. *J. Phys. Chem. C* **2013**, *117*, 703–711.

(53) Szalóki, M.; Hegedűs, V.; Fodor, T.; Martos, R.; Radics, T.; Hegedűs, C.; Dezső, B. Evaluation of the Effect of the Microscopic Glass Surface Protonation on the Hard Tissue Thin Section Preparation. *Appl. Sci.* **2020**, *10*, 7742.

(54) Lan, W. J.; Kubeil, C.; Xiong, J. W.; Bund, A.; White, H. S. Effect of Surface Charge on the Resistive Pulse Waveshape during Particle Translocation through Glass Nanopores. *J. Phys. Chem. C* **2014**, *118*, 2726–2734.

(55) Zhang, F.; Defnet, P. A.; Fan, Y.; Hao, R.; Zhang, B. Transient Electrocatalytic Water Oxidation in Single-Nanoparticle Collision. *J. Phys. Chem. C* **2018**, 6447-6455.

(56) The Merck Index, 12th ed., Entries# 2387 and 8746.

(57) Liu, Y.; Xu, C.; Gao, T.; Chen, X.; Wang, J.; Yu, P.; Mao, L. Sizing Single Particles at the Orifice of a Nanopipette. *ACS Sens.* **2020**, *5*, 2351– 2358,

(58) Soto, Á. M.; German, S. R.; Ren, H.; Van Der Meer, D.; Lohse, D.; Edwards, M. A.; White, H. S. The Nucleation Rate of Single O2 Nanobubbles at Pt nanoelectrode. *Langmuir* **2018**, *34*, 7309–7318.

CHAPTER 4 EXPLORATION OF TRANSIENT METAL NANOPARTICLE TRANSLOCATION IMAGING USING ELECTROCHEMILUMINESCENCE

4.1 Introduction

Since its introduction in 2016, single-entity electrochemistry (SEE) has emerged as a powerful tool in electrochemistry due to its ability to resolve individual analytes (e.g. cells, nanoparticles, and molecules) from ensemble measurements.[1, 2] This capability is particularly valuable for detecting biological entities, where heterogeneity and ultralow concentrations pose significant challenges, as in early disease diagnosis.[3] As discussed in Chapters 2 and 3, among SEE methodologies, nanopore-based sensing offers a key advantage over nanoparticle collision electrochemistry by facilitating the wireless coupling of redox reactions on a single nanoparticle, thereby broadening its applicability in bioanalytical systems.

Despite these advantages, conventional SEE platforms face inherent limitations when applied to ultralow-concentration analytes. Nanoscale electrodes or nanopores are typically employed to minimize background noise, yet their small dimensions result in low total analyte flux (as opposed to flux density), leading to impractically long detection times.[4] For instance, when the analyte concentration is 1 pM, a 100 nm sensor captures only ~0.01 molecules per second, indicating ~100 s duration between detections.[4] Furthermore, biosensing applications demand high receptor densities to compensate for slow binding kinetics at ultralow concentrations.[4] For example, detecting 1 pM DNA with 10% accuracy within 100 s requires approximately 2×10^8 receptors, indicating a sensor diameter of ~36 µm, which is far exceeding the nanoscale dimensions of typical SEE platforms.[4] To overcome these challenges, dense arrays of nanopores present an attractive solution. Such arrays combine the benefits of nanoscale sensitivity with enhanced mass transport and increased total receptor count, enabling statistically robust detection of rare analytes within practical time duration.[4] Additionally, nanopore arrays can facilitate spatial mapping of analytes, further expanding their utility in multiplexed and high-throughput biosensing. Thus, the development of scalable, high-density nanopore arrays represents a critical advancement for SEE, bridging the gap between single-molecule sensitivity and real-world analytical applications.

The signal detection of nanopore array is mainly based on electrochemical imaging as electrical measurement can be limited by flicker noise[5, 6] and throughput of readout channels[7]. In general, two groups of electrochemical imaging methods have been applied to nanopore-based SEE: scanning probe methods and optical imaging. In scanning probe methods, a nanoscale probe (e.g., a nanoelectrode or nanopipette) is raster-scanned across the nanopore array to spatially resolve electrochemical activity. For instance, scanning electrochemical microscopy (SECM) has enabled *in situ* visualization of radical diffusion dynamics across nanopore arrays with high spatial resolution.[8] However, the sequential nature of probe scanning inherently limits temporal resolution, restricting real-time monitoring of rapid processes. In optical imaging, the translocation of fluorescence-labeled analytes is monitored by total internal reflection fluorescence microscopy (TIRF)[9, 10], confocal fluorescence microscopy[11], or fluorescence microscopy[12]. While these methods provide parallelized detection, their application is constrained by the need for analyte labeling, specialized laser illumination, and photobleaching effects, which collectively hinder long-term measurements and broader applicability.

Electrochemiluminescence (ECL) based closed bipolar electrochemical imaging has been extensively explored on the ultramicroelectrode arrays[13, 14, 15, 16, 17], owing to its inherent advantages of photostability[18], elimination of external excitation sources, and potential for label-free detection in closed bipolar configurations. The system employs a closed bipolar electrode (BPE) that simultaneously couples a target redox reaction at one pole with an ECL-generating reaction at the opposite pole, effectively converting electrochemical events into spatially resolved optical signals.[19] The closed BPE configuration physically isolates the cathodic and anodic poles with an insulating barrier. Each pole is immersed in separate electrolyte solutions. Notably, the applied voltage is delivered through driving electrodes rather than the BPE itself, enabling the *wireless* operation of the bipolar electrode. This design facilitates the scalable fabrication of electrode arrays without the need for direct electrical connections to individual sensing elements. This technique has proven particularly valuable for single-entity detection, demonstrating remarkable sensitivity in monitoring transient nanoparticle collision events with single-particle resolution.[20] Building on this foundation, we draw inspiration from previous work (discussed in Chapter 3) where metal nanoparticles translocating nanopores function as transient bipolar electrodes, allowing wireless probing of single-nanoparticle electrochemistry. This principle motivates our proposed adaptation of closed bipolar ECL for nanopore array imaging, wherein ECL reactions are coupled with redox reactions of interest to enable parallelized, high-sensitivity detection (**Figure 4.1**).

In this chapter, we establish a fundamental framework for imaging transient nanoparticle translocation events across large-scale nanopore arrays by first investigating single-nanopipette-based bipolar electrochemiluminescence (ECL) detection. Our approach systematically progresses through three experimental stages: First, we developed and characterized a bipolar ECL imaging system using paired gold ultramicroelectrodes (UMEs), demonstrating successful coupling between ECL generation and oxygen/water reduction reactions. Second, to simulate nanoparticle translocation events, we deposited gold nanoclusters at the nanopipette orifice and examined their bipolar ECL response under both linear sweep and pulsed voltage conditions. Finally, we explored multiple experimental configurations to achieve bipolar ECL imaging of gold nanoparticle (Au NP) translocations. While these attempts did not yield observable translocation events, our results suggest the system's performance is fundamentally limited by three key factors: (1) nanoparticle residence time within the detection zone, (2) faradaic efficiency of the coupled reactions, and (3) optical detection sensitivity. These findings establish important design considerations for future development of ECL-based nanopore sensing platforms, highlighting the need for optimized nanopore geometries, enhanced ECL reporter systems, and improved temporal resolution to successfully capture transient nanoparticle translocation events.

4.2 Experimental Section

4.2.1 Reagents and Solutions

All chemical reagents were used as received. The following chemicals were used as received from their manufacturers: potassium chloride (KCl, Fluka, >99%), potassium ferricyanide ($K_3Fe(CN)_6$, Sigma-Aldrich), ferrocenemethanol (FcMeOH, Sigma-Aldrich, 97%), tris(2,2'-bipyridyl)dichlororuthenium(II) hexahydrate ($Ru(bpy)_3^{2+}$, Sigma-Aldrich, 99.5%), 2-(dibutylamino)ethanol (DBAE, Sigma-Aldrich, 99%), potassium phosphate monobasic (KH_2PO_4, J.T. Baker, 99.9%), potassium phosphate dibasic (K_2HPO_4, J.T. Baker, 99.9%), sodium borohydride ($NaBH_4$, Sigma-Aldrich, 98.0%), hydrogen peroxide (H2O2, Thermo Scientific, 30%), sodium citrate dihydrate ($HOC(COONa)(CH2COONa)_2 \cdot 2H_2O$, Sigma-Aldrich). Gold(III) chloride (HAuCl4) was purchased from Salt Lake Metals (1% solution by weight, 99.99% purity). All solutions were prepared with 18.2 MΩ·cm deionized water from a Barnstead NANOpure water purification system (Thermo Scientific).

4.2.2 Electrode Fabrication

The fabrication of 25 μm Au disk ultramicroelectrode (UME) was fabricated as previously reported in Chapter 2. Before each experiment, Au UMEs were freshly polished with fine 1200-grit sandpaper (Buehler) and rinsed with excess DI water. All the electrodes were characterized and screened by running cyclic voltammetry at 100 mV/s in an aqueous solution containing 1 mM FcMeOH and 100 mM KCl.

To prepare Ag/AgCl quasi-reference electrodes, a piece of 0.5-mm-diameter Ag wire (99.99%, Alfa Aesar) was submerged in bleach for at least one hour and subsequently rinsed with DI water.

4.2.3 Nanoparticle Synthesis

Gold nanoparticles were synthesized as previously described.[21] In general, citrate-stabilized Au nanoparticle (NP) seeds were synthesized via a modified Turkevich method involving the rapid injection of citrate (1.5 mL, 1 wt%)/$HAuCl_4$ (0.5 mL, 1 wt%)/$AgNO_3$ (42.5 μL, 0.1 wt%)/H_2O (457.5 μL) mixture into boiling water, followed by 1 h of reflux to yield uniform, quasi-spherical Au NPs. These seeds were subsequently used in the seeded growth synthesis of monodisperse Au NPs with 147 nm in diameter. Growth was achieved under ambient conditions by H_2O_2-mediated reduction of HAuCl4 in the presence of sodium citrate, with particle size tuned via the molar ratio of HAuCl4 to seed. For the synthesis of 142 nm Au NPs, the reaction mixture containing 4.9 mL H_2O, 0.29 mM HAuCl4, 85 μM citrate, and 5 M H_2O_2 was prepared under stirring, followed by the injection of 2.8 nM gold seeds solution. H_2O_2 was removed by centrifugation. The size of Au NPs was confirmed by dynamic light scattering (DLS) (**Figure 4.9**).

4.2.4 Fabrication and Characterization of Nanopipettes

For the fabrication of nanopipettes, borosilicate capillary tubing with filament (1.2 mm o.d., 0.69 mm i.d.) (Sutter Instrument) was pulled. For the gold nanocluster deposited nanopipette, a flaming/brown puller (SU-97, Sutter Instrument) was used. Nanopipettes were pulled using program below: HEAT = RAMP, PUL = 45, VEL = 80, DEL = 200, PRESSURE = 600. For Au NPs translocation experiments, a CO2 laser puller (P-2000, Sutter Instrument) with the following two-line program was used to pull the pipette: Line 1: HEAT = 350, FIL = 3, VEL = 30, DEL = 220, PUL = 0. Line 2: HEAT = 350, FIL = 3, VEL = 40, DEL = 180, PUL = 120. The diameter of the pipette was calculated from the ionic resistance measured in 0.1 M KCl solution at room temperature (**Figure 4.8**).[22]

4.2.5 Gold Nanocluster Deposition

The deposition of the gold cluster at the nanopipette orifice was performed following the procedure from the previous publication with slight modification.[23] First, a nanopipette filled with 25 mM HAuCl4 in 0.1 M KCl was mounted on a glass slide using epoxy, and a pair of Ag/AgCl electrodes were placed in the pipette (working electrode) and chamber (reference electrode), separately. A potential of −0.6 V was applied to initiate deposition upon slow addition of ∼200 μL of freshly prepared 50 mM NaBH4 in ethanol. $NaBH_4$ solution was periodically replenished and added to avoid solution evaporation and bubble formation. Current–time traces were recorded using an Axopatch 200B amplifier.

The resulting gold nanocluster-modified nanopipettes were characterized by cyclic voltammetry in a system where the pipette tip was immersed in 2 mM FcMeOH in 0.1 M KCl, while the back of the pipette was filled with 10 mM ferricyanide in the same buffer.

4.2.6 Electrochemical Measurements

ECL imaging on the Au UME was performed using a Chem-Clamp potentiostat (Dagan) equipped with a headstage (gain N = 0.01). The potentiostat was interfaced with a personal computer via a PCI-6251 data acquisition board (National Instruments) and a BNC-2090 breakout box (National Instruments). A waveform generator (EG&G PARC 175) was connected to the Chem-Clamp to generate the voltage waveform. Data acquisition was carried out using a custom LabView 10.0 program (National Instruments), which received an external trigger signal from the camera to enable synchronized recording of both electrochemical and optical signals.

Gold deposition at the nanopipette orifice was conducted using an Axopatch 200B high-impedance amplifier (Molecular Devices) and a Digidata 1322A digitizer (Molecular Devices), interfaced with a Dell computer. Current–time traces were recorded using pClamp 10.4 Axoscope software (Molecular Devices) with a sampling rate of 100 kHz.

ECL imaging at the gold nanocluster-modified nanopipette orifice was carried out using a Chem-Clamp potentiostat (Dagan) with a headstage of gain N = 1. In amperometric experiments, the Chem-Clamp was connected to a Digidata 1322A digitizer (sampling rate: 100 kHz) to acquire current–time traces. Pulsed voltage waveforms were applied via a 33220A waveform generator (Agilent Technologies) connected to the Chem-Clamp. For cyclic voltammetry measurements, a similar setup to that used for ECL imaging on the Au UME was employed, with the exception of using a headstage with gain N = 1.

Amperometric detection of single nanoparticle (NP) translocation events was performed using the Chem-Clamp potentiostat with a headstage of gain N = 1, interfaced with a Digidata 1322A digitizer. Data were acquired at a 100 kHz sampling rate, with the low-pass filter set to 10 kHz.

4.2.7 Optical Measurements

An Olympus IX70 microscope equipped with a 20× (0.4 NA Olympus Plan N) objective was used to image both Au UMEs and nanopipettes. An Andor Luca S 658 M EMCCD camera cooled to -20 °C (0.6 μs vertical pixel shift speed, and 13.5 MHz readout rate) was used for image recording. A 128×128-pixel window in isolated crop mode was used to obtain fast exposure times with minimal time between frames. For Au UME imaging, the exposure time (frame rate) was 0.05046s (19.8177 Hz) with an EM gain of 20. For nanopipette imaging, an EM gain of 225 and exposure time (frame rate) of 0.10046s (9.9542 Hz) were used. Andor SOLIS and ImageJ were used for image processing. All graphs in the manuscript were created using Origin 2025.

4.3 Results and Discussion

4.3.1 Bipolar ECL Imaging on Au UME

Prior to investigating single Au NPs translocation via closed-bipolar ECL imaging, we first sought to establish closed-bipolar ECL imaging on Au UMEs. The electrochemical cell configuration is illustrated in **Figure 4.2A**. To mimic the asymmetric chemical environment at the nanopipette orifice during Au NPs translocation, two 25 μm Au UMEs were positioned in physically isolated solutions and electrically connected via a cable to form a bipolar electrode. The cathodic pole contained 10 mM KCl, while 25 mM $Ru(bpy)_3^{2+}$, 20 mM DBAE, and 100 mM phosphate buffer (pH 7.4) were included in the anodic pole. The anodic pole was mounted on an inverted microscope for ECL imaging. A low ionic strength solution (10 mM KCl) was selected for the cathodic pole to prevent aggregation of citrate-capped Au NPs, which occurs at ionic concentrations exceeding 20 mM or at pH values below the pKa (3.13) of the citrate capping ligand.[24] The $Ru(bpy)_3^{2+}$/DBAE system was chosen as the ECL probe due to its higher ECL efficiency and reduced toxicity compared to the conventional $Ru(bpy)_3^{2+}$/tripropylamine (TPrA) system.[25] To avoid interference from Ag deposition, instead of Ag/AgCl, Au and Pt wires were employed as driving electrodes in the cathodic and anodic poles, respectively.

The closed bipolar electrochemiluminescence (ECL) signals were detected at a gold ultramicroelectrode (Au UME) using a reversible potential sweep (0 to 4 V). Both electrochemical (I–E) and optical (ECL intensity vs. potential) responses are shown in **Figure 4.2B**. During the forward scan (0 to 3 V), the current and ECL intensity exhibited correlated behavior, with onset potentials near ~1.5 V. To prevent nanoparticle aggregation, no external redox mediators were added to the cathodic pole. Instead, we leveraged the abundance of water molecules as a source of electrons for ECL enhancement, hypothesizing that water reduction (alongside dissolved O_2 reduction) could serve as the cathodic half-reaction. In air-saturated 10 mM KCl (pH ~7.0), the dissolved O_2 concentration (~0.21 mM) supports the following possible cathodic reactions[26]:

$$\mathrm{O_2} + 2\mathrm{H^+} + 2\mathrm{e^-} = \mathrm{H_2O_2},\ E^0 = 0.695\ \mathrm{V\ vs\ NHE} \tag{R1}$$

$$\mathrm{O_2} + 4\mathrm{H^+} + 4\mathrm{e^-} = 2\mathrm{H_2O},\ E^0 = 1.229\ \mathrm{V\ vs\ NHE} \tag{R2}$$

$$2\mathrm{H_2O} + 2\mathrm{e^-} = 2\mathrm{H_2} + 2\mathrm{OH^-},\ E^0 = -0.828\ \mathrm{V\ vs\ NHE} \tag{R3}$$

On the anodic pole, the ECL mechanism involves sequential oxidation of the $Ru(bpy)_3^{2+}$ and the co-reactant DBAE[27]:

$$\mathrm{Ru(bpy)_3^{2+}} = \mathrm{Ru(bpy)_3^{3+}} + \mathrm{e^-},\ E^0 = 1.091\ \mathrm{V\ vs\ NHE} \tag{R4}$$

$$\mathrm{DBAE} = [\mathrm{DBAE^{\cdot}}]^+ + \mathrm{e^-} \tag{R5}$$

$$[\mathrm{DBAE^{\cdot}}]^+ = \mathrm{DBAE^{\cdot}} + \mathrm{H^+} \tag{R6}$$

$$\mathrm{Ru(bpy)_3^{3+}} + \mathrm{DBAE^{\cdot}} = \mathrm{Ru(bpy)_3^{2+*}} + \mathrm{products} \tag{R7}$$

$$\mathrm{Ru(bpy)_3^{2+*}} = \mathrm{Ru(bpy)_3^{2+}} + h\nu \tag{R8}$$

The driving potential across the bipolar electrode can be calculated as:

$$E_{bipolar} = E_{anode} - E_{cathode} \tag{1}$$

where E_{anode} is the driving potential on the anodic pole, and $E_{cathode}$ is the driving potential on the cathodic pole of the bipolar electrode.[10] In the conventional two-electrode configuration (**Figure 4.10**), the cathodic oxygen reduction onset occurs at ~-0.75 V (vs Au QRE), while $Ru(bpy)_3^{2+}$ oxidation begins at ~0.5 V (vs Pt QRE). This yields a theoretical driving voltage of ~1.25 V, similar to the observed ECL onset potential.

Next, a current plateau is observed at 3 V. A similar plateau is seen in the two-electrode system (**Figure 4.10**). In the control experiment without $Ru(bpy)_3^{2+}$/DBAE, the plateau disappears, confirming that it arises from the oxidation of $Ru(bpy)_3^{2+}$/DBAE (R4 to R8). Interestingly, the ECL intensity does not peak during the current plateau but instead reaches its maximum before the steady-state current is established, then declines to a steady value before further decaying. In the two-electrode system, the potential at which the ECL intensity drops coincides with the onset of Au oxidation (to $Au(OH)_n$) in blank phosphate buffer.[28] Above 3.5 V, the ECL intensity decays to nearly zero. While gold surface oxidation inhibits TPrA oxidation (reducing ECL in Rubpy/TprA system),[29] DBAE oxidation is catalyzed by hydroxyethyl species,[25] preserving ECL signals here. Thus, the primary quenching mechanism is water oxidation, which generates O_2, a known quencher of $Ru(bpy)_2^{2+*}$, and also lowers interfacial pH via proton release, further suppressing ECL[29, 30] During the reverse scan (4 → 0 V), ECL signal recovery was limited, likely due to O_2 adsorption on the electrode. Extending the scan to 5 V irreversibly quenched ECL, with no recovery in subsequent cycles (**Figure 4.2C**), consistent with persistent surface oxidation or passivation.

These experiments demonstrate the feasibility of closed-bipolar ECL imaging on Au UMEs, leveraging water reduction as the cathodic half-reaction. The system's stability under controlled potentials (<3.5 V) supports its application for real-time Au NPs translocation imaging studies.

4.3.2 Bipolar ECL Imaging on Gold Nanoclusters Confined in a Nanopipette

Building on our successful demonstration of bipolar ECL imaging at Au UMEs, we next explored whether this approach could be extended to detect bipolar ECL signals from gold nanoclusters deposited at nanopipette orifices. This configuration serves as an important model system for Au NPs translocation studies, as the gold nanocluster closely mimics the behavior of a conductive nanoparticle passing through the nanopore. When positioned at the nanopipette orifice under an applied potential, the nanocluster functions as a nanoscale bipolar electrode, enabling coupled redox reactions at its opposite extremities.[31] This allows us to perform localized bipolar ECL imaging at the nanopipette orifice with nanoscale resolution, establishing the framework for single-nanoparticle translocation imaging experiments.

Deposition of gold nanoclusters at the nanopipette orifice was carried out by a two-step process involving chemical reduction followed by bipolar electrochemical deposition (**Figure 4.3A**).[23] The nanopipette was back-filled with $HAuCl_4$. Upon application of voltage, the addition of $NaBH_4$ induces the electrophoretic migration of $AuCl_4^-$ ions toward the orifice while BH_4^- ions are electrochemically driven into the pipette. The subsequent chemical reduction of $AuCl_4^-$ by BH_4^- yields gold nanoparticles via the following reaction:[23]

$$8\,\mathrm{AuCl_4^-} + 3\,\mathrm{BH_4^-} + 9\,\mathrm{EtOH} \rightarrow 8\,\mathrm{Au\,(s)} + 3\,\mathrm{B(EtO)_3} + 21\mathrm{H^+} + 32\,\mathrm{Cl^-} \qquad \text{(R9)}$$

Initially, the deposition proceeds via chemical reduction until the orifice becomes sufficiently obstructed, preventing direct contact between the internal and external solutions. At this stage, the deposition mechanism transitions to bipolar electrochemical deposition, where $AuCl_4^-$ is reduced at the cathodic pole and BH_4^- is oxidized at the anodic pole. A representative current-time trace for gold deposition in a 178 nm diameter nanopipette is shown in the **Figure 4.3B.** Upon $NaBH_4$ addition, an initial current increase is observed due to the completion of the electrochemical circuit. As deposition progressed, the current gradually decreases as gold nanoclusters partially blocked the orifice. Fluctuations in the current are attributed to nanoparticle formation, dislodgment, and translocation events.[23] By varying the voltage application time, different amounts of gold nanoclusters are deposited at the nanopipette orifice. The resulting gold cluster-modified nanopipettes were characterized by cyclic voltammetry in a system where the tip was immersed in 2 mM FcMeOH in 0.1 M KCl, while the back was filled with 10 mM ferricyanide in the same buffer. As shown in the **Figure 4.3C**, the current decreases compared to the initial ionic resistance measurement (**Figure 4.8**), confirming gold cluster deposition near the orifice. If the orifice has been fully blocked, the nanopipette would have behaved as a closed bipolar nanoelectrode, yielding a steady-state limiting current.[32] However, the observed resistive response, rather than a diffusion-limited current, indicates that for a 178 nm diameter nanopipette, a ~5 min deposition time did not result in complete orifice blockage. One final interesting observation is that we noticed that the deposition can only be successfully performed when nanopipette was placed horizontally. If the nanopipette was placed into solution vertically, no current bloackage can be detected under the same deposition parameters.

Following the deposition, bipolar ECL imaging of the confined gold clusters was performed. As illustrated in **Figure 4.4A**, the experimental setup consists of a nanopipette filled with electrolyte solution and containing an internal Au wire, while an external Pt wire is immersed in the ECL solution surrounding the nanopipette. The nanopipette is horizontally mounted on a coverslip using epoxy and positioned above the microscope objective for ECL imaging. We performed voltage sweeps (0-4 V) using a 178 nm diameter nanopipette containing deposited gold clusters. In this configuration, redox reactions occur in a coupled manner across the nanoscale interface: reduction of species (primarily O_2 and H_2O) within the pipette is electrochemically coupled with oxidation of the ECL-active species ($Ru(bpy)_3^{2+}$/DBAE) in the bulk solution. This bipolar arrangement enables efficient electron transfer between the spatially separated redox processes. The ECL signal emerged at approximately 0.6 V, peaked at 0.9 V. It is worth noticed that this onset poptential is lower than that on Au UME. Subsequently, ECL intensity is decreased until complete quenching occurred at 4 V (**Figure 4.4B**). This quenching correlated with visible bubble formation at higher potentials, consistent with our previous observations on Au UMEs where water oxidation generates both O_2 quenchers and local pH changes. The merged brightfield-ECL image (**Figure 4.4C**) at 0.9 V distinctly localized the emission signal at the nanopipette orifice, confirming the spatial precision of our approach. A control experiment using bare nanopipettes (without gold clusters) yielded no detectable ECL signal (**Figure 4.11**), providing evidence that the observed emission originates specifically from the gold nanoclusters functioning as nanoscale bipolar electrodes. Notably, while the current response (I-E curve) showed only capacitive behavior without redox peaks, the ECL signal provided clear potential-dependent changes. This enhanced sensitivity of optical detection over current measurements is evident in **Figure 4.4C**, which shows distinct ECL emission frames at various potentials. These collective results not only validate gold nanoclusters as effective nanoscale bipolar electrodes but also establish this configuration as a powerful platform for confined ECL studies.

Next, bipolar electrochemiluminescence (ECL) imaging was performed on a gold nanocluster-deposited nanopipette using a potential step method. This approach was chosen to better mimic the conditions of single-nanoparticle (NP) translocation experiments, where a constant potential is maintained during detection. The experimental setup was identical to that used in **Figure 4.4A**, except that a potential step was applied to the nanopipette instead of a liner potential sweep. Initially, the nanopipette was held at 0 V, a potential insufficient to drive the coupled reduction and ECL reactions. After 1 s, the potential was stepped to 4 V, which is well beyond the threshold required for the reaction based on the CV in **Figure 4.4B**. As shown in **Figure 4.5**, no ECL signal was observed at 0 V, remaining at baseline. Upon stepping to 4 V, the ECL signal was still absent, consistent with the potential sweep data discussed earlier, which is likely due to quenching by water oxidation at the anodic pole under high voltage. Notably, pre-application of a negative potential prior to the 4 V step significantly influenced the ECL response. When moderate negative potentials (–1 V to –3 V) were applied before stepping to 4 V, a transient ECL spike was observed, followed by rapid quenching due to the high oxidative potential. However, when a more negative potential (–4 V) was applied, the ECL signal persisted for nearly 1 s, matching the duration of the potential step. While the precise mechanism requires further investigation, we hypothesize that the negative potential promotes the pre-concentration of $Ru(bpy)_3^{2+}$ within the nanocluster-modified region, potentially through enhanced electroosmotic and electrophoretic fluxes. Regardless of the origin, these findings confirm that bipolar ECL detection at the nanopipette orifice is achievable under constant potentials, and signal amplification can be strategically modulated through pulsed potential sequences.

4.3.3 Attempts at Detection of Single Au Nanoparticle Translocation with Bipolar ECL

The successful ECL imaging of gold nanoclusters at the nanopipette orifice confirms that nanoclusters/nanoparticles at the orifice can serve as bipolar electrodes, coupling ECL reactions with other redox processes. Based on this finding, we shifted our focus to detect Au NPs translocation using bipolar ECL imaging. To improve the sensitivity of the ECL imaging, a relatively large sized nanoparticle (147 nm) is used for translocation experiments (**Figure 4.9**).

Our initial experimental setup is illustrated in **Figure 4.6A**. A 178 nm nanopipette was backfilled with an ECL solution (25 mM Ru(bpy)$_3^{2+}$, 20 mM DBAE in 100 mM phosphate buffer), and the tip was immersed in a 10 mM KCl solution containing 147 nm Au NPs (2.74 pM). A pressure of ~1 PSI was applied to draw Au NPs into the nanopipette. **Figure 4.6B** shows simultaneously recorded current and ECL signals under an applied potential of -4 V. The current signal (blue trace) exhibits discrete spikes, indicating Au NPs translocation into the nanopipette. However, despite the high translocation frequency (153 Hz), the ECL signal shows no spikes or correlation with the current signal. Notably, no current spikes were observed under +4 V. Since both the glass nanopipette and Au NPs are negatively charged under neutral conditions, we attribute the translocation driving force to electroosmotic flow.[33] Intriguingly, under -4 V, the current trace displayed conductive peaks rather than the expected resistive peaks. This current enhancement phenomenon has been previously reported[34, 35] and was also observed in Chapter 3. A possible explanation is that the counterion cloud around the Au NPs increases local ion density near the nanopipette orifice.[35] Additionally, we propose that the coupled bipolar reaction generates faradaic current, further enhancing the signal. However, as this chapter focuses on ECL imaging, a detailed discussion of current enhancement will be reserved for future research. Statistical analysis of the conductive current peaks (**Figure 4.6C&D**) reveals an average peak current of -251.29 ± 94.02 pA with a corresponding half-width of 0.71 ± 0.16 ms. In a previous study on transient nanoparticle collisions detected via closed bipolar ECL imaging, researchers noted the absence of sharp current spikes (attributed to hydrogen adsorption) in the ECL signal.[20] The study estimated the charge for the undetected hydrogen adsorption process at 403 ± 90 fC, suggesting that the ECL detection sensitivity falls below this level. If we assume that the conductive peaks in our system arise solely from faradaic current due to coupled redox reactions, the average charge per translocation event would only be 182 ± 119 fC, which is significantly lower than the ECL detection sensitivity. Furthermore, in translocation systems, the measured current includes both ionic current (from the translocation process) and faradaic current.[36] As a result, the number of electrons transferred is lower than we expected, which may explain the absence of ECL signals.

Unlike immobilized gold nanoclusters at the nanopipette orifice (where ECL imaging does not require high temporal resolution), the rapid translocation of Au NPs introduces challenges in both temporal resolution and detection sensitivity for real-time ECL imaging. To address this, we modified the experimental setup (**Figure 4.7A**). The nanopipette (90 nm diameter, smaller than the 147 nm Au NPs) was backfilled with a 2.7 pM Au NP suspension in 10 mM KCl, followed by the addition of ~200 μL ECL solution at the tip. We propose that under an applied voltage, Au NPs migrate toward the orifice but become trapped due to size exclusion. At sufficiently high voltages, these trapped NPs act as wireless nanopore electrodes, enabling bipolar electrochemical reactions and subsequent ECL emissions.

Figure 4.7B displays amperometric traces of Au NP translocation at –2 V, –2.5 V, and –3 V (all voltages are applied from inside the pipette pore to the outside). Despite the inverted solution configuration compared to the first experimental setup, translocation signals were only observed under negative voltages. Even at the same Au NPs concentration, translocation frequency was significantly reduced in this configuration. Additionally, conductive signals were detected, with translocation frequency and current amplitude increasing sharply from –2 V to –3 V. Unlike the first setup, where only sharp current spikes were observed, this configuration exhibited a fast spike followed by a slow decay (**Figure 4.7D**). The decay durations were 10.44 ± 17.85 ms (–2 V), 11.22 ± 21.92 ms (–2.5 V), and 12.18 ± 24.23 ms (–3 V), with some events exceeding 150 ms, which is far longer than the transient spikes in the initial setup.

Previous studies report staircase or spike-shaped currents when nanoparticles larger than the nanopore interacts with the orifice.[37, 38] A staircase signal corresponds to nanoparticle capture and hold, while spikes indicate nanoparticle collisions and departure. The authors attribute these differences to dynamic changes in electroosmotic, electrophoretic, and dielectrophoretic forces under varying voltages and particle properties. In our system, the negatively charged nanopipette surface (in 10 mM KCl) generates electroosmotic flow (EOF) that drives NPs away from the orifice, while electrophoresis moves them toward it. At more negative voltages, enhanced electrophoresis increases NP entry into the sensing zone. However, NPs are still repelled through EOF afterwards.[38] Further studies are needed to fully elucidate NP dynamics in this bipolar system.

Figure 4.7B also shows synchronized current and ECL measurements under different voltages. Surprisingly, no ECL spikes or correlations with current signals were observed. Increasing the voltage to -4 V induced strong current oscillations but no detectable ECL spikes. We initially suspected that excessive voltage led to water reduction, quenching ECL. However, even at lower voltages, ECL signals remained absent. Assuming the current rises solely from faradaic processes, the largest peak (26,040 fC over 20 ms) would correspond to significant charge transfer. However, since the measured current includes both ionic and faradaic contributions, the actual faradaic charge, and thus ECL-generating electron transfer, is far lower, likely explaining the absence of ECL. The ECL efficiency (photons per electron) in the $Ru(bpy)_3^{2+}$/DBAE system is ~0.05.[30] If 26,040 fC were purely faradaic, ~8.1×10^6 photons would be generated. Although the current duration is prolonged due to the slow decay component in this configuration (where nanoparticles are larger than the nanopore), the observed charge transfer remains significantly smaller than the threshold required for detectable ECL events. Previous studies of transient nanoparticle collisions, such as those involving hydrogen evolution, report detectable signals only with substantially larger charge transfers (-80.71 ± 36.48 pC over 400 ms).[39] Our system's smaller charge transfer and shorter signal duration fall below this detection limit.

To improve ECL detection, future work could employ larger nanoparticles or glass surface modifications to enhance NP trapping at the orifice, ensuring prolonged electrode-like behavior during translocation.

4.4 Conclusion

In this study, we investigate the potential of bipolar electrochemiluminescence (ECL) imaging as a powerful tool for monitoring conductive nanoparticle translocation events. Our systematic approach progresses from fundamental studies on Au UMEs to nanoscale investigations using gold nanoclusters confined within nanopipettes, demonstrating that spatially coupled redox reactions, specifically water/O_2 reduction at the cathodic pole and $Ru(bpy)_3^{2+}$/DBAE oxidation at the anodic pole, can generate stable and spatially resolved ECL signals under nanoconfinement. The successful observation of localized ECL emissions at nanopipette orifices confirms that gold nanoclusters function as efficient wireless nanopore electrodes, with signal generation and modulation directly controlled by the applied potential. These results highlight the exceptional spatial resolution achieved through this nanoscale bipolar ECL system.

However, applications of this approach to real-time detection of translocating Au nanoparticles encounter significant challenges. The transient nature of nanoparticle translocation results in both limited charge transfer and insufficient event duration for detectable ECL generation. These findings reveal critical limitations in the current system's ability to balance nanoparticle residence time, faradaic efficiency, and optical sensitivity for single-entity detection. Future advancements may overcome these limitations through several promising approaches including implementation of nanoparticle trapping mechanisms and surface-modified nanopipettes to prolong residence time and enhance faradaic processes, or adoption of alternative ECL systems with superior quantum yields. By establishing these fundamental design principles, our work not only advances the understanding of nanoscale bipolar electrochemistry but also provides a clear pathway toward achieving optical tracking of transient nanoscale events through ECL detection.

4.5 Figures

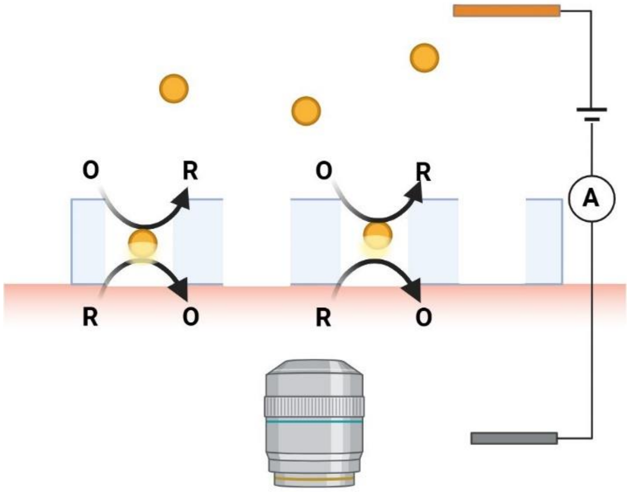

Figure 4.1. Detection scheme for bipolar ECL imaging of Au NPs translocation on nanopore array.

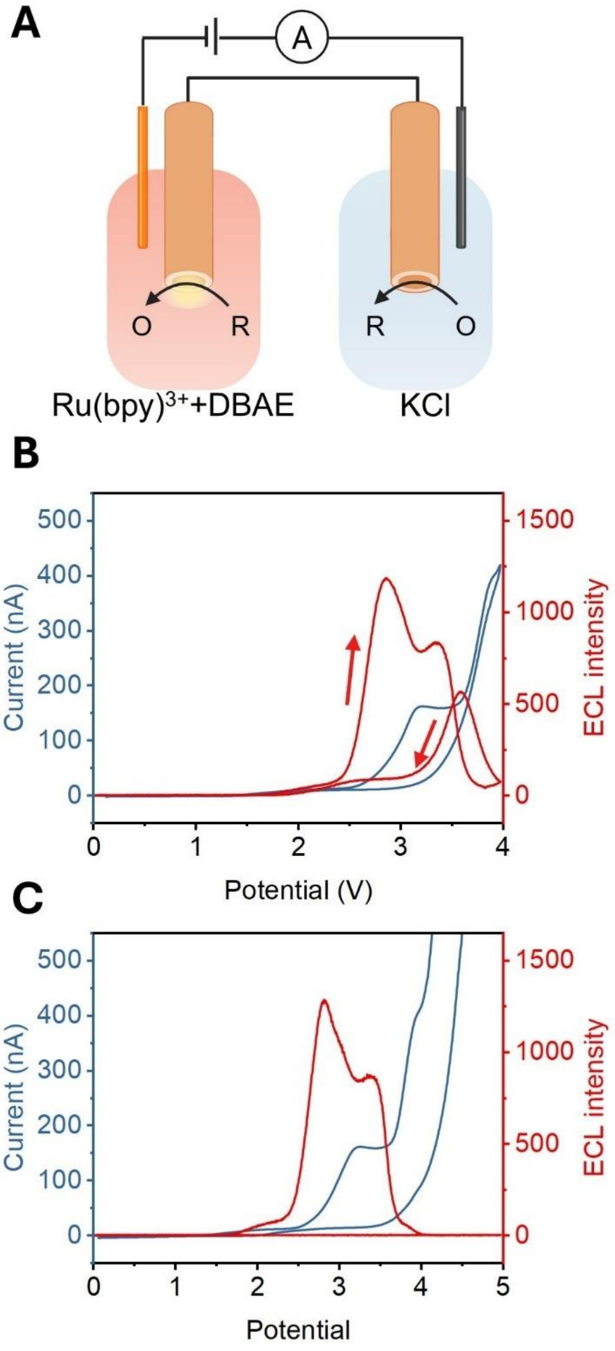

Figure 4.2. Closed bipolar ECL imaging on Au UMEs.
(A) Schematic illustration of the experimental configuration for closed bipolar ECL imaging. (B) Simultaneous voltammetric (blue) and optical ECL (red) responses during the potential sweep from 0 to 4 V. (C) Corresponding voltammetric (blue) and ECL (red) signals during the extended potential sweep from 0 to 5 V.

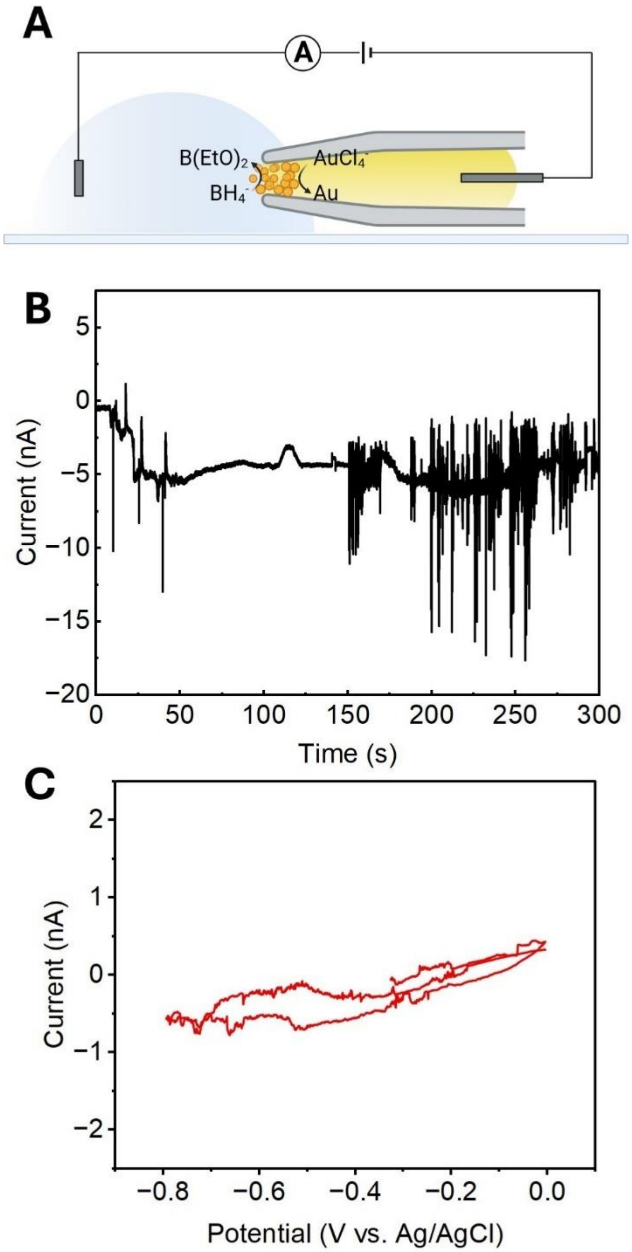

Figure 4.3. Gold nanocluster deposition and characterization at nanopipette orifices.
Schematic of the electrochemical deposition setup: a nanopipette backfilled with 25 mM HAuCl4 in 0.1 M KCl is immersed in 50 mM $NaBH_4$ (in ethanol), with Ag/AgCl driving electrodes applying −600 mV for Au reduction. (B) Representative current-time trace during Au deposition in a 178 nm nanopore, reflecting nucleation dynamics and nanopore blocking. (C) Voltammetric characterization of the Au-modified nanopipette in a bipolar configuration, with the tip immersed in 2 mM ferrocenemethanol (FcMeOH) and the back filled with 10 mM ferricyanide ($Fe(CN)_6^{3-}$).

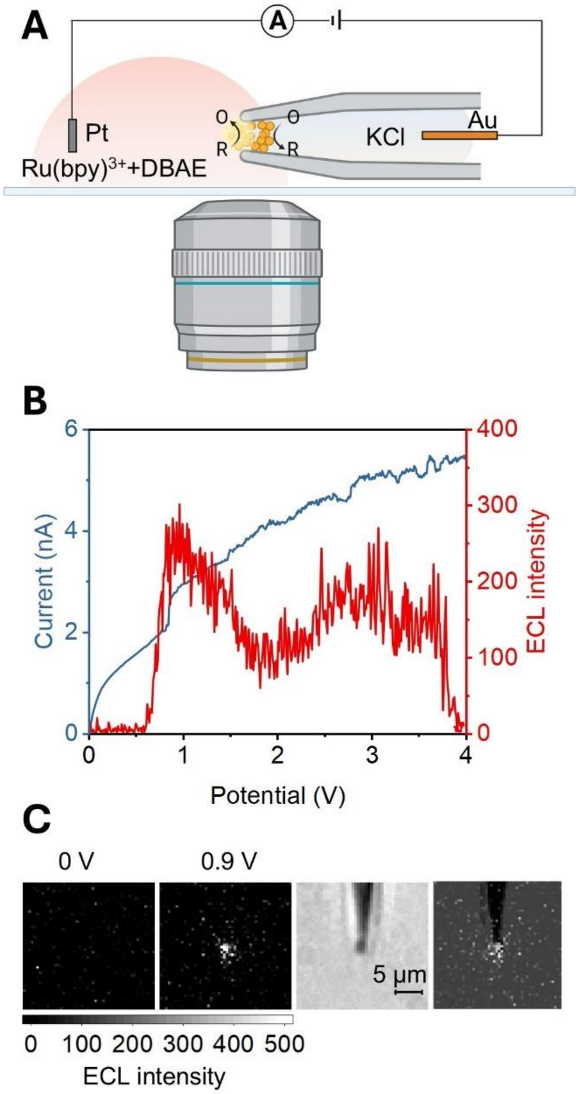

Figure 4.4. Bipolar ECL imaging of nanoconfined gold nanoclusters.

(A) Schematic of the experimental configuration for nanoscale bipolar ECL measurements. (B) Synchronized (top) ECL intensity and (bottom) voltammetric responses during the potential sweep, showing potential-dependent emission from deposited gold nanoclusters. Overlay of bright-field microscopy and ECL emission (0.8 V) at the nanopipette orifice, which demonstrates spatial localization of the signal. (C) The first two figures are ECL images recorded at applied potentials of 0 V (no emission) and 0.9 V (active ECL signal). Followed by bright-field microscopy image of the nanopipette and an overlay of ECL emission with the nanopipette.

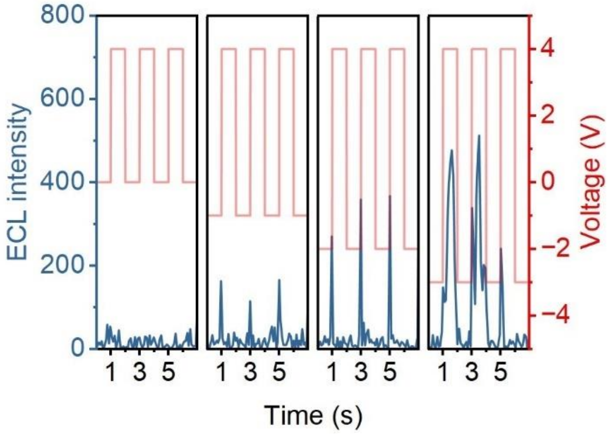

Figure 4.5. Potential-step triggered ECL from nanoconfined gold nanoclusters.

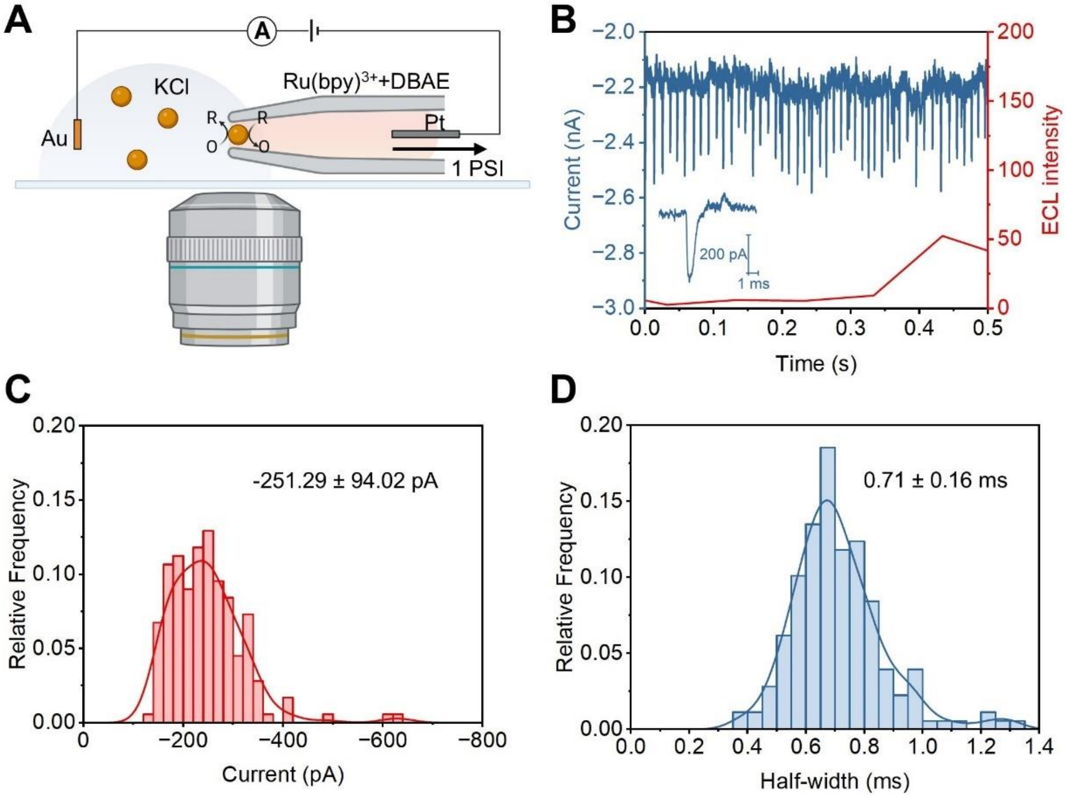

Figure 4.6. ECL monitoring of Au NPs translocation through larger nanopores.
(A) Schematic of the experimental configuration for simultaneous current and ECL detection. (B) Synchronized current (blue) and ECL (red) transient signals during AuNP translocation events at -4 V. (C) Statistical distribution of translocation current amplitudes. (D) Histogram of the half-width of translocation events. The "n" values for (C) to (D) are all equal to 178.

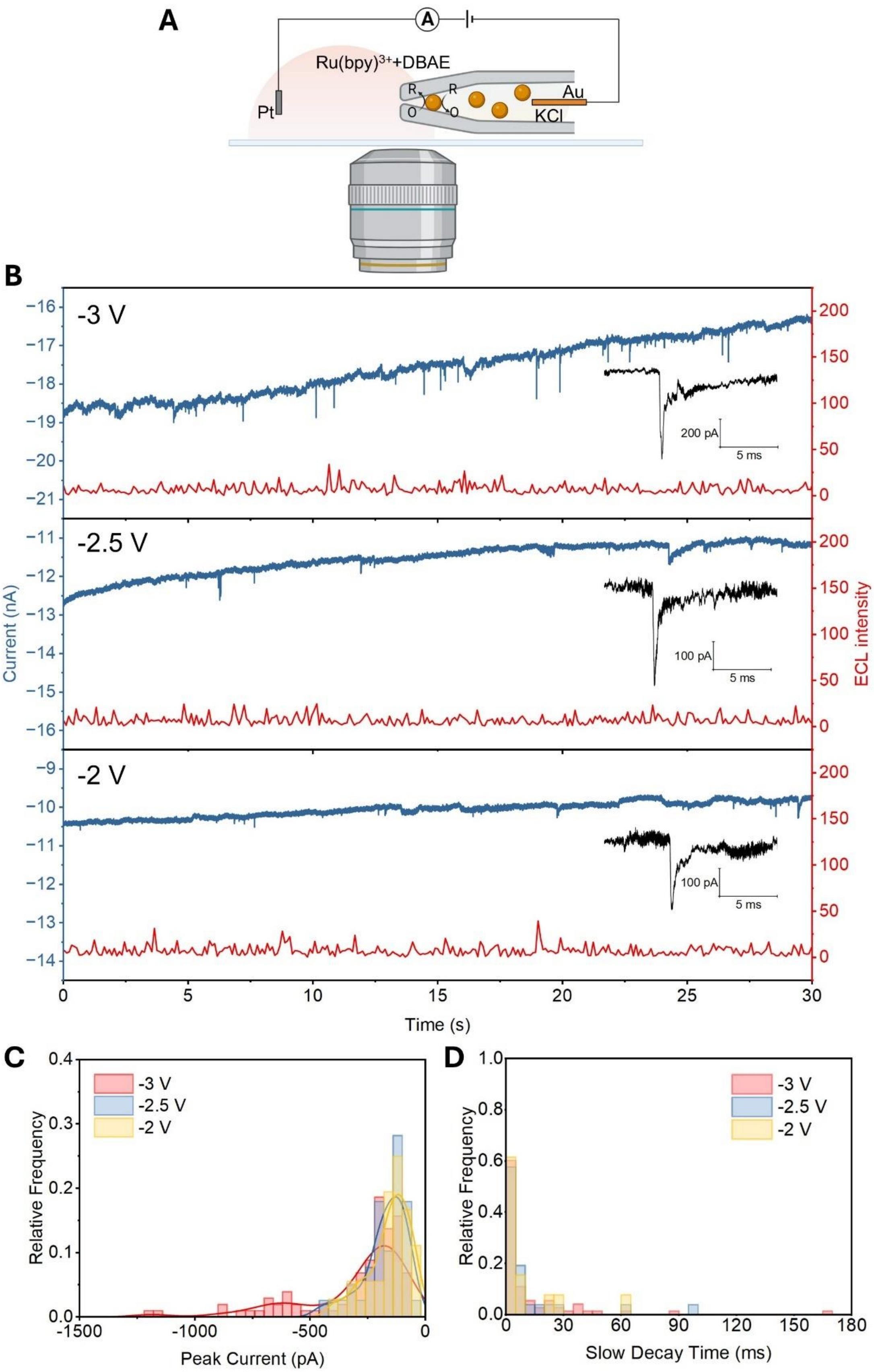
A
Ru(bpy)$^{3+}$+DBAE
Pt
R
O
R
O
Au
KCl
B
-3 V
200 pA
5 ms
-2.5 V
100 pA
5 ms
-2 V
100 pA
5 ms
Current (nA)
ECL intensity
Time (s)
C
-3 V
-2.5 V
-2 V
Relative Frequency
Peak Current (pA)
D
-3 V
-2.5 V
-2 V
Relative Frequency
Slow Decay Time (ms)

Figure 4.7. ECL detection of gold nanoparticle translocation through size-exclusion nanopores. (A) Schematic of the experimental configuration with a 90 nm nanopipette (smaller than 147 nm AuNPs). (B) Simultaneous amperometric (blue) and ECL (red) recordings at different applied potentials (-2 V, -2.5 V, -3 V), with insets showing representative translocation events. (C) Distribution of translocation peak currents (n = 17, 33, and 80 events for -2 V, -2.5 V, and -3 V, respectively). (D) Duration analysis of translocation events showing slow decay time distributions at each potential.

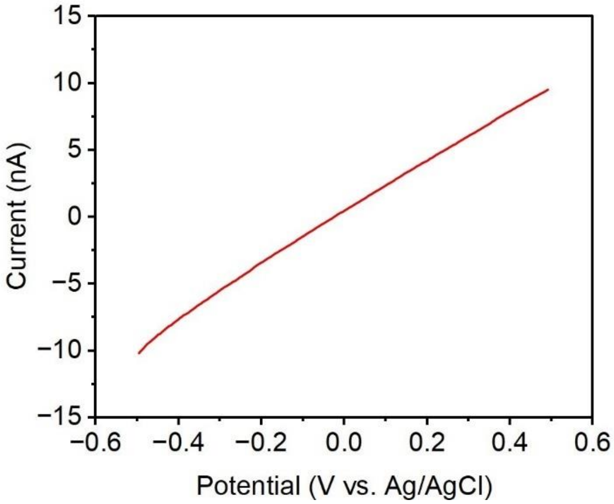

Figure 4.8. Characterization of nanopipette size.
A representative *i-V* curve of a 178 nm diameter pipette nanopore in 100 mM KCl. The scan rate was 100 mV/s. The pipette pore diameter was calculated from the ionic resistance and the cone angle. The potential was applied between two Ag/AgCl quasi-reference electrodes (QREs).

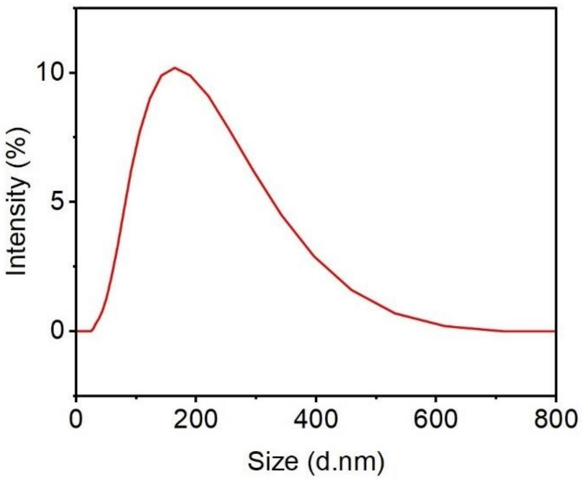

Figure 4.9. Au NPs size distribution analysis by dynamic light scattering (DLS).

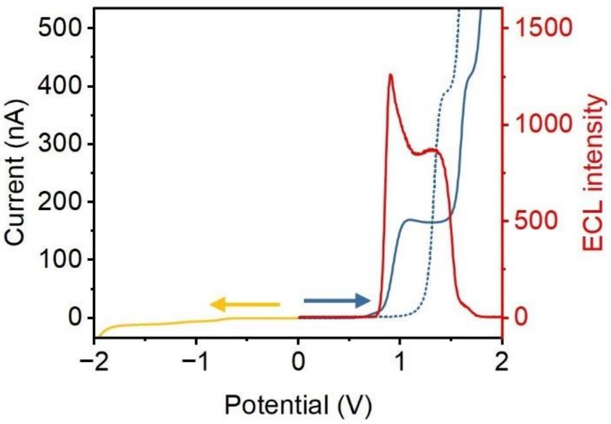

Figure 4.10. ECL characterization in a two-electrode system.
Cyclic voltammograms (blue) and corresponding ECL responses (red) for a 25 μm Au UME in 25 mM Ru(bpy)$_3^{2+}$/20 mM DBAE (100 mM phosphate buffer, pH 7.4). Control measurement shows the background current in a blank phosphate buffer (blue dashed line). The yellow line is the electrochemical response of Au UME in 10 mM KCl. Scan rate: 100 mV/s.

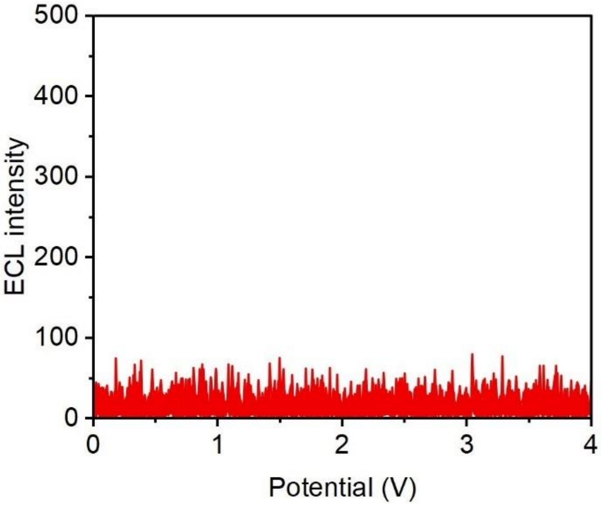

Figure 4.11. ECL response of a nanopipette without gold clusters deposition.
178 nm nanopipette was backfilled with 10 mM KCl, and the tip was immersed in ECL solution. The scan rate is 100 mV/s.

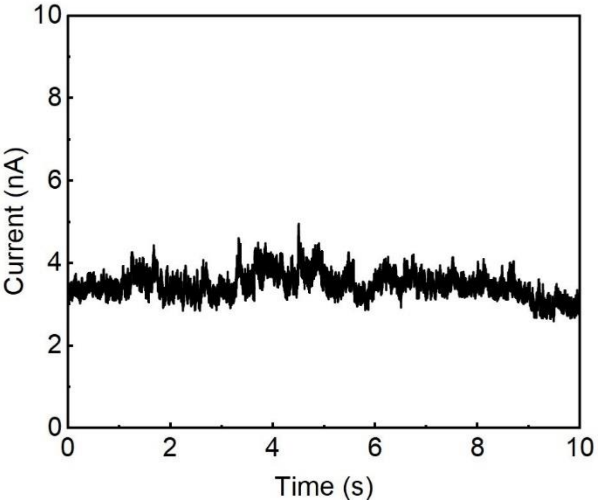

Figure 4.12. Example trace of Au NPs translocation under 4 V.

4.6 References

(1) Zhang, L.; Wahab, O. J.; Jallow, A. A.; O'Dell, Z. J.; Pungsrisai, T.; Sridhar, S.; Vernon, K. L.; Willets, K. A.; Baker, L. A. Recent Developments in Single-Entity Electrochemistry. *Anal. Chem.* **2024**, *96*, 8036–8055.

(2) Baker, L. A. Perspective and Prospectus on Single-Entity Electrochemistry. *J. Am. Chem. Soc.* **2018**, *140*, 15549–15559.

(3) Zhang, J. H.; Shen, Q.; Zhou, Y. G. Quantification of Tumor Protein Biomarkers from Lung Patient Serum Using Nanoimpact Electrochemistry. *ACS. Sens.* **2021**, *6*, 2320–2329.

(4) Lemay, S. G.; Moazzenzade, T. Single-Entity Electrochemistry for Digital Biosensing at Ultralow Concentrations. *Anal. Chem.* **2021**, *93*, 9023–9031.

(5) Gao, R.; Edwards, M. A.; Harris, J. M.; White, H. S. Shot Noise Sets the Limit of Quantification in Electrochemical Measurements. *Curr. Opin. Electrochem.* **2020**, *22*, 170–177.

(6) Wheeler, K.; Gott, J.; Roehrich, B.; Chung, J.; Kajal, K.; Syzdek, J.; Hespanha, J.; Sepunaru, L. Investigation of Noise at a Microelectrode during a Faradaic Reaction. *ACS Electrochemistry* **2025**, *1*(4), 552–559

(7) Lei, C.; Hu, D. High Throughput Mapping of Single Molecules' Redox Potentials on Electrode. *Anal. Chem.* **2021**, *93*, 8864–8871.

(8) Liu, Y.; Holzinger, A.; Knittel, P.; Poltorak, L.; Gamero-Quijano, A.; Rickard, W. D. A.; Walcarius, A.; Herzog, G.; Kranz, C.; Arrigan, D. W. M. Visualization of Diffusion within Nanoarrays. *Anal. Chem.* **2016**, *88*, 6689–6695.

(9) McNally, B.; Singer, A.; Yu, Z.; Sun, Y.; Weng, Z.; Meller, A. Optical Recognition of Converted DNA Nucleotides for Single-Molecule DNA Sequencing Using Nanopore Arrays. *Nano Lett.* **2010**, *10*, 2237–2244.

(10) Han, C.; Hao, R.; Fan, Y.; Edwards, M. A.; Gao, H.; Zhang, B. Observing Transient Bipolar Electrochemical Coupling on Single Nanoparticles Translocating through a Nanopore. *Langmuir* **2019**, *35*, 7180–7190.

(11) Pitchford, W. H.; Kim, H. J.; Ivanov, A. P.; Kim, H. M.; Yu, J. S.; Leatherbarrow, R. J.; Albrecht, T.; Kim, K. B.; Edel, J. B. Synchronized Optical and Electronic Detection of Biomolecules Using a Low Noise Nanopore Platform. *ACS Nano* **2015**, *9*, 1740–1748.

(12) Schmeltzer, A. J.; Peterson, E. M.; Harris, J. M.; Lathrop, D. K.; German, S. R.; White, H. S. Simultaneous Multipass Resistive-Pulse Sensing and Fluorescence Imaging of Liposomes. *ACS Nano* **2024**, *18*, 7241–7252.

(13) Iwama, T.; Inoue, K. Y.; Abe, H.; Matsue, T. Chemical Imaging Using a Closed Bipolar Electrode Array. *Chem. Lett.* **2018**, *47*, 843–845.

(14) Li, G.; Hao, R. Focused Ion Beam Fabrication of High-Resolution Electrochemical-Electroluminescence Coupling Bipolar Nanoelectrode Array *Sensors. Sens. Actuators Rep.* **2024**, *8*, 100220.

(15) Anderson, T. J.; Defnet, P. A.; Zhang, B. Electrochemiluminescence (ECL)-Based Electrochemical Imaging Using a Massive Array of Bipolar Ultramicroelectrodes. *Anal. Chem.* **2020**, *92*, 6748–6755.

(16) Wu, Y.; Gu, Q.; Wang, Z.; Tian, Z.; Liu, H.; Liu, S. Ultrasensitive Electrochemiluminescence Imaging Detection of Multiple MiRNAs in Single Cells with a Closed Bipolar Electrode Array Chip. *Anal. Chem.* **2024**, *96*, 12112–12119.

(17) Wu, Y.; Gu, Q.; Wang, Z.; Tian, Z.; Wang, Z.; Liu, W.; Han, J.; Liu, S. Electrochemiluminescence Analysis of Multiple Glycans on Single Living Cell with a Closed Bipolar Electrode Array Chip. *Anal. Chem.* **2024**, *96*, 2165–2172.

(18) Sciuto, E. L.; Santangelo, M. F.; Villaggio, G.; Sinatra, F.; Bongiorno, C.; Nicotra, G.; Libertino, S. Photo-Physical Characterization of Fluorophore $Ru(Bpy)_3^{2+}$ for Optical Biosensing Applications. *Sens. Biosensing Res.* **2015**, *6*, 67–71.

(19) Yu, S.; Mehrgardi, M.; Shannon, C. A Bipolar Electrochemical Sensor with Square Wave Excitation and ECL Readout. *Electrochem. Commun.* **2018**, *88*, 24–28.

(20) Defnet, P. A.; Zhang, B. Detection of Transient Nanoparticle Collision Events Using Electrochemiluminescence on a Closed Bipolar Microelectrode. *ChemElectroChem* **2020**, *7*, 252–259.

(21) Liu, X.; Xu, H.; Xia, H.; Wang, D. Rapid Seeded Growth of Monodisperse, Quasi-Spherical, Citrate-Stabilized Gold Nanoparticles via H_2O_2 Reduction. *Langmuir* **2012**, *28*, 13720–13726.

(22) Guerrette, J. P.; Zhang, B. Scan-Rate-Dependent Current Rectification of Cone-Shaped Silica Nanopores in Quartz Nanopipettes. *J. Am. Chem. Soc.* **2010**, *132*, 17088–17091.

(23) Wood, M.; Zhang, B. Bipolar Electrochemical Method for Dynamic in Situ Control of Single Metal Nanowire Growth. *ACS Nano* **2015**, *9*, 2454–2464.

(24) Xiang, Z.; Deng, H.; Peljo, P.; Fu, Z.; Wang, S.; Mandler, D.; Sun, G.; Liang, Z. Electrochemical Dynamics of a Single Platinum Nanoparticle Collision Event for the Hydrogen Evolution Reaction. *Angew. Chem.* **2018**, *130*, 3522–3526.

(25) Liu, X.; Shi, L.; Niu, W.; Li, H.; Xu, G. Environmentally Friendly and Highly Sensitive Ruthenium(II) Tris(2,2′-Bipyridyl) Electrochemiluminescent System Using 2-(Dibutylamino)Ethanol as Co-Reactant. *Angew. Chem. Int. Ed.* **2007**, *46*, 421–424.

(26) Zhang, Y.; Robinson, D. A.; McKelvey, K.; Ren, H.; White, H. S.; Edwards, M. A. A High-Pressure System for Studying Oxygen Reduction During Pt Nanoparticle Collisions. *J. Electrochem. Soc.* **2020**, *167*, 166507.

(27) Xue, L.; Guo, L.; Qiu, B.; Lin, Z.; Chen, G. Mechanism for Inhibition of $Ru(Bpy)_3^{2+}$/DBAE Electrochemiluminescence System by Dopamine. *Electrochem. Commun.* **2009**, *11*, 1579–1582.

(28) Burke, L. D.; Nugent, P. F. The Electrochemistry of Gold: I. The Redox Behaviour of the Metal in Aqueous Media. *Gold Bull.* **1997**, *30*, 43–53.

(29) Zu, Y.; Bard, A. J. Electrogenerated Chemiluminescence. 66. The Role of Direct Coreactant Oxidation in the Ruthenium Tris(2,2')Bipyridyl/Tripropylamine System and the Effect of Halide Ions on the Emission Intensity. *Anal. Chem.* **2000**, *72*, 3223–3232.

(30) Richter, M. M. Electrochemiluminescence (ECL). *Chem. Rev.* **2004**, *104*, 3003–3036.

(31) Gao, R.; Lin, Y.; Ying, Y. L.; Hu, Y. X.; Xu, S. W.; Ruan, L. Q.; Yu, R. J.; Li, Y. J.; Li, H. W.; Cui, L. F.; et al. Wireless Nanopore Electrodes for Analysis of Single Entities. *Nat. Protoc.* **2019**, *14*, 2015–2035.

(32) Bard, A. J.; Faulkner, L. R.; White, H. S. *Electrochemical Methods: Fundamentals and Applications*; Wiley, **2022**.

(33) Lan, W. J.; Holden, D. A.; Zhang, B.; White, H. S. Nanoparticle Transport in Conical-Shaped Nanopores. *Anal. Chem.* **2011**, *83*, 3840–3847.

(34) Lan, W. J.; Kubeil, C.; Xiong, J. W.; Bund, A.; White, H. S. Effect of Surface Charge on the Resistive Pulse Waveshape during Particle Translocation through Glass Nanopores. *J. Phys. Chem. C.* **2014**, *118*, 2726–2734.

(35) Goyal, G.; Freedman, K. J.; Kim, M. J. Gold Nanoparticle Translocation Dynamics and Electrical Detection of Single Particle Diffusion Using Solid-State Nanopores. *Anal. Chem.* **2013**, *85*, 8180–8187.

(36) Yu, R. J.; Xu, S. W.; Paul, S.; Ying, Y. L.; Cui, L. F.; Daiguji, H.; Hsu, W. L.; Long, Y. T. Nanoconfined Electrochemical Sensing of Single Silver Nanoparticles with a Wireless Nanopore Electrode. *ACS Sens.* **2021**, *6*, 335–339.

(37) Xu, C.; Liu, Y.; Xiong, T.; Wu, F.; Yu, P.; Wang, J.; Mao, L. Dynamic Behavior of Charged Particles at the Nanopipette Orifice. *ACS Sens.* **2021**, *6*, 2330–2338.

(38) Li, T.; He, X.; Zhang, K.; Wang, K.; Yu, P.; Mao, L. Observing Single Nanoparticle Events at the Orifice of a Nanopipet. *Chem. Sci.* **2016**, *7*, 6365–6368.

(39) Defnet, P. A.; Han, C.; Zhang, B. Temporally-Resolved Ultrafast Hydrogen Adsorption and Evolution on Single Platinum Nanoparticles. *Anal. Chem.* **2019**, *91*, 4023–4030.

CHAPTER 5 CLOSED BIPOLAR IMAGING USING OFF-AXIS DARK FIELD MICROSCOPY

5.1 Introduction

Electrochemical imaging enables the spatially and temporally resolved probing of redox-active species in chemical and biological systems. Current electrochemical imaging techniques fall into two primary categories: scanning probe-based methods and optical microscopy-coupled approaches. In scanning probe-based techniques, such as scanning ion conductance microscopy (SICM) and scanning electrochemical cell microscopy (SECCM), a nanoscale probe (e.g., an ultramicroelectrode or nanopipette) is scanned across a sample surface while recording currents. Collected currents are then used to construct maps of electrochemical activity and surface topography. [1] While scanning probe methods achieve exceptional spatial resolution (e.g., <100 nm),[2] the speed of scanning restricts real-time studies. In contrast, optical-electrochemical imaging combines synchronized optical and current measurements, offering improved spatiotemporal resolution and enabling real-time observation of redox processes.[3]

In optical-electrochemical imaging, electrochemiluminescence (ECL)[4]and fluorescence[5]are widely employed as light-generating systems, where ECL emitters or redox-mediated fluorophores undergo oxidation/reduction to modulate light emission. These light-generation processes can be coupled with complementary analyte half-reactions through bipolar electrochemistry, enabling optical monitoring of electrochemical dynamics.[6]Unlike conventional electrochemistry, where redox reactions are confined to a working electrode, bipolar electrochemistry involves two coupled half-reactions occurring at opposite poles of a bipolar electrode (BPE). Bipolar electrochemistry is typically performed in either open or closed configurations. In the open configuration, the BPE is fully immersed in a single electrolyte, and a high external voltage (≥20–30 V) is applied between driving electrodes to polarize the BPE and drive redox reactions at its anodic and cathodic poles.[7]In contrast, the closed configuration physically separates the two poles into different solutions, blocking ionic current flow between them. As a result, a significantly lower driving voltage (< 2 V) is sufficient to drive faradaic reactions at both poles.[8] Massive parallel closed BPE array has gained attention in electrochemical imaging due to its excellent spatial resolution. Coupling with redox reaction of fluorophores or ECL emitters, the electrochemical reactions at one side of the closed BPE arrays can be read out by fluorescence or ECL signals at another side.[9] Closed BPE array has been successfully applied in diverse sensing applications, including single-cell imaging[10] and electrocatalyst screening[11]. However, the current utility of this technique is constrained by the limited selection of efficient ECL emitters (e.g., tris(2,2′-bipyridyl)ruthenium(II) and luminol) and redox-mediating fluorophores (e.g., resorufin and dihydroresorufin).

Dark-field microscopy (DFM) has emerged as a powerful label-free imaging technique, offering high sensitivity and rapid acquisition without the need for fluorescent or electrochemiluminescent (ECL) probes. In DFM, oblique illumination prevents direct transmission of incident light into the objective, creating a dark background while selectively collecting light scattered or emitted by the sample.[12]The scattering signal is further enhanced through localized surface plasmon resonance (LSPR) effects[13], refractive index variations[14], and elastic scattering[15], enabling real-time optical monitoring of *in situ* electrodeposition processes for single plasmonic nanoparticles. For instance, DFM has been employed to track the heterogeneous electrodeposition of single Ag[16], Pd[17], Co[18], and Ni[19] nanoparticles. Furthermore, DFM enables real-time monitoring of Cu_2O/Au nanostructure growth through scattering signal feedback. The resulting nanostructures exhibit enhanced electrocatalytic activity for glucose oxidation, enabling ultrasensitive glucose detection.[20]

The unique capability of DFM to resolve metal nanoparticle dynamics motivates its integration with closed bipolar electrochemistry (BPE), where electrodeposited nanoparticles could serve as the light-generating pole. However, conventional DFM requires optically transparent electrodes (e.g., indium tin oxide, ITO), which are prone to electrochemical dissolution under acidic conditions during cathodic or anodic polarization, limiting their utility in BPE systems.[21,22] Additionally, non-transparent electrodes (e.g., carbon fiber) introduce strong scattering from insulating materials, obscuring nanoparticle-derived signals.

To overcome these limitations, our group established an off-axis DFM configuration that spatially separates illumination from detection. [23] In this design, a low-numerical-aperture (NA) objective positioned perpendicular to the collection optics directs incident light such that nanoparticle scattering is selectively detected while background electrode scattering is minimized. Leveraging this platform, we now demonstrate its integration with closed bipolar electrochemistry, creating a novel imaging system where nanoparticle electrodeposition at the reporting pole is monitored via off-axis DFM while simultaneous analyte detection occurs at the sensing pole. This combination merges the exceptional spatial resolution of plasmonic nanoparticle imaging with the inherent advantages of closed BPE systems. Furthermore, the system's versatility is enhanced through multiple compatible metal deposition options (e.g., Ag, Au), where selection of metals with stronger scattering cross-sections can further improve detection sensitivity. This approach opens new possibilities for spatially resolved electrochemical analysis with enhanced optical detection capabilities.

As the first step toward high spatial resolution imaging on large arrays, we therefore sought to use well-established copper electrodeposition and hydrogen peroxide oxidation as our cBPE system to explore bipolar optical detection based on off-axis DFM as proof of concept. In this chapter, we first employed off-axis DFM to achieve real-time, *in situ* imaging of copper electrodeposition on carbon fiber electrodes. We then established a quantitative sensing platform for hydrogen peroxide by coupling its oxidation at a closed bipolar electrode with copper electrodeposition, where the scattered light intensity provides a direct measure of H_2O_2 concentration. To demonstrate the versatility of this approach, we integrated a glucose oxidase (GOx)-modified electrode into the system, enabling closed bipolar electrochemical glucose detection. The GOx-modified electrode was systematically characterized by monitoring enzymatically generated H_2O_2, and the enzyme loading was optimized for enhanced performance. Finally, we demonstrated quantitative glucose sensing by combining the oxidation of GOx-derived H_2O_2 with real-time, off-axis dark-field imaging of copper electrodeposition.

5.2 Experimental Section

5.2.1 Reagents and Solutions

All chemical reagents were used as received. Methanol, 2-allylphenol (98%), ferrocene methanol (FcMeOH, 97%), chitosan, copper sulfate pentahydrate, sulfuric acid, d-(+)-glucose (≥99.5%), glucose oxidase from *Aspergillus niger* (Type X-S, 100000-250000 units/g solid) were purchased from Sigma Aldrich. Other chemicals were of at least analytical grade. 1× PBS contains 150mM NaCl, 71.29 mM Na_2HPO_4, and 28.71 mM NaH_2PO_4. The pH is adjusted to 7.4. All solutions were prepared with 18.2 MΩ-cm deionized water obtained from a Nanopure water purification system (Thermo Scientific).

5.2.2 Electrode Preparation and Modification

Fabrication of carbon-fiber disk microelectrodes (CFEs) and 25-μm-diameter Pt disk UMEs were fabricated as previously reported in Chapter 2. All the electrodes were characterized and screened by running cyclic voltammetry at 100 mV/s in an aqueous solution containing 2 mM FcMeOH and 1× PBS. To prepare Ag/AgCl quasi-reference electrodes, a piece of 0.5-mm-diameter Ag wire (99.99%, Alfa Aesar) was submerged in bleach for at least one hour and subsequently rinsed with DI water.

The preparation of GOx-chitosan enzyme electrodes was followed by a previously published method.[24] The Pt UME was first polished with P2000 sandpaper and subsequently cleaned by boiling in 6 M HNO_3, followed by thorough rinsing with Nanopure water. The enzyme electrodes were fabricated using the following procedure: A 0.06 mL aliquot of 10 mg/mL or 1 mg/mL glucose oxidase (GOx) solution was mixed. Subsequently, 0.8 mL of chitosan solution (1.0 wt.% in 83.3 mM acetic acid) with 0.12 mL DI and 0.02 mL of glutaraldehyde (GA) aqueous solution (2.5 wt.%) were sequentially added to the mixture. After vortex mixing for 5 minutes, the Pt UME was immersed in the resulting solution for 30 seconds. The coated electrode was then air-dried at room temperature. All fabricated enzyme electrodes were stored at 4°C in 1× PBS prior to electrochemical characterization.

5.2.3 Electrochemical Measurements

A custom experimental setup was employed to perform cyclic voltammetry. The system consisted of a waveform generator (EG&G Parc 175) connected to a current amplifier (Dagan) and a breakout box (National Instruments). Data acquisition and voltage-current response measurements were performed using an in-house LabVIEW program. For amperometric experiments, signals were sampled at 100 kHz using a Dagan current amplifier equipped with a 10 kHz low-pass filter. Analog-to-digital conversion was carried out using a DigiData 1322A digitizer. All experiments were conducted inside a custom-built Faraday cage. Ag/AgCl wires served as quasi-reference or driving electrodes throughout the study. Synchronization between electrochemical and optical recordings was ensured using a digital trigger in AxoScope 10.0 or in-house LabView program.

5.2.4 Copper Electrodeposition and Off-axis DFM Imaging

Copper deposition scattering dynamics on CFEs were investigated using a customized off-axis DFM system (**Figure 5.1**), adapted from established method.[2323] The setup was based on an upright microscope modified for off-axis DFM, where the illumination path was perpendicular to the collection objective. The illumination system consisted of a 150 W halogen lamp (Cole Parmer 41723 series), hollow light-guiding tubes, and a 10× objective lens (Olympus UPlanFL N, NA 0.3). Unlike conventional DFM, no beam stop was required for the collection objective. A high-precision 3-axis micromanipulator (Newport) ensured sub-micron alignment between the illumination and collection focal points, optimizing the signal-to-noise ratio for scattering measurements. The CFE was mounted perpendicular to the collection objective in a custom cuvette and precisely positioned using a micromanipulator to align the electrode surface with the focal planes of both objectives. Copper deposition was monitored in real time using the 10× objective (Olympus UPlanFL N, NA 0.3), selected for its optimal balance of resolution and working distance.

A 128×128-pixel window in isolated crop mode was used to obtain fast exposure times with minimal time between frames. Exposure times, (frame rates) of 0.050046s (19.818 Hz) was used unless otherwise stated. Andor SOLIS software was used to record all imaging data. Andor SOLIS and ImageJ were used for image processing. All figures were created using Origin 2023.

5.3 Results and Discussion

5.3.1 In Situ Off-axis Dark-field Imaging of Copper Deposition

To integrate our off-axis imaging system with the bipolar glucose sensing platform, we first established the capability to optically monitor nanoscale copper deposition using off-axis darkfield microscopy. Copper electrodeposition was achieved by cyclic voltammetry scanning carbon fiber electrodes (CFEs) from +0 V to -0.5 V and then to +0.5 V (vs. Ag/AgCl) at 100 mV/s in an electrolyte containing 50 mM $CuSO_4$ and 50 mM H_2SO_4.

Figure 5.2 demonstrates synchronized electrochemical and optical responses during copper deposition and stripping. The cathodic current (+0 V to -0.5 V) increase corresponds to the reduction of Cu^{2+} to Cu(0) on the electrode surface. Concurrently, an increase in light scattering intensity is observed, attributed to plasmonic scattering from electrodeposited copper nanoparticles on the carbon fiber electrode (CFE). Plasmonic nanoparticles (e.g., Au, Ag, Cu) exhibit strong light scattering at their localized surface plasmon resonance (LSPR) frequencies when illuminated.[25, 26] Electrodeposited Cu nanoparticles display LSPR in the visible range, producing bright scattering signals in DFM, where only scattered light is detected.[27] According to Mie theory, the absorption and scattering cross-sections of nanoparticles depend on their size and morphology.[17] The electrodeposited copper forms fractal-like structures with rough surfaces, enhancing scattering efficiency. Larger aggregates contribute to more intense scattering.[17]Thus, the optical response enables direct visualization of the deposition process. The onset potential of optical CV is observed about 150 mV more negative than the current cyclic voltammogram. This potential shift is likely due to the minimum copper deposition threshold required for optical detection on ultramicroelectrode. As reported in the bipolar electrogenerated chemiluminescence system, the size geometry of the bipolar system can significantly change the optical detection sensitivity, where a smaller reporting pole (CFEs electrode in this system) relative to analyte pole (Pt UME) displays better signal-to-noise ratio.[28] Thus, the optical sensitivity can be further improved by replacing ultramicroelectrode to a nanoelectrode.[29] The optical signal continues to increase during the reverse potential scan (−0.5 V to −0.2 V), immediately preceding the onset of copper oxidation. This behavior indicates that the large copper clusters deposited on the CFE surface during the forward scan (0 V to −0.5 V) are still presented, while additional nucleation sites are activated, leading to the formation of new copper nuclei. A similar trend has been reported for glassy carbon electrodes, where copper deposition processes were characterized by atomic force microscopy (AFM).[30] The observed phenomenon can be attributed to the additional activation of nucleation sites on the carbon surface at increasingly negative potentials.[30] During the stripping step of Cu (0), after the applied voltage passed ~-0.2 V, the optical intensity drops, which corresponds to the copper oxidation peak on the voltammetry. After the voltage passes 0 V, current drops to near 0 nA, the optical intensity also drops to near 0, which indicates deposited copper nanoclusters are fully oxidized (stripped). A control experiment was conducted in the absence of $CuSO_4$ to verify the origin of scattering signal. As shown in **Figure 5.2B**, no copper deposition scattering signal is detected, confirming that the signal observed in off-axis DFM arises exclusively from copper deposition.

5.3.2 Bipolar Coupling of Copper Deposition and H_2O_2 Oxidation

In a closed bipolar electrochemical system, the anodic and cathodic poles are physically separated into two distinct compartments, connected via a metallic wire electrode.[31]Two driving electrodes apply an external voltage across the isolated solutions, enabling the coupling of complementary redox reactions at opposing poles.[8]By integrating a light-generating process at one pole, the light intensity can serve as a quantitative reporter of electrochemical activity. As previously discussed, variations in light scattering intensity correlate with the copper deposition process, making it a suitable optical signal reporter.

Figure 5.3A illustrates the experimental configuration of the closed bipolar system. As proof of concept, H_2O_2 oxidation was selected as the model anodic reaction, coupled with cathodic copper deposition, given that H_2O_2 is the enzymatic product of glucose oxidation catalyzed by glucose oxidase (GOx). Cell 1 contained a 25 μm Pt ultramicroelectrode (UME) immersed in an H_2O_2 and PBS solution, while Cell 2 included a 50 mM $CuSO_4$/50 mM H_2SO_4 electrolyte with a 5 μm carbon fiber electrode (CFE). Two Ag/AgCl driving electrodes, one in each cell, were connected directly to the current amplifier. The Pt UME and CFE were connected directly to complete the bipolar circuit.

Figure 5.3B presents the bipolar cyclic voltammogram (CV) obtained using a 25 μm Pt UME for 1 mM H_2O_2 oxidation coupled with a 5 μm CFE as the cathodic copper deposition reporting pole. The results demonstrate that in bipolar system, the H_2O_2 oxidation current reaches a diffusion-limited plateau at applied potentials exceeding +1.2 V. Comparison with conventional 2-electrode voltammetry (green and blue curves, **Figure 5.3B**) suggests that the anodic H_2O_2 oxidation limits the overall faradaic current in the bipolar system, as evidenced by the similar steady-state currents observed in both configurations. This limiting current (14.4 nA) aligns with the theoretical steady-state current expected for a 25 μm Pt disk electrode in 1 mM H_2O_2 solution. [32]The theoretical driving potential across the bipolar electrodes can be calculated by **Equation 1**[33], where E_{anode} is the driving potential on the anodic pole (H_2O_2 oxidation), and $E_{cathode}$ is the driving potential on the cathodic pole of the bipolar system.

$$E_{bipolar} = E_{anode} - E_{cathode} \qquad (1)$$

Given that the copper reduction occurs at ~ -200 mV vs. Ag/AgCl (as shown in **Figure 5.3B**), and H_2O_2 oxidation occurs at around 100 mV vs. Ag/AgCl (**Figure 5.3B**), at least 300 mV would be required for this bipolar coupling process, which is confirmed by the bipolar cyclic voltammogram.

The correlated copper deposition scattering signal was synchronously collected with the electrochemical response. Both the current-voltage and optical intensity-voltage voltammograms are presented in **Figure 5.4**. While both signals show increasing trends with applied potential, the optical signal demonstrates an onset potential approximately 250 mV more positive than the current signal, consistent with observations in 2-electrode system. Control experiments performed in the absence of H_2O_2 showed slight increases in both current and optical signals, potentially attributable to competing redox processes such as water oxidation. To minimize these background interferences, an applied potential of +1.0 V was selected for subsequent amperometric glucose sensing measurements.

The sensitivity of the closed-bipolar system was evaluated by measuring the optical response to varying concentrations of H_2O_2 in PBS. Under an applied constant potential of +1.0 V for 15 s, the resulting copper deposition exhibits a concentration-dependent increase in optical intensity, with a linear correlation ($R^2 = 0.987$) observed over the range of 50 μM to 1 mM (**Figure 5.5**). The system demonstrates a limit of detection (LOD) of 35.88 μM H_2O_2, which shows a better detection sensitivity when comparing to a previously reported bipolar electrochemiluminescence imaging system for H_2O_2 detection with a LOD of 50 μM.[34] Given the well-established enzymatic generation of H_2O_2 from glucose oxidase (GOx)-catalyzed reactions, this system holds significant promise for indirect glucose sensing with high sensitivity and rapid response.

5.3.3 Characterization of GOx-chitosan Enzyme Electrode

Chitosan, a biocompatible and porous polymer, was selected as the immobilization matrix due to its strong adhesion, structural stability, and ability to facilitate substrate diffusion while entrapping enzymes.[35] Its high density of amino groups enables effective cross-linking with glutaraldehyde (GA), forming covalent bonds with GOx to enhance immobilization stability.[36] During measurement, glucose diffuses to the electrode surface, where is oxidized by immobilized GOx. The enzymatic reaction generates H_2O_2, which is subsequently oxidized at the electrode surface and detected amperometrically.[37] This two-step process (enzymatic reaction followed by electrochemical detection) ensures high selectivity and sensitivity toward glucose.

The successful immobilization of glucose oxidase (GOx) within the chitosan film was first verified electrochemically. **Figure 5.6A** demonstrates that GOx-functionalized electrodes (1 mg/mL in chitosan film) show a characteristic oxidation current between +0.3 V and +0.6 V (vs. Ag/AgCl) in 400 mM glucose solution, corresponding to the electrochemical oxidation of enzymatically generated H_2O_2. Control experiments with GOx-free chitosan-modified electrodes show no detectable current in this potential window, confirming the enzymatic origin of the signal. To unequivocally attribute this response to H_2O_2 oxidation, additional control experiments were performed (**Figure 5.6B**). A bare Pt electrode in a 1 mM

H_2O_2/1 mM glucose solution (red curve) exhibits an oxidation peak with a potential window identical to that observed for the GOx-chitosan-modified electrode in 1 mM glucose (green curve). This result confirms that the anodic current originates from H_2O_2 oxidation. Furthermore, no current is observed when either: (i) GOx is absent from the chitosan film (yellow curve), or (ii) glucose is removed from the test solution (blue curve). These results provide evidence that the electrochemical signal originates specifically from GOx-catalyzed glucose oxidation and subsequent H_2O_2 detection.

The loading of GOx critically influences the detection sensitivity of the system. To optimize the enzyme loading, Pt UMEs were functionalized with varying concentrations of GOx in chitosan and evaluated by measuring the oxidation current of enzymatically generated H_2O_2 via cyclic voltammetry in glucose solutions. As shown in **Figure 5.7A**, Pt UMEs modified with 1 mg/mL GOx enabled robust detection of glucose at concentrations as low as 0.1 mM. In contrast, electrodes functionalized with 0.1 mg/mL GOx exhibited negligible current differentiation between 1 mM glucose and blank PBS (**Figure 5.7B).** Consequently, 1 mg/mL GOx in chitosan was selected for subsequent experiments to ensure high sensitivity.

5.3.4 Quantitative Detection of Glucose with Off-axis Dark-field Imaging

Glucose quantification was achieved through closed bipolar coupling of a glucose oxidase (GOx)-modified Pt ultramicroelectrode (UME) with an off-axis dark-field imaging system for monitoring copper deposition on CFEs. The GOx-modified Pt UME was incubated in glucose solutions of varying concentrations for 30 min at room temperature, followed by the application of a constant potential of +1 V for 90 s. The resulting copper deposition was tracked in real time using off-axis DFM. As illustrated in **Figure 5.8A**, the optical scattering intensity increases with the duration of applied potential, reflecting the progressive accumulation of copper nanoparticles on the carbon fiber electrode surface. In contrast, no detectable scattering signal is observed in the absence of glucose, as the anodic current generated at the Pt UME is insufficient to drive copper deposition at the cathodic reporting pole (CFE). **Figure 5.8B** displays the dark-field images of the CFE after 90 s of polarization, demonstrating a concentration-dependent enhancement in scattering intensity. A linear correlation ($y = 301.3x + 4.01$, $R^2 = 0.978$) between optical intensity and glucose concentration is established with liner detection range (LDR) of 100 µM to 1 mM (**Figure 5.8C**). The system demonstrates a limit of detection (LOD) of 16.04 µM glucose. The sensitivity is adequate since the clinical glucose concentration is greater than 3.5 mM. [38]

5.4 Conclusion

In this work, we integrated an off-axis dark-field imaging system with a closed bipolar electrochemical platform to enable real-time, optical tracking of nanoscale copper deposition and its application in glucose sensing. Leveraging the strong plasmonic scattering of electrodeposited copper nanoparticles, we demonstrated that off-axis DFM serves as a highly sensitive and direct imaging tool for monitoring electrochemical processes at ultramicroelectrode surfaces. The bipolar coupling of H2O2 oxidation (anodic pole) and copper deposition (cathodic pole) facilitates the quantitative detection of H2O2, achieving a linear range of 50 µM to 1 mM and a detection limit of 35.88 µM. For glucose detection, glucose oxidase (GOx) was immobilized within a chitosan matrix on a Pt ultramicroelectrode. The resulting biosensor exhibits excellent sensitivity, with a linear response from 100 µM to 1 mM and a limit of detection of 16.04 µM. The strong correlation between optical scattering intensity and glucose concentration underscores the potential of this approach for label-free, real-time monitoring of enzymatic reactions.

This study not only provides new insights into the integration of closed bipolar electrochemistry with optical dark-field imaging but also establishes a versatile platform for biosensing applications. By functionalizing the system with alternative oxidase enzymes, this strategy can be adapted for the detection of diverse biomarkers. Future work will focus on enhancing sensitivity through nanoelectrode integration, as well as extending the platform to other enzymatic or catalytic processes for biomedical and environmental monitoring. Additionally, the development of an imaging array could further improve spatial resolution and throughput.

5.5 Figures

Figure 5.1. The configuration of off-axis DFM.
The experimental setup of off-axis DFM for imaging Cu deposition on the carbon fiber electrode (CFE) surface.

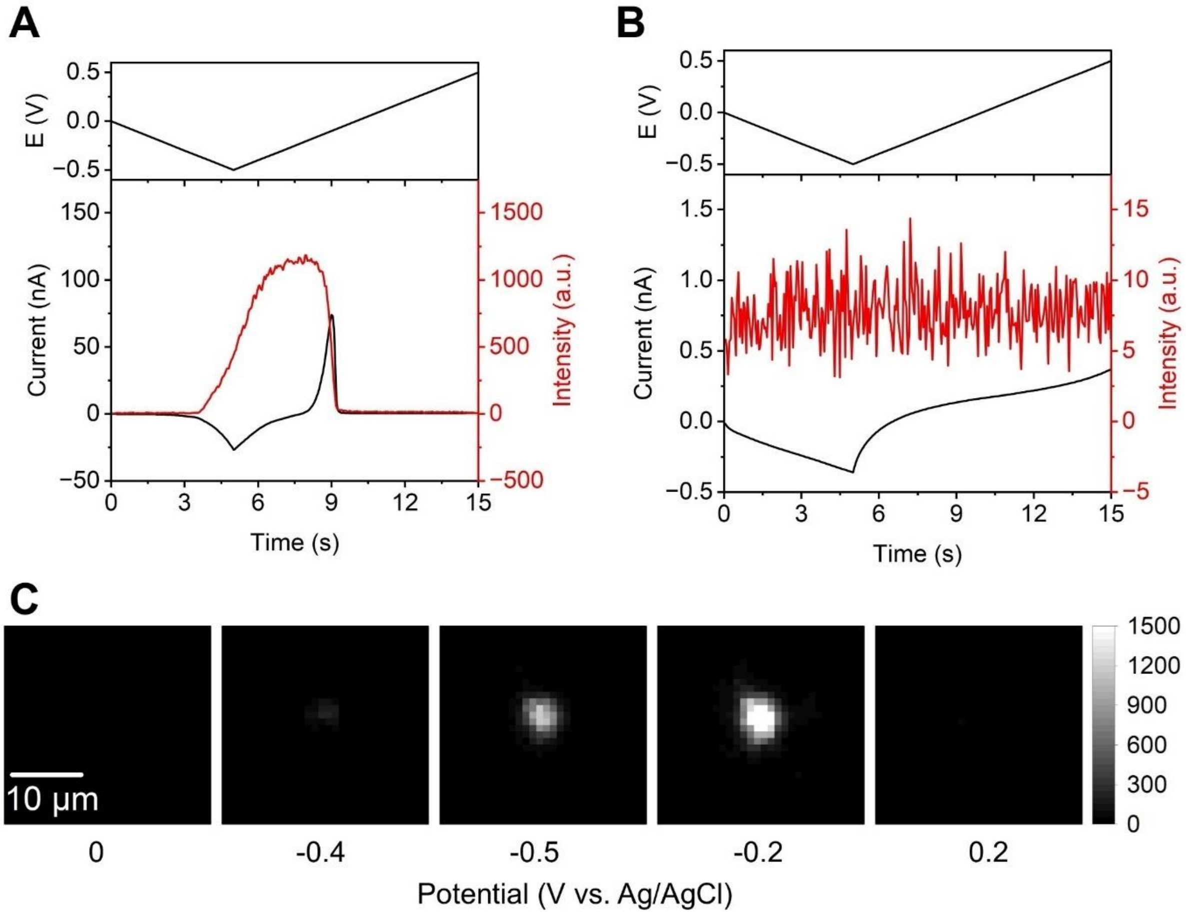

Figure 5.2. Off-axis DFM imaging of Cu electrodeposition.

(A) Simultaneous electrochemical (black) and optical scattering (red) signals recorded during immersion of a CFE in a solution containing 50 mM $CuSO_4$ and 50 mM H_2SO_4. (B) Correlated current (black) and optical scattering (red) responses of a CFE in 50 mM H_2SO_4. (C) Off-axis DFM images capturing Cu electrodeposition-induced scattering on the CFE surface at applied potentials of −0 V, −0.4 V, −0.5 V, -0.2 V, and 0.2 V (vs. Ag/AgCl).

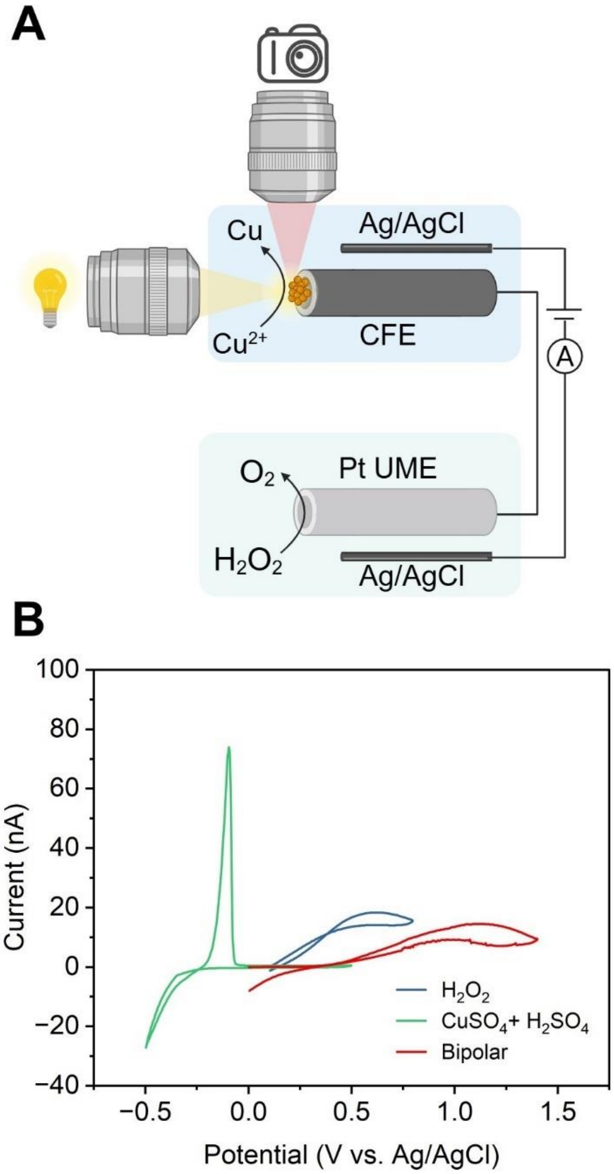

Figure 5.3. Coupling of Cu electrodeposition with H_2O_2 oxidation using closed BPE.
(A) Schematic of the closed BPE setup, which enables simultaneous measurement of the current through the BPE and light emission from the reporting pole (CFE) using off-axis DFM. (B) Electrochemical signals of two-electrode and closed BPE systems. Blue line: CV of 25 μm Pt UME in a two-electrode setup in 1 mM H_2O_2 and 10 mM PBS. Green line: Voltammogram of Cu deposition (50 mM $CuSO_4$ and 50 mM H_2SO_4) in a two-electrode system. Red line: BPE response with the anode (CFE) in 1 mM H_2O_2 and 10 mM PBS and the cathode (Pt UME) in 50 mM $CuSO_4$ and 50 mM H_2SO_4.

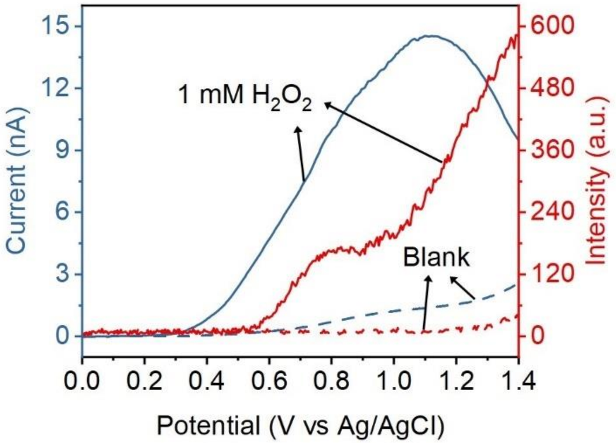

Figure 5.4. Correlated current and optical responses of closed BPE system.
Solid and dashed lines represent responses in the presence and absence of H_2O_2 in the analyte (anodic) pole, respectively. The reporter (cathodic) pole contained 50 mM $CuSO_4$ and 50 mM H_2SO_4 solution.

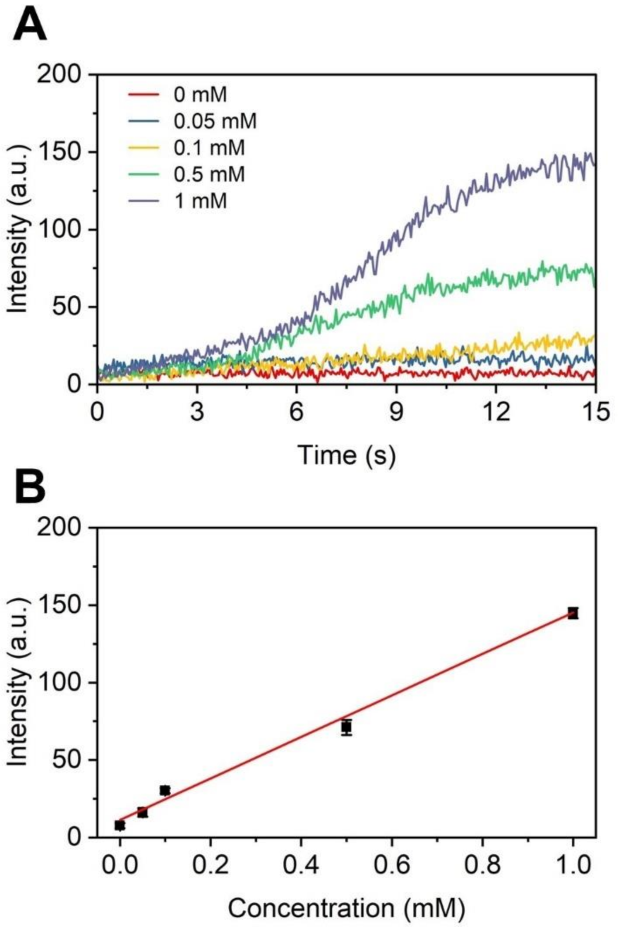

Figure 5.5. Quantitative detection of H_2O_2 using off-axis DFM.

(A) Representative time-dependent scattering intensity profiles for different H_2O_2 concentrations (0-1 mM in 1 × PBS). (B) Calibration curve showing the linear relationship between H_2O_2 concentration and DFM scattering intensity (n = 3; error bars represent mean ± standard deviation).

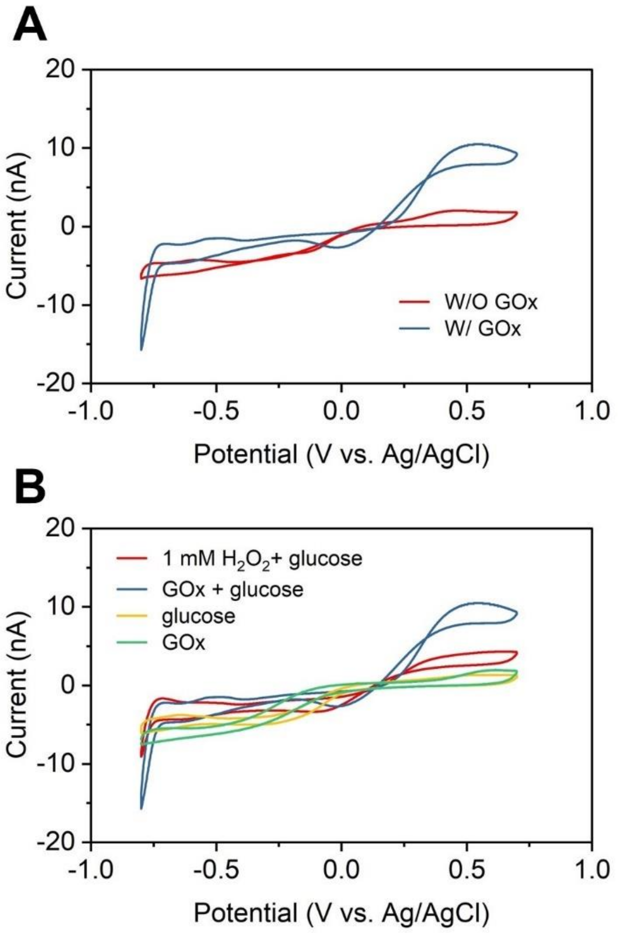

Figure 5.6. Characterization of glucose oxidase modified enzyme electrode.
(A) CVs of a GOx-modified Pt UME (blue) and an unmodified Pt UME (red) in 400 mM glucose (1× PBS). (B) CVs of Pt UMEs under varying conditions: (i) bare Pt UME in 1 mM H_2O_2 + 400 mM glucose (red), (ii) GOx-modified Pt UME in 1 mM glucose (1× PBS, blue), (iii) bare Pt UME in 1 mM glucose (yellow), and (iv) GOx-modified Pt UME in 1× PBS (green).

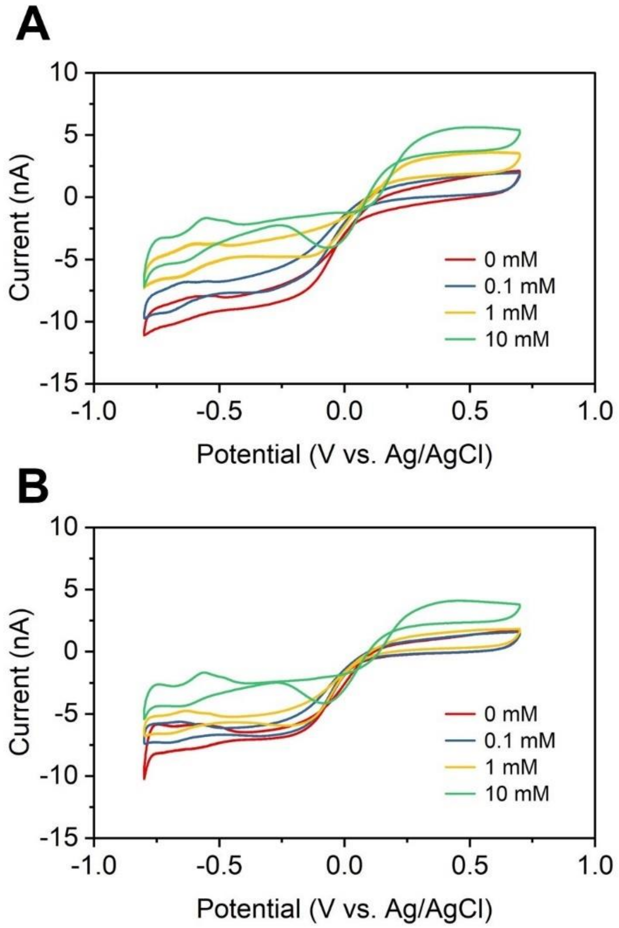

Figure 5.7. Optimization of GOx loading on enzyme electrode.
A) CVs of a GOx-modified electrode (1 mg/mL GOx) in glucose solutions at varying concentrations (indicated). (B) CVs of a GOx-modified electrode (0.1 mg/mL GOx) under glucose concentration gradients.

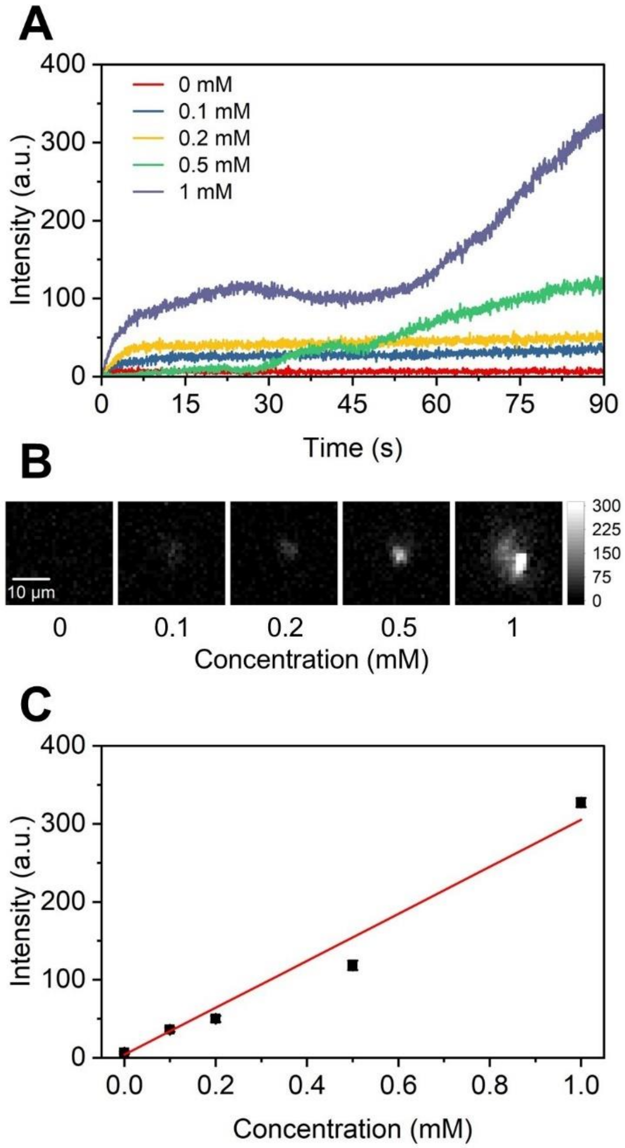

Figure 5.8. Quantitative detection of glucose using off-axis DFM.
(A) Time-dependent scattering intensity profiles for glucose concentrations ranging from 0 to 1 mM in 10 mM PBS. (B) Corresponding off-axis DFM images of Cu electrodeposition patterns after 90 s of applied potential for each glucose concentration. (C) Linear calibration curve correlating glucose concentration with normalized scattering intensity (n = 3; data shown as mean ± SD).

5.6 References

(1) Takahashi, Y.; Kumatani, A.; Shiku, H.; Matsue, T. Scanning Probe Microscopy for Nanoscale Electrochemical Imaging. *Anal. Chem.* **2017**, *89* (1), 342–357.

(2) Bian, K.; Gerber, C.; Heinrich, A. J.; Müller, D. J.; Scheuring, S.; Jiang, Y. Scanning Probe Microscopy. *Nat. Rev. Methods Primers* **2021**, *1* (1), 36.

(3) Peng, Z.; Wan, R.; Zhang, B. Single-Molecule Imaging for Probing the Electrochemical Interface. *Curr. Opin. Electrochem.* **2022**, *35*, 101047.

(4) Xing, Z.; Lu, X.; Zhang, Z.; Zhao, Y.; Cao, Y.; Zhou, Y.; Zhu, J. J. Electrochemiluminescence Microscopy in Nano-Electrochemistry Research: Unraveling the Underlying Principles, Tracing the Evolutionary Developments, and Charting the Prospective Trajectories. *Adv. Funct. Mater.* **2025**, 2425768.

(5) Sambur, J. B.; Chen, P. Distinguishing Direct and Indirect Photoelectrocatalytic Oxidation Mechanisms Using Quantitative Single-Molecule Reaction Imaging and Photocurrent Measurements. *J. Phys. Chem. C.* **2016**, *120*, 20668–20675.

(6) Qin, X.; Gao, J.; Jin, H. J.; Li, Z. Q.; Xia, X. H. Closed Bipolar Electrode Array for Optical Reporting Reaction-Coupled Electrochemical Sensing and Imaging. *Chem. Eur. J.* **2023**, *29*, e202202687.

(7) Mavré, F.; Anand, R. K.; Laws, D. R.; Chow, K. F.; Chang, B. Y.; Crooks, J. A.; Crooks, R. M. Bipolar Electrodes: A Useful Tool for Concentration, Separation, and Detection of Analytes in Microelectrochemical Systems. *Anal. Chem.* **2010**, *82*, 8766–8774.

(8) Guerrette, J. P.; Oja, S. M.; Zhang, B. Coupled Electrochemical Reactions at Bipolar Microelectrodes and Nanoelectrodes. *Anal. Chem.* **2012**, *84*, 1609–1616.

(9) Defnet, P. A.; Zhang, B. Detection of Transient Nanoparticle Collision Events Using Electrochemiluminescence on a Closed Bipolar Microelectrode. *ChemElectroChem* **2020**, *7*, 252–259.

(10) Qin, X.; Jin, H. J.; Li, X.; Li, J.; Pan, J. Bin; Wang, K.; Liu, S.; Xu, J. J.; Xia, X. H. Label-Free Electrochemiluminescence Imaging of Single-Cell Adhesions by Using Bipolar Nanoelectrode Array. *Chem. Eur. J.* **2022**, *28*, e202103964.

(11) Khani, H.; Wipf -, D. O.; Semi Lee, C.; Na, Y.; Hee Seol, K. Electrocatalyst Screening on a Massive Array of Closed Bipolar Microelectrodes. *J. Electrochem. Soc.* **2021**, *168*, 106502.

(12) Wang, W. Imaging the Chemical Activity of Single Nanoparticles with Optical Microscopy. *Chem. Soc. Rev.* **2018**, *47*, 2485–2508.

(13) Saqib, M.; Fan, Y.; Hao, R.; Zhang, B. Optical Imaging of Nanoscale Electrochemical Interfaces in Energy Applications. *Nano Energy* **2021**, *90*, 106539.

(14) Novo, C.; Funston, A. M.; Pastoriza-Santos, I.; Liz-Marzán, L. M.; Mulvaney, P. Influence of the Medium Refractive Index on the Optical Properties of Single Gold Triangular Prisms on a Substrate. *J. Phys. Chem. C.* **2008**, *112*, 3–7.

(15) Shi, R.; Chen, X.; Huo, J.; Guo, S.; Smith, Z. J.; Chu, K. Epi-Illumination Dark-Field Microscopy Enables Direct Visualization of Unlabeled Small Organisms with High Spatial and Temporal Resolution. *J. Biophotonics.* **2022**, *15*.

(16) Hill, C. M.; Pan, S. A Dark-Field Scattering Spectroelectrochemical Technique for Tracking the Electrodeposition of Single Silver Nanoparticles. *J. Am. Chem. Soc.* **2013**, *135*, 17250–17253.

(17) Nguyen, T. N.; Cappillino, P. J.; Chang, W.-S. Revealing Enhanced Size Uniformity of the Electrochemical Deposition of Palladium Nanoparticles via Single-Particle Dark-Field Scattering Imaging. The *J. Phys. Chem. C.* **2025**, *129*, 6477–6485.

(18) Brasiliense, V.; Clausmeyer, J.; Dauphin, A. L.; Noël, J. M.; Berto, P.; Tessier, G.; Schuhmann, W.; Kanoufi, F. Opto-Electrochemical In Situ Monitoring of the Cathodic Formation of Single Cobalt Nanoparticles. *Angew. Chem. Int. Ed.* **2017**, *56*, 10598–10601.

(19) Godeffroy, L.; Ciocci, P.; Nsabimana, A.; Miranda Vieira, M.; Noël, J. M.; Combellas, C.; Lemineur, J. F.; Kanoufi, F. Deciphering Competitive Routes for Nickel-Based Nanoparticle Electrodeposition by an Operando Optical Monitoring. *Angew. Chem. Int. Ed.* **2021**, *60*, 16980–16983.

(20) Zhao, Y.; Zhao, W.; Chen, H. Y.; Xu, J. J. Dark-Field Microscopic Real-Time Monitoring the Growth of Au on Cu_2O Nanocubes for Ultra-Sensitive Glucose Detection. *Anal. Chim. Acta.* **2021**, *1162*, 338503.

(21) Senthilkumar, M.; Mathiyarasu, J.; Joseph, J.; Phani, K. L. N.; Yegnaraman, V. Electrochemical Instability of Indium Tin Oxide (ITO) Glass in Acidic PH Range during Cathodic Polarization. *Mater. Chem. Phys.* **2008**, *108*, 403–407.

(22) Geiger, S.; Kasian, O.; Mingers, A. M.; Mayrhofer, K. J. J.; Cherevko, S. Stability Limits of Tin-Based Electrocatalyst Supports. *Sci. Rep.* **2017**, *7*, 1–7.

(23) Suvira, M.; Ahuja, A.; Lovre, P.; Singh, M.; Draher, G. W.; Zhang, B. Imaging Single H_2 Nanobubbles Using Off-Axis Dark-Field Microscopy. *Anal. Chem.* **2023**, *95*, 15893–15899.

(24) Ren, J.; Shi, W.; Li, K.; Ma, Z. Ultrasensitive Platinum Nanocubes Enhanced Amperometric Glucose Biosensor Based on Chitosan and Nafion Film. *Sens. Actuators B Chem.* **2012**, *163*, 115–120.

(25) Fang, Y.; Xu, B.; Wang, S.; Liu, H.; Wang, J.; Si, M. Highly Stable Localized Surface Plasmon Resonance of Cu Nanoparticles Obtained via Oxygen Plasma Irradiation. *Nanoscale* **2024**, *16*, 9748–9753.

(26) Tcherniak, A.; Ha, J. W.; Dominguez-Medina, S.; Slaughter, L. S.; Link, S. Probing a Century Old Prediction One Plasmonic Particle at a Time. *Nano Lett.* **2010**, *10*, 1398–1404.

(27) Liu, M.; Chao, J.; Deng, S.; Wang, K.; Li, K.; Fan, C. Dark-Field Microscopy in Imaging of Plasmon Resonant Nanoparticles. *Colloids Surf. B Biointerfaces* **2014**, *124*, 111–117.

(28) Oja, S. M.; Zhang, B. Electrogenerated Chemiluminescence Reporting on Closed Bipolar Microelectrodes and the Influence of Electrode Size. *ChemElectroChem* **2016**, *3*, 457–464.

(29) Suvira, M. *Novel Electroanalytical Tools for Probing Electrochemically Generated Surface Nanobubble Characteristics*, University of Washington: United States -- Washington, **2023**.

(30) Grujicic, D.; Pesic, B. Electrodeposition of Copper: The Nucleation Mechanisms. *Electrochim. Acta.* **2002**, *47*, 2901–2912.

(31) Cox, J. T.; Guerrette, J. P.; Zhang, B. Steady-State Voltammetry of a Microelectrode in a Closed Bipolar Cell. *Anal. Chem.* **2012**, *84*, 8797–8804.

(32) Bard, A. J.; Faulkner, L. R.; White, H. S. *Electrochemical Methods: Fundamentals and Applications*; Wiley, 2022.

(33) Han, C.; Hao, R.; Fan, Y.; Edwards, M. A.; Gao, H.; Zhang, B. Observing Transient Bipolar Electrochemical Coupling on Single Nanoparticles Translocating through a Nanopore. *Langmuir* **2019**, *35*, 7180–7190.

(34) Zhang, J. D.; Yu, T.; Li, J. Y.; Xu, J. J.; Chen, H. Y. An ITO Bipolar Array for Electrochemiluminescence Imaging of H_2O_2. *Electrochem. Commun.* **2014**, *49*, 75–78.

(35) Suginta, W.; Khunkaewla, P.; Schulte, A. Electrochemical Biosensor Applications of Polysaccharides Chitin and Chitosan. *Chem. Rev.* **2013**, *113*, 5458–5479.

(36) Monteiro, O. A. C.; Airoldi, C. Some Studies of Crosslinking Chitosan–Glutaraldehyde Interaction in a Homogeneous System. *Int. J. Biol. Macromol.* **1999**, *26*, 119–128.

(37) Wang, J. Electrochemical Glucose Biosensors. *Chem. Rev.* **2008**, 108, 814–825.

(38) Forzani, E. S.; Zhang, H.; Nagahara, L. A.; Amlani, I.; Tsui, R.; Tao, N. A Conducting Polymer Nanojunction Sensor for Glucose Detection. *Nano Lett.* **2004**, *4*, 1785–1788.

VITA

Ruixuan Wan was born and raised in Kunming, China. She graduated from Kunming No. 1 High School in 2012. Later, she obtained her B.S. and M.S. in Pharmaceutical Science from China Pharmaceutical University in 2016 and 2019, respectively. The following September, she joined University of Washington to pursue her Ph.D. in Chemistry under the guidance of Prof. Bo Zhang.